Università degli Studi di Padova

Università degli Studi di Padova
Centro Interdipartimentale "Centro Ricerche Fusione"

Universidade Técnica de Lisboa
Instituto Superior Técnico

Joint research doctorate in fusion science and engineering
Cicle XXVI

FLOW AND TRANSPORT IN THE EDGE OF FUSION DEVICES

Coordinator: Ch.mo Prof. Piero Martin

Supervisor: Ch.mo Prof. Piero Martin

Supervisor: Dott. Gianluca Spizzo

Doctoral Student:
Giovanni Ciaccio

♡ ◊

Abstract

The main topic of the Thesis is the study of the electrostatic, plasma response (E^r and flows) to magnetic islands embedded in the chaotic edge of a tokamak, when resonant magnetic perturbations (RMPs) are applied. Results are compared with the known phenomenology and theory in the chaotic edge of a reversed-field pinch (RFP). Proxies of the two configurations are the tokamak TEXTOR, with the application of the dynamic ergodic divertor (DED); and the RFX-mod RFP. The main tool used for simulations of islands, two-fluid transport (electrons and ions), and ambipolar E^r field, is the Hamiltonian guiding-center code ORBIT.

As an initial step, to validate the reconstruction of the edge topology of TEXTOR and RFX, the ORBIT code has been validated against the volume-preserving code NEMATO [24]. In the limit of low energy, ORBIT can be used to trace the magnetic field topology, in a way in all respects similar to field line-tracing codes. NEMATO is a field-line tracing code, implemented to integrate solenoidal flows for incompressible fluid dynamics, with automatic volume preservation [47]. The question is, how accurate is the description of the magnetic field with ORBIT, given that it is a Hamiltonian code (therefore, with a simplectic matrix), but it uses a Runge-Kutta (RK) integrator instead of a fully implicit solver (which is the case of NEMATO). Besides this, ORBIT describes perturbations in terms of a scalar field α, such that $\delta\vec{B} = \nabla \times \alpha\vec{B}_0$, with B_0 the equilibrium field. The two codes are validated on the structure of the $q = 0$ island chain, which characterizes the multi helicity (MH) configuration in RFP. As input for both codes we use the snapshot of a cylindrical 3D nonlinear, magnetohydrodynamic (MHD) visco-resistive simulation (SpeCyl code [20]). The first benchmarking test employs a Hamiltonian (single-mode) magnetic field configuration. Both codes successfully yield field lines which follow flux surfaces in both the $m = 1$ and $m = 0$ cases. The comparison between the codes is then extended to a chaotic magnetic field configuration, by including many modes. The result is that the scalar field representation of ORBIT and the RK integrator do not include measurable differences in the Poincaré maps and in the calculation of the correlation length of the chaotic field.

As a second step in this Thesis, in order to develop a common picture of particle transport with edge magnetic islands in Tokamaks and RFPs, test

particle transport simulations are carried out in TEXTOR following the steps of the study performed in RFX-mod [123]. The RMP configurations studied are the $m/n = 12/4$ and $3/1$. The ORBIT code has been adapted to the equilibrium of TEXTOR (circular equilibrium with pressure [144]), and a proper form for the eigenfunctions has been developed, on the basis of the analytical formula used in TEXTOR using as input the current flowing in the DED. The resulting Poincaré plots show the well-known, basic features of TEXTOR stochastic edge, such as the inner island chain, the remnant islands, and the laminar flux tubes embedded in the ergodic fingers, which is consistent with previous works on this subject. Maps in the (r, θ) plane of the electron and ion parallel connection length to the wall, $L_\parallel(r, \theta)$, highlight the properties of the magnetic structures observed in the Poincaré plot: while ions, having a large Larmor radius, are weakly affected by the magnetic topology, electron trajectories are linked to the magnetic field lines. The behavior of $L_\parallel$ entails a characteristic modulation of the radial electric field E^r with large positive values in the zone with electron $L_\parallel \approx 0$ (the so-called laminar flux tubes, which occupy a region in between the main island chain and the remnant islands).

As a further step, the evaluation of the local radial transport of particles, i.e. ion and electron diffusion coefficients (D_i and D_e, respectively), has been performed along a helical path from the O-point (OP) through the X-point (XP) of an $m/n = 4/1$ remnant island. The result shows that D_i is rather constant along the path, and it is almost neoclassical, while D_e is larger ($4 \div 40\ m^2/s$), and is strongly modulated (larger at the XP, lower at the OP), consistently with the $L_\parallel$ maps. Finally, an analytic 3D formulation of the ambipolar potential for the $3/1$ DED configuration is developed on the basis of the geometry of the $m/n = 4/1$ magnetic island, that balances electron and ion fluxes inside the island. The result is compared to measurements of plasma potential inside an $m/n = 4/1$ island in the edge of the TEXTOR device and with the analysis on RFX-mod edge. In RFX-mod ORBIT predicts the potential well to stay in proximity of the OP of the main island ($m/n = 0/1$), while measurements show the potential well near the XP. In the TEXTOR experiment fast Mirnov probe measurements show that the potential well corresponds to the XP of the $m/n = 4/1$ island, i.e. the region with larger D_e, consistently with ORBIT results. The difference between RFX and TEXTOR could be ascribed to a collisional dependence (the case of RFX is highly collisional, contrary to TEXTOR); to a different level of chaos, in RFX compared to TEXTOR; or to a more pronounced plasma-wall interaction.

The final, main message of the Thesis is that RMPs in tokamaks, even if induced as static perturbation, are capable of producing a pattern of large, radial electric field E^r, which is the footprint of the underlying topology. The pattern of E^r can be successfully reproduced by ORBIT. The comparison with RFX shows that collisional effects can be important in determining

amplitude and phase of this electrostatic potential.

Sommario

L'argomento principale della Tesi è lo studio delle isole magnetiche, al bordo di una macchina tokamak, create per mezzo di perturbazioni magnetiche risonanti (RMP), e della relativa risposta elettrostatica del plasma (flussi e campo elettrico radiale E^r). I risultati sono stati confrontati con la fenomenologia e la teoria già conosciute nell'ambito del chaos magnetico al bordo di una macchina con configurazione magnetica *reversed-field pinch* (RFP). In particolare, l'analisi è stata eseguita sul tokamak TEXTOR ed il confronto fatto con il RFP RFX-mod. Per tale studio, si é utilizzato il codice hamiltoniano di centro guida ORBIT, che permette di eseguire simulazioni di trasporto di particelle e ricostruire la topologia magnetica.

In primis, ORBIT é stato confrontato con il codice *volume-preserving* NEMATO [24], allo scopo di validare la ricostruzione della topologia magnetica di ORBIT, al bordo di TEXTOR e RFX-mod. Nel limite di bassa energia, ORBIT può essere utilizzato per tracciare le linee di campo magnetico, in modo simile ai codici *field-line tracing*, come NEMATO. NEMATO integra flussi solenoidali per fluidi incomprimibili, conservando automaticamente il volume [47]. Si vuole verificare quanto accurata sia la descrizione di un campo magnetico da parte di ORBIT, che pur essendo un codice hamiltoniano, usa un integratore Runge-Kutta (RK) anziché risolvere in modo completamente implicito le equazioni del moto (come fa NEMATO). Inoltre, in ORBIT le perturbazioni sono descritte mediante un campo scalare α, così che $\delta\vec{B} = \nabla \times \alpha\vec{B}_0$, dove B_0 è il campo all'equilibrio. I due codici sono validati su una struttura composta da isole $q = 0$ che caratterizzano la configurazione *multy helicity* (MH) nel RFP. I dati in ingresso, per entrambi i codici, provengono da una simulazione MHD, *visco-resistive* in geometria cilindrica 3D non lineare, del codice SpeCyl [20]. Inizialmente il confronto è stato eseguito su una semplice configurazione con uno solo modo non nullo nello spettro delle perturbazioni, verificando che entrambi i codici creano linee di campo che seguono le superfici di flusso calcolate analiticamente. Il confronto è quindi esteso alla configurazioni caotica (con tutti i modi). Il risultato è che la rappresenzione α di ORBIT e l'integratore RK, non comportano alcuna differenza apprezzabile nelle mappe di Poincaré e nel calcolo della lunghezza di correlazione.

Nella seconda parte della Tesi, allo scopo di disegnare un quadro co-

mune del trasporto di particelle nel tokamak RMP e nel RFP, simulazioni di trasporto di particelle (ioni ed elettroni) sono state eseguite, seguendo le analisi storicamente effettuate in RFX-mod [123]. In particolare, due configurazioni magnetiche in TEXTOR sono state considerate: $m/n = 12/4$ e $3/1$. Il codice ORBIT è stato adattato ricostruendo l'equilibrio magnetico di TEXTOR (equilibrio circulare con pressione [144]) e le perturbazioni, sulla base di una formula analitica sviluppata a TEXTOR. Le mappe di Poincaré create con ORBIT mostrano le caratteristiche base del bordo caotico di TEXTOR, come la catena interna di isole, le isole *remnant*, ed i tubi di flusso laminare circondati da una zona ergodica (*ergodic fingers*), consistentemente con lavori precedenti effettuati a TEXTOR. Le proprietà delle suddette strutture sono evidenziate con simulazioni di lunghezza di connessione, $L_\parallel(r, \theta)$: mentre gli ioni, avendo un raggio di Larmor più grande, sono debolmente influenzati dalla topologia magnetica, le traiettorie degli elettroni sono vincolate alle linee di campo. L'andamento di $L_\parallel$ comporta una caratteristica modulazione di E^r con valori positivi nelle zone con $L_\parallel \approx 0$ (cioè i tubi di flusso laminare tra le isole remnant e le catena di isole interna).

Successivamente, i coefficienti di diffusione ionici ed elettronici (D_i and D_e, rispettivamente), sono stati calcolati lungo l'intervallo poloidale tra l'*O-point* (OP) e l'*X-point* (XP) dell'isola remnant $m/n = 4/1$, per valutare localmente il trasporto radiale di particelle. Il risultato mostra che D_i è circa costante lungo l'intervallo e quasi neoclassico, mentre D_e è più grande ($4 \div 40\ m^2/s$), e fortemente modulato (più grande nel XP, più piccolo nel OP), consistentemente con le mappe di $L_\parallel$. Infine, una formulazioni 3D, analitica del campo ambipolare nella configurazione $3/1$ è stata sviluppata a partire dalla geometria dell'isola $m/n = 4/1$, che bilancia i flussi ionici ed elettronici al bordo. Il risultato è confrontato con misure di potenziale di plasma nell'isola $m/n = 4/1$ e con le analisi al bordo di RFX-mod. In RFX-mod ORBIT predice una buca di potenziale in prossimità del OP dell'isola principale ($m/n = 0/1$), mentre le misure mostrano che la buca sia vicino al XP. In TEXTOR le misure mostrano che la buca di potenziale in corrispondenza del XP dell'isola $m/n = 4/1$, cioè la regione con grande D_e, consistentemente con i risultati di ORBIT. La differenza tra RFX e TEXTOR può essere dovuta alla dipendenza dalle collisioni (in RFX si ha alta collisionalità, contrariamente a TEXTOR); a una diversa quantità di caos tra RFX-mod e TEXTOR; oppure ad una interazione plasma-parete più pronunciata in RFX-mod.

Il messaggio principale delle Tesi è che gli RMPs nei tokamak, anche se indotti come perturbazioni statiche, sono capaci di produrre un campo elettrico radiale E^r, la cui struttura è la stessa della topologia magnetica al bordo. Tale struttura può essere riprodotta in ottima approssimazione da ORBIT. Il confronto con RFX dimostra che gli effetti collisionali possono essere importanti nel determinare ampiezza e fase di questo potenziale elettrostatico.

Contents

Abstract **v**

Sommario **ix**

List of Figures **xiii**

1 Introduction and background **1**
1.1 An overview of plasma flow and radial electric field studies in fusion devices . . . 1
1.1.1 Resonant magnetic perturbations in Tokamaks . . . 2
1.1.2 Stellarator . . . 5
1.2 The RFX-mod reversed-field pinch . . . 7
1.2.1 Reversed-Field Pinch . . . 7
1.2.2 RFX-mod . . . 10
1.2.3 Experimental measurements of plasma flow and radial electric field . . . 11
1.2.4 Ambipolar potential at RFX-mod . . . 14
1.3 The TEXTOR tokamak . . . 21
1.3.1 The Dynamic Ergodic Divertor . . . 21
1.3.2 Diagnostic tools . . . 22
1.3.3 Numerical tools . . . 23
1.3.4 Studies on 3D structure and transport characteristics of the stochastic layer . . . 24
1.4 Thesis contents . . . 28

2 Benchmark ORBIT-NEMATO **31**
2.1 Introduction . . . 31
2.2 ORBIT . . . 32
2.2.1 Flux coordinates . . . 33
2.2.2 Equations of motion . . . 35
2.2.3 Magnetic field lines . . . 40
2.2.4 Magnetic field perturbation components . . . 44
2.3 NEMATO . . . 45
2.4 Test run . . . 48

2.5 Qualitative benchmark 50
2.5.1 Conserved flux surfaces 51
2.5.2 Poincaré plots, chaotic case 52
2.6 Quantitative benchmark 54
2.6.1 Lyapunov exponent 55
2.6.2 Correlation length 55
2.7 Summary and remarks 58

3 Ion and electron transport with TEXTOR-DED 61
3.1 Introduction 61
3.2 Magnetic configuration 61
3.2.1 Equilibrium 62
3.2.2 Magnetic field perturbations 65
3.3 Test particle simulations 71
3.3.1 Poincaré plots 71
3.3.2 Connection length maps 73
3.3.3 Radial electric field map 82
3.4 Summary and remarks 84

4 Electrostatic response to RMP islands in TEXTOR 87
4.1 Introduction 87
4.2 Poincaré plot 87
4.3 Particle diffusion coefficients 88
4.4 Ambipolar potential 96
4.4.1 The measurements of potential 96
4.4.2 The model for the potential 97
4.5 Summary and remarks 103

5 Conclusions 105

A DED current amplitude and phase 107

B Continuous current density 109

C Nonideal coil configuration 111

D Scalar potential 115

Bibliography 117

List of Figures

1.1 ELMs suppression . . . 3
1.2 ELM cycle . . . 4
1.3 RFP configuration . . . 7
1.4 RFP q-profile . . . 8
1.5 T_e flattening in magnetic island . . . 9
1.6 QSH vs SHAX . . . 10
1.7 RFX-mod machine . . . 10
1.8 Measured plasma flow at RFX-mod . . . 13
1.9 Measured E_r at RFX-mod . . . 14
1.10 RFX-mod electron connection length map . . . 16
1.11 RFX-mod experimental and modeled radial electric field . . . 18
1.12 RFX-mod modeled ambipolar potential . . . 19
1.13 RFX-mod electron root . . . 20
1.14 DED sketch . . . 22
1.15 TEXTOR magnetic topology . . . 25
1.16 TEXTOR n_e and T_e measurements . . . 26
1.17 TEXTOR plasma flow measurements . . . 27
1.18 TEXTOR radial electric field measurements . . . 27

2.1 Poloidal and toroidal flux functions . . . 34
2.2 ORBIT eigenfunctions m=0 . . . 46
2.3 ORBIT eigenfunctions m=1 . . . 47
2.4 SpeCyl run . . . 49
2.5 Mode spectrum of SpeCyl run . . . 50
2.6 Analytic flux surface vs Poincaré . . . 51
2.7 Flux surfaces $m = 0$ . . . 52
2.8 Flux surfaces $m = 1$ . . . 52
2.9 Full spectrum Poincaré plots . . . 53
2.10 ORBIT correlation function . . . 57
2.11 NEMATO correlation function . . . 58

3.1 Circular equilibrium . . . 62
3.2 TEXTOR q profile . . . 63

3.3 TEXTOR Δ profile 64
3.4 TEXTOR g profile 64
3.5 DED coil configuration in the (θ,φ) plane 66
3.6 DED coil non-ideal configuration 69
3.7 TEXTOR $n = 4$ perturbations 70
3.8 TEXTOR $n = 4$ spectrum 72
3.9 TEXTOR $n = 4$ magnetic field Poincaré plot 73
3.10 TEXTOR $n = 4$ kinetic Poincaré plot 74
3.11 TEXTOR electron and ion temperature profiles 75
3.12 TEXTOR electron density profile 76
3.13 TEXTOR electron connection length map 77
3.14 TEXTOR ion connection length map 78
3.15 TEXTOR unperturbed ion connection length map 80
3.16 TEXTOR ion 1D distribution 81
3.17 TEXTOR radial electric field map 83

4.1 TEXTOR $n = 1$ spectrum 88
4.2 TEXTOR $n = 1$ magnetic field Poincaré plot 89
4.3 TEXTOR $m/n = 4/1$ flux surfaces 90
4.4 Archimedes' serpentine surface 92
4.5 Archimedes' serpentine sections 92
4.6 Density profile in the OP of TEXTOR 4/1 island 93
4.7 Deposition points in OP and XP of TEXTOR 4/1 island . . . 94
4.8 TEXTOR D_i and D_e sample 95
4.9 TEXTOR measured plasma potential 97
4.10 TEXTOR measured plasma potential map 98
4.11 TEXTOR radial profile of plasma potential 99
4.12 TEXTOR modeled ambipolar potential map 101
4.13 Modeled radial electric field map 102
4.14 Trapped electron in TEXTOR ambipolar potential 102

Chapter 1

Introduction and background

Purpose of this Chapter is to provide the reader with the background in which the Thesis was developed. Apart from obvious reference to existing literature, the results shown have been obtained by the research groups of RFX and TEXTOR, the PhD student has mainly worked with, before the 3 year PhD period. As such, they do not belong to the original research activity of the Student.

1.1 An overview of plasma flow and radial electric field studies in fusion devices

In the field of magnetically confined nuclear fusion plasmas, recent studies focus on effects of 3D magnetic fields on edge transport and flows. In the tokamak community, resonant magnetic perturbations (RMPs) are 3D fields applied by purpose to stabilize plasmas with high energy confinement (H-modes) with respect to edge localized modes (ELMs) [40, 114]. In fact, ELMs are thought to cause excessive heat loads and damage of materials in the divertor of ITER [75], in a way that ELM control has become mandatory. In other configurations, such as the stellarator [41, 42] and reversed-field pinch (RFP) [140], kinetic properties in the edge are modulated by islands spontaneously resonating in a chaotic layer next to the wall. There is evidence that these edge phenomena influence flow and transport on a global scale, in all of the three magnetic configurations. In the tokamak, RMP application is in many situations directly connected to density pump out, that is, the rapid loss of electron density over the whole radial profile as soon as the RMP is switched [39]. However, also the opposite effect is observed (i.e. density increase) by fine tuning the resonant amplitudes in the applied RMP spectrum [129]. This shows that a direct link between the applied RMP field and edge transport patterns exists in tokamaks. In the RFP the connection between transport, flow and the magnetic structure is even more natural. A transport barrier, related to the $q = 0$ surface,

is located in the plasma edge [124, 11] which determines the shape of density and temperature profiles, and electrostatic properties [29]. In the RFP, this in turn influences many practical aspects of plasma performances, such as access to enhanced confinement regimes [112] and the impact on global power balance [101]. It is worth noting that edge islands are thought to influence the Greenwald density limit in the RFP, through the formation of a localized radiative ring (Multifaceted Asymmetric Radiation From the Edge - MARFE) near the X-points (XP) of the edge islands [137, 98, 97]. Recently, a model of accumulation of particles within edge islands has been proposed for the Tokamak, too [53], resembling a model for the MARFE developed at TEXTOR [136].

The plasma flow is directly linked to the radial component of the edge electric field, E^r, through

$$E^r = \frac{T_i}{Ze}\frac{\nabla p_i}{p_i} + v_\varphi B_\theta - v_\theta B_\varphi \, . \tag{1.1.1}$$

If one can neglect the diamagnetic term $\nabla p_i/p_i$, radial electric field and flow are equivalent. In all of the three configurations (Tokamak, RFP and Stellarator) it has been observed that the presence of a stochastic magnetic topology in the edge influences the sign of E^r. In the Tokamak, the application of the RMP changes the sign of E^r [153] and of the associated flow [26, 151]: generally speaking, E^r changes sign, from $E^r < 0$ to $E^r > 0$, or, if already positive, increases its amplitude. Some changes in the topological properties of the MARFE are seen if RMPs are applied [65]. In the RFP the electric field E^r (and toroidal velocity v_ϕ) is a footprint of the underlying island, and in some cases the modulation is so strong that E^r can change sign along the toroidal angle φ [140]. In the Large Helical Device (LHD) the minimum of E^r is correlated with the radial position of resonances, and shows a scaling with collisionality (more positive E^r at higher collision frequency [67]).

1.1.1 Resonant magnetic perturbations in Tokamaks

Resonant (and non-resonant) magnetic perturbations have been successfully applied in DIII-D [40, 38], ASDEX-Upgrade [132] and JET [73] to control edge-localized modes (ELMs) [159, 131] and/or spread the plasma-wall interaction on a larger surface. In this sense, the particle and power handling in ITER [75, 72] is strictly linked to this type of studies, as explained above. In ITER, uncontrolled type-I ELMs are expected to cause significant impurity influxes into the main plasma and shorten the lifetime of plasma face components (PFCs), including extreme events such as evaporation and melting. The initial physics basis for this scheme of ELM suppression *postulated that radial plasma transport could be enhanced in the pedestal region*

by the creation of an ergodic layer thus controlling the rise of the pedestal pressure and avoiding the occurrence of type-I ELMs [64].

The use of an ergodic field to influence edge transport was originally developed for limiter machines with an ergodic divertor (Tore Supra [54]) or a dynamic ergodic divertor (TEXTOR [46]). In tokamaks with divertor configurations, ELM suppression has been observed to depend on the collisionality level and density in the pedestal region. Fig. 1.1 summarizes the operational space over which type I ELMs are suppressed in present experiments. In DIII-D type-I ELMs in stationary high confinement regimes at high collisionalities have been avoided by applying the perturbation from in-vessel "I-coils" with DC operation and main toroidal symmetry $n = 3$, for high triangularity configurations [38]. These results were then extended to lower collisionalities [40]. ASDEX-Upgrade has also achieved suppression of type-I ELMs by applying edge magnetic field perturbations with $n = 2$ symmetry by in-vessel coils, in high collisionality and high density discharges [132]. JET has also demonstrated a reduction of the type-I ELM energy losses, although without a full elimination of type-I ELMs by the application of $n = 1$ and $n = 2$ perturbations with external mid-plane coils [73].

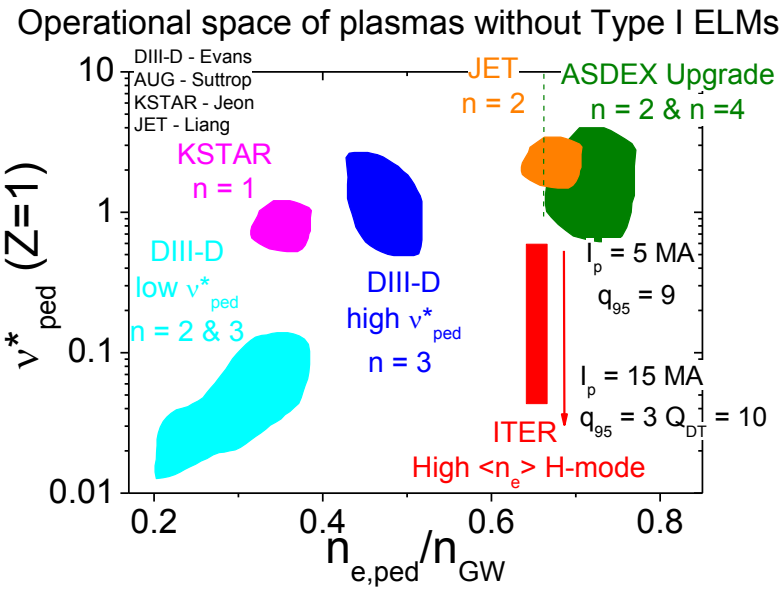

Figure 1.1: Operational space in terms of pedestal collisionality and pedestal density (normalized to the Greenwald value) for regimes in which type-I ELMs have been eliminated by the application of edge magnetic field perturbations in DIII-D, ASDEX-Upgrade, JET and KSTAR.

Presently, the understanding of the edge magnetic perturbation method for ELMs mitigation/suppression is still at a stage which does not allow a robust physics-based extrapolation for ITER. Observations demonstrating the existence of a region with ergodic transport at the edge are now widespread across divertor tokamaks, in which toroidally asymmetric divertor footprints for particle and power fluxes are measured. However, typically, these structures are more predominantly seen in the particle fluxes rather than in the power fluxes and it has not yet been demonstrated that their existence plays a key role on the achievement of ELM suppression itself as opposed to being a feature that is coincidental with the mechanism leading to ELM suppression (such as the appearance of a magnetic island in the pedestal [119]).

The standard picture, developed by Phil Snyder at General Atomics (GA, San Diego, USA) [120], is that ELMs are triggered by the peeling-ballooning modes (PBM). PMB is destabilized by high pressure gradient p'_{ped}, or current, in the pedestal, with the pedestal current J_{ped} being largely bootstrap current, and therefore $j_{\|} \propto \nabla n$. This picture makes it possible to derive semiquantitative models of various types of ELM cycles, which are shown in a schematic diagram in the (p'_{ped}, J_{ped}) space in Fig. 1.2. RMPs, by reducing the pedestal density with the "pump-out" mechanism, bring the PBM back to the stability region. This vision is widely accepted in the

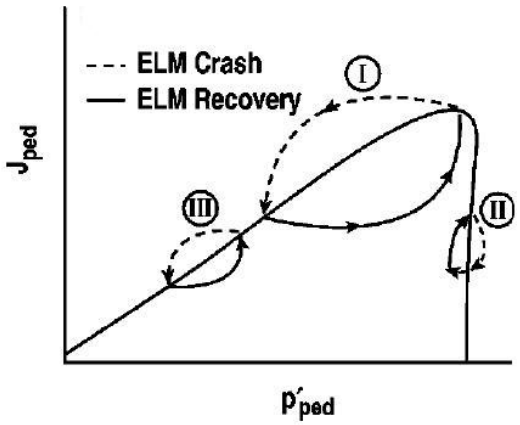

Figure 1.2: Simplified model of a small and large ELM cycles.

Tokamak community, since it takes into account the main phenomenology of ELMs. It is anyway inconsistent with a certain number of observations:

- RMP in ASDEX stabilize ELMs at $n/n_G > 0.6$, as it is evident in Fig. 1.1;

- RMPs itself increase the amount of $j_{\|}$, instead than decreasing it [140, 151, 150];

- PBM are sensitive to pressure gradient: even in DIII-D, despite density decreases, T_e often increases, so that the conclusion on ∇p_e could be questionable.

An other outstanding issue is to determine the *exact topology* of the total 3D field in the pedestal plasma region. The total field is given not only by the sum of the external 3D magnetic field perturbation and the plasma 2D magnetic field, the so-called vacuum approximation. In addition, 3D currents can be induced in the plasma rational surfaces that screen/amplify the resonant components of the external 3D field. The magnitude and location of these response currents are themselves affected by the rotation of the plasma and thus the applied perturbations can be substantially modified from the estimates by the static vacuum model [10, 105, 130]. In addition, a rotating island creates an inductive electric field, whose magnitude is proportional to the rotation frequency [145]. This field adds to the total current and modifies the topology. To our knowledge, the problem of how the inductive field modifies the RMP has been tackled only by Elizaveta Kaveeva and V. Rozhansky at the State Polytechnical Institute in St.Petersburg [68].

In order to clarify these issues a considerable effort has been devoted on effects of 3D magnetic topology on edge transport through flows and radial electric field analysis: especially in the tokamak TEXTOR, detailed features of chaotic layers and islands has been thoroughly investigated (see Sec. 1.3).

1.1.2 Stellarator

In stellarators, studies on the relation between transport and radial electric field (flow) are an outstanding issue as well. Measurements of plasma flow inside the effective last closed flux surface (LCFS) show a radial electric field, E^r, whose dependence on the collisionality is found to be consistent with a neoclassical ambipolar condition [67]. The ambipolar electric field derives from balancing the ion and electron radial fluxes as follows:

$$\vec{\Gamma}_e = \quad -D_e\vec{\nabla}n_e + n_e\mu_e\vec{\mathbf{E}}_A \tag{1.1.2}$$

$$\vec{\Gamma}_i = \quad -D_i\vec{\nabla}n_i + n_i\mu_i\vec{\mathbf{E}}_A \tag{1.1.3}$$

We consider classic diffusion coefficients without magnetic field:

$$D_\alpha = \frac{T_\alpha}{m_\alpha\nu_{\alpha b}} \tag{1.1.4}$$

$$\mu_\alpha = \frac{Ze}{m_\alpha\nu_{\alpha b}} \tag{1.1.5}$$

where "b" = "background", $\nu_{\alpha b}$ are the collisions of the species α with the background. Postulating the quasi-neutrality:

$$\begin{cases} 1. & T_e \gtrsim T_i; \\ 2. & n_e = n_i; \end{cases} \tag{1.1.6}$$

we can then balance the fluxes $\Gamma_e = \Gamma_i$ and get:

$$-D_e \vec{\nabla} n + n\mu_e \vec{\mathbf{E}}_A = -D_i \vec{\nabla} n + n\mu_i \vec{\mathbf{E}}_A \tag{1.1.7}$$

from which we can find the ambipolar electric field:

$$\vec{\mathbf{E}}_A = \frac{-D_e + D_i}{-\mu_e + \mu_i} \frac{\vec{\nabla} n}{n} \,. \tag{1.1.8}$$

Finally, since $\vec{\nabla} n \sim .n_0/L_n \ \vec{\nabla} r$, being L_n the normalized length of the gradient

$$\vec{\mathbf{E}}_A = \frac{D_e - D_i}{|\mu_e| + \mu_i} \frac{\vec{\nabla} r}{L_n} \,. \tag{1.1.9}$$

where we took into account that $-\mu_e = |\mu_e|$. Eq. (1.1.9) shows that

- if $D_e > D_i$, $\vec{\mathbf{E}}_A$ is positive ($E^r > 0$, outwards the plasma core) and it tends to slow down the electron loss rate (electron-root);
- if $D_e < D_i$, $\vec{\mathbf{E}}_A$ is negative ($E^r < 0$, inwards the plasma core) and it tends to slow down the ion loss rate (ion-root) [76].

In the Stellarator generally $D_i \gg D_e$ (neoclassical transport in the "banana" regime) and therefore the ion-root is more common, with relative problem of impurity accumulation in the core, since $E^r < 0$. This accumulation can lead to a collapse of the plasma due to radiative losses, and thus limits high performance plasma discharges in non-axisymmetric devices. At the LHD heliotron, gyro-kinetic simulations of impurity transport including in the model an electrostatic radial electric field generated by an ambipolar potential have been performed. The results show that the ambipolar potential can both increase and decrease the impurity accumulation, depending on the interplay between the radial drift $v_{E\times B}$ arising from the potential, and the ∇B drift, v_d, and the electrostatic and magnetic trapping [52].

On the other hand, in contrast with the neoclassical theory, E^r is positive in the region outside the effective LCFS characterized by ergodic structure for both low and high collisionality regimes. This can be explained by the loss of electrons on the open field lines, leaving the ions behind [67].

At LHD $n/m = 1/1$ magnetic islands can be created by external perturbation coils, and the size of the magnetic island can be controlled by changing the current of the perturbation coils. When the perturbation field is applied ion and electron temperature are observed to flatten inside the magnetic island. The measured poloidal flow is zero at the center of the magnetic island and the direction of the flow is reversed across the center of the island [66].

1.2 The RFX-mod reversed-field pinch

In RFPs the plasma edge is naturally characterized by the presence of islands related to the $q = 0$ surface [124, 11]. The RFX-mod RFP devoted a considerable effort to the description of the topological features of the edge. In this section we will present the RFP configuration, a description of the RFX-mod device and the experimental and simulation results on magnetic and transport properties at the plasma edge of RFX-mod.

1.2.1 Reversed-Field Pinch

The reversed-field pinch is a toroidal configuration for magnetic confinement of fusion plasmas [13, 88]. The term "reversed-field" comes from the fact that the toroidal magnetic field reverses its sign near the plasma edge, as shown in Fig. 1.3; while the term "pinch" addresses the phenomenon where a magnetic field line keeps the plasma away from the wall, increases the plasma density and heats the plasma by adiabatic compression. Since the RFP is

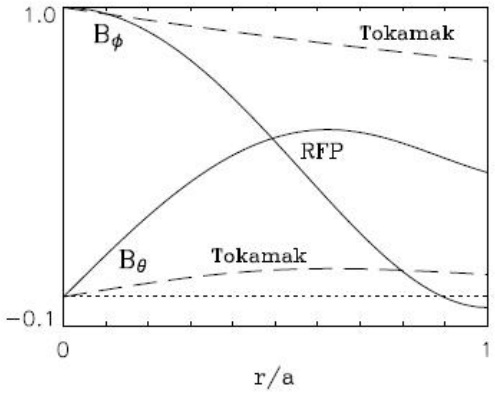

Figure 1.3: Typical radial profiles of the toroidal B_ϕ and poloidal B_θ components of the equilibrium magnetic field in a tokamak (dashed lines) and a RFP (continuous lines). The profiles are normalized to the value of B_ϕ in the plasma center at $r/a = 0$.

an intrinsically low safety factor device (see Fig. 1.4), a broad spectrum of $m = 1$ magnetic modes is resonant throughout the plasma radius, and several $m = 0$ modes are resonant at the reversal radius [89, 90]. As a consequence, a standard RFP operation is intrinsically characterized by a broad spectrum of helical magnetic modes, so-called Multiple Helicity (MH) condition, that lead to current driven instabilities, such as resistive kink/tearing modes. On the one hand, the non-linear effect of kink/tearing modes with $m = 1$ sustains the poloidal current which strongly determines the toroidal

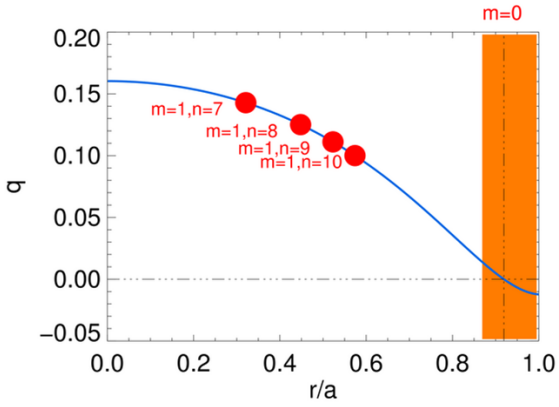

Figure 1.4: The safety factor profile changes its sign at the reversal radius. As a consequence, a broad spectrum of ($m = 1$, $n \lesssim 2R_0/a$) magnetic modes is resonant throughout the plasma radius, and several ($m = 0$, $n \geqslant 1$) modes are resonant at the reversal radius.

field distribution via the so-called RFP dynamo effect (see [19, 12, 33, 91] and references therein). The RFP dynamo sustains the characteristic sign reversal at the plasma edge against resistive diffusion, which would tend to flatten the toroidal field profile, and only a small toroidal flux is produced by external coils. A drawback of the dynamo is that the level of confinement in the RFP is typically not as good as the tokamak one, due to the magnetohydrodynamic (MHD) activity which can develop in such a MH configuration, spoiling the order of the magnetic topology. In fact, the MH character of the magnetic field results in the production of a series of magnetic islands corresponding to the resistive kink/tearing modes. The interaction between these magnetic structures makes the dynamic of the field line chaotic, with detrimental effect on the confinement of energy and particles. The chaos is only minimized by the existence of a transport barrier in the reversal region, due to the presence of $m = 0$ islands [124] at the $q = 0$ surface. The existence of the $m = 0$ islands has been confirmed by the flattening of the electron temperature profile around the reversal when the TS toroidal location corresponds to the O-point (OP) of the $m = 0$ island. This is shown in Fig. 1.5 in Ref. [139].

In recent years, however, a promising way to improve the confinement of RFP plasmas has been extensively investigated, mainly thanks to the implementation of a sophisticated system of feedback control of the MHD modes [92, 93] which allows for a careful tailoring of modes with $m = 0, 1$ and $|n| \leq 23$. The approach exploits the tendency of RFP plasmas to self-organize into quasi-single helicity (QSH) states, as observed in all major RFP devices [36, 78, 81]. The QSH regime is characterized by one (dominant)

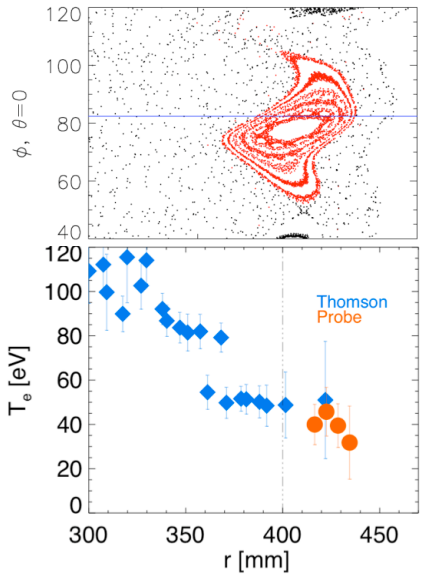

Figure 1.5: The measured electron temperature profile (bottom) flattens out in correspondence of the magnetic island (top).

nonlinearly saturated kink/tearing mode with $m = 1$, of significantly larger amplitude than other ("secondary") MHD modes. These states feature a strong reduction in magnetic chaos and better confinement properties than MH states. In particular, chaos in the core vanishes and conserved helical flux surfaces appear, leaving the peripheral zone still chaotic. Topologically, this configuration is characterized by two magnetic axis (Double Axis, DAx), one corresponding to the equilibrium field and the other to the magnetic island associated with the dominant MHD mode; these axis are separated by a *separatrix* magnetic surface (see Fig. 1.6(a)). Unfortunately, QSH phases are periodically interrupted by magnetic reconnection events [23] associated with enhanced dynamo modes activity and formation of current sheets [95, 160] during which the secondary modes increase and a back-transition to MH is observed. A considerable effort is being devoted in RFX-mod to avoid back transitions and lengthen the QSH phase, e.g. through the optimization of the active feedback system [80, 155], the wall conditioning with Lithium [101] and optimized control of the equilibrium and q profile [8].

QSH plasmas are preferentially observed when increasing the plasma current [95]. In particular, the occurrence of internal transport barriers is observed when the so-called Single Helical Axis (SHAx) state [78, 79] is achieved, where all of the secondary modes almost vanish and only the dominant remains active. In the SHAx state, the magnetic separatrix merges with the main magnetic axis and a plasma column with a single helical axis is

obtained (see Fig. 1.6(b)). This is the so-called dominant mode separatrix expulsion process [37], which in Hamiltonian systems is connected to an enhanced resilience to chaos [49].

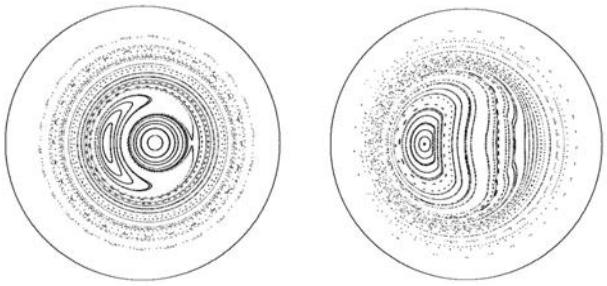

(a) (b)

Figure 1.6: (a) QSH and (b) SHAx topological configurations.

1.2.2 RFX-mod

The RFX-mod (Reversed Field Experiment modified) [121], located at the Istituto Gas Ionizzati (IGI) of the Italian Consiglio Nazionale delle Ricerche (CNR) in Padova, is the biggest RFP in the world with major plasma radius $R = 2.0\ m$ and minor radius $a = 0.46\ m$ (see Fig. 1.7). The

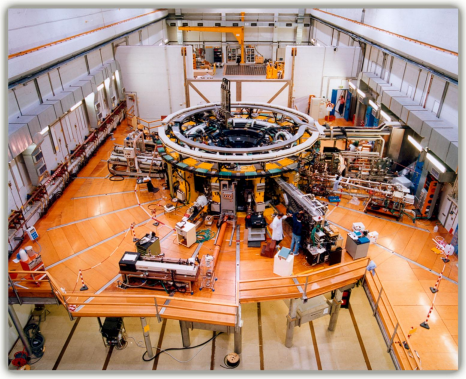

Figure 1.7: The RFX-mod machine.

plasma current can reach up to $I_p = 2\ MA$ with pulse length of up to $1\ s$. The machine is composed by an all-welded, rigid vacuum vessel made of INCONEL 625 [55]. The vessel is protected from the plasma by means of a first wall composed by 2016 graphite tiles [154]. Graphite has been chosen because it sublimates at a high temperature, and for its low atomic number Z which limits radiative losses. A stabilizing shell, made of copper and

3 mm thick, is located at about 0.56 m from the toroidal axis with the main purpose of passively stabilizing MHD ideal instabilities in the first $\sim 50\ ms$ of the plasma discharge, being then superseded ed by the active feedback control system [121]. This shell is enclosed by a mechanical structure which bears the weight of the vacuum vessel and of the toroidal windings. Magnetizing coils provide the time varying magnetic flux that induces the plasma current during the discharge [128]. It is composed by 40 coils that can carry a maximum current of 50 kA. Toroidal field coils (a set of 48 coils uniformly distributed along the toroidal direction, that surround the vessel and the shell) are designed to generate the toroidal magnetic field needed to set-up and maintain the discharge (up to 0.7 T). Field shaping coils (set of poloidal coils) are designed to generate a vertical field whose aim is to control plasma position during the discharge. In order to control the instability arising for $t > 50\ ms$, RFX-mod is equipped with a complete set of 192 saddle coils (4 poloidal $\times$ 48 toroidal), with a real-time feedback control of instabilities with $m = 0, 1$ and $|n| \leq 23$ [80]. The feedback system was tested in RFX-mod with an overall, decisive improvement of electron temperature, pulse length and overall plasma confinement, with respect to the old, thick-shell RFX [92, 83, 93]. After a brief period of initial operations with the virtual shell [93] it was realized that an intrinsic limitation, i.e. aliasing of the side-band harmonics generated by the discrete coils system coupled with coils with the same periodicity, did not allow further improvement. To overcome this systematic limitation, the aliased sidebands contribution (estimated from the coil currents) is subtracted from the measurements. The "cleaned" measurements are used as the new, reference feedback variable. The scheme is called Clean mode control (CMC), and more details are reported in Refs. [80, 156].

1.2.3 Experimental measurements of plasma flow and radial electric field

Historically, at the RFX-mod RFP studies of plasma flow and radial electric field were initially carried on in relationship with the density limit issue. The density limit (or "Greenwald" limit) still defies a comprehensive theoretical explanation, even if in tokamaks and RFPs it can be characterized phenomenologically in terms of the Greenwald density [63], namely $n_G = I_p/\pi a 2$ (n_G in $10^{20} m^{-3}$, I_p in MA). Density is then often expressed as a ratio n/n_G, which in the RFX is given by

$$\frac{n_e}{n_G} = \frac{1}{15} \frac{n_e(10^{19}\ m^{-3})}{I_p(MA)}\ . \tag{1.2.1}$$

Given the proportionality $I_p \propto B$, in the RFP $n/n_G \approx n/B$, ratio of the average density to the equilibrium magnetic field. In the RFP, a central role

in determining the Greenwald limit is played by the edge density: by increasing n_e/n_G, temperature decreases and density increases in the edge. The edge density accumulation takes place at $n_e \approx n_G$ in the chaotic, MH state, being preceded by a back-transition from the QSH to MH at $n_e/n_G \sim 0.35$ [112, 99]. The edge density accumulation causes an increase in the total radiation and $O_{IV} - O_{VI}$ line emission, in the shape of a ring localized toroidally and poloidally symmetric ($m = 0$), in analogy with the MARFE [74, 108, 117] in tokamaks, which is a structure characterized by very low temperature and strong recombination, toroidally symmetric and poloidally localized ($n = 0$). The difference between the RFP and tokamak MARFEs (poloidally and toroidally symmetric, respectively) is only apparent, since the geometry of the MARFE follows the equilibrium B field in the edge (poloidal in the RFP, toroidal in the Tokamak). It is the MARFE in the tokamak, and its poloidal analogue in the RFP, which ultimately causes the discharge termination (often disruptive in the tokamak, never disruptive in the RFP [137]). The huge edge density peak measured in the RFP at $n_e/n_G \sim 1$, which is the initial trigger of the whole density limiting phenomenon, cannot be sustained by local diffusion, $D\partial n_{edge}/\partial r$ [111]. A breakthrough for the explanation of this apparently odd phenomenon has been the analysis of the toroidal component of the flow.

In Fig. 1.8(a) measurements of the toroidal component of plasma flow, v_φ, as a function of the helical angle u, in the case of a $m/n = 0/1$ island in the RFX-mod are shown. We recall here that in the RFP (v_r,v_φ) are the components of the perpendicular flow. The flow is measured by a gas-puff imaging diagnostic (GPI) [3, 5], at a single point toroidally and at a radius $r = 0.98a$. Since the island is slowly rotating in the lab frame of reference, to map the measurement (which is a function of time) on the topology of the island, it is convenient to use the definition of helical angle $u(\theta;\varphi;t) = m\theta - n\varphi + \omega_{mn}t$, which in the case of a 0/1 island simplifies to $u_{0,1} = -\varphi + \omega_{0,1}t$. One can interpret $u_{0,1}$ as the toroidal angle in a frame of reference rotating together with the island. Formally, it can be shown that the formula for $u_{m,n}$ is obtained quite naturally by expressing the Hamiltonian of field lines in action-angle variables (see Sec. 2.2.3). In this way, any island that develops at a given m/n resonance has a similar shape, when plotted on the plane (u, ψ), with ψ the magnetic flux coordinate (for more details about the definition and use of the helical angle see Ref. [140]).

The flow is generally negative over the helical angle, which would correspond to $E^r < 0$: this is the usual situation in RFX (see e.g. Fig.7(c) and (d) in Ref. [127]), and has been interpreted in the past in terms of finite ion Larmor radius effects [9]. But there is a large portion of the toroidal angle where $v_\varphi > 0$ ($E^r > 0$) with two null points that define a huge convective cell (diameter ~ 3 m). This is also confirmed by measurements showing that E^r change sign in RFX along φ [21, 102]. Looking at the arrows in Fig. 1.8(a), it is easy to recognize a "source" and a "stagnation" point: the

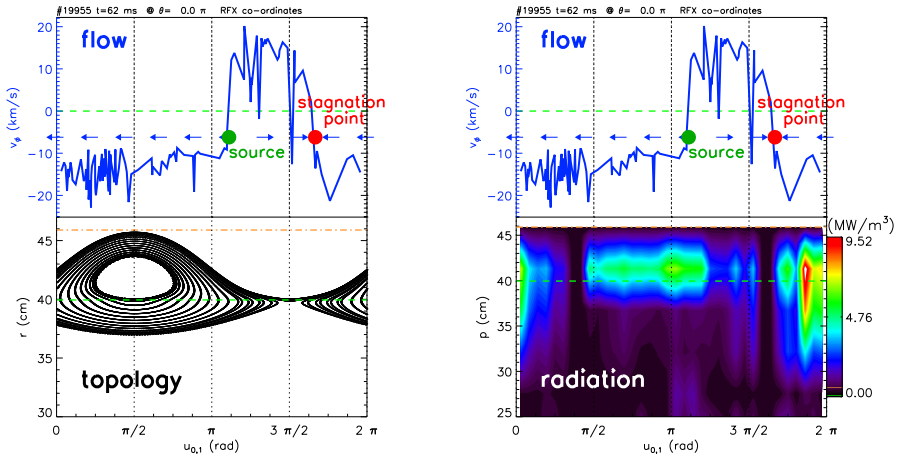

(a) (b)

Figure 1.8: On the top the measured toroidal flow as a function of the helical angle $u_{0,1}$. On the bottom the corresponding 0/1 island (a) and the measured total radiation (b) on a map (r,u). The zeroes of the flow are marked as bullets, and correspond to a source and stagnation point for plasma density (green and red, respectively).

center of the convective cell corresponds to the X-point (XP) of the 0/1 island, which is plotted in Fig. 1.8(a), bottom panel, while the OP corresponds to the baseline $E^r < 0$. Measurements of the radial component of the velocity, v_r, confirm the presence of a convective cell [30]. Namely, the flow possesses the same symmetry as the magnetic island. The connection with the Greenwald limit lies in the fact that the stagnation point is always found to coincide with the poloidal MARFE which develops at $n/n_G \geq 0.8$, as shown in Fig. 1.8(b) [97, 98].

To better understand the topology of the E^r field, it is convenient to map the measured values (as a function of u) onto an edge flux surface calculated with VMEC/V3FIT: the adaptation of VMEC to the reversed field pinch is a recent addition in the framework of a collaboration between Consorzio RFX and the Auburn University [135]. The result is shown in Fig. 1.9(a): in the color map, blue corresponds to the potential well ($E^r > 0$ at $r = a$) while red corresponds to the potential hill ($E^r < 0$ at $r = a$). The potential well corresponds to the XP of the island, which, in terms of flux surfaces, is the region where the annulus is shrunk: thus, the symmetry of E_r is the same as the magnetic island. A nice proof that this is a general property has been obtained recently with the complete toroidal array of Langmuir probes, called ISIS (Integrated System of Internal Sensors) [118]. By exploiting the technique of a rotating 1/7 island and the mapping on the helical angle and the VMEC flux surface, one can obtain the picture

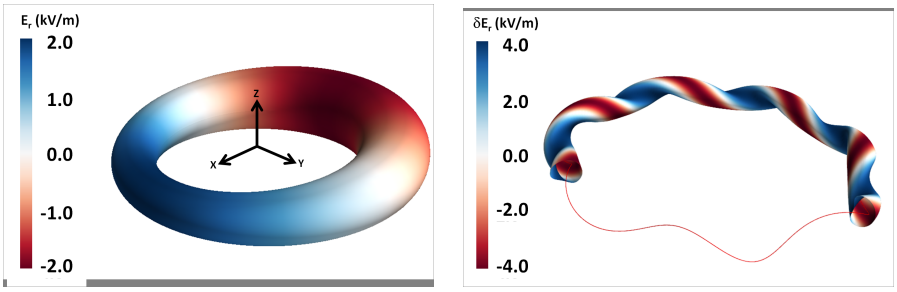

(a) (b)

Figure 1.9: (a) Measurements of $E^r \approx v_\varphi B_\theta$ mapped onto an edge flux surface calculated with VMEC/V3FIT in the 0/1 symmetry; (b) E_r measured with the array of internal sensors (ISIS), mapped onto a helical flux surface calculated with VMEC/V3FIT.

shown in Fig. 1.9(b): in this case, helical flux surfaces refer to the RFP SHAx state. In the SHAx state, even if the island is resonating in the core plasma, the helical ripple at the edge is comparable to the 0/1 case, and it is capable of modulating edge kinetic quantities as it has already been shown in Fig. 1.8(a). Again, analogously to Fig. 1.9(b), the E_r field has the same symmetry as the island, and in this case the potential well appears as a blue ribbon winding up the helical surface (For a detailed discussion of the ISIS measurements in the helical symmetry of RFX, see Ref. [140]). The pictorial view of Fig. 1.9 makes immediate that the electrostatic potential is parent to the magnetic topology: in particular, Fig. 1.9(b) shows an impressive similarity with simulations of ambipolar potential in the stellarator [52] (even if in RFX-mod case we are dealing with actual measurements mapped onto a helical equilibrium). But Fig. 1.9 shows also deeper result: the values of E^r are not constant on a flux surface, meaning that if one searches for an analytic form of the potential, this must not be a flux function, $\Phi \neq \Phi(\psi)$.

Summarizing, experiments show that magnetic islands spontaneously resonating in the reversed-field pinch are associated with macroscopic fluctuations of the flow (up to $\sim$ 20 km/s); the symmetry is the same as the generating island (1/7 low density, and 0/1 at high density in the RFX), and values of E^r are not constant on a flux-surface. In some cases (0/1 at high density) the coherent fluctuations of the flow are also associated to the Greenwald limit through the mechanism of the stagnation point and the MARFE.

1.2.4 Ambipolar potential at RFX-mod

To investigate the physics underlying the observations presented in Sec. 1.2.3, the guiding center Hamiltonian code ORBIT [141] has been applied. ORBIT

exploits a rather unique feature of the RFP: *the precise knowledge of the radial structure (eigenfunction) of the saturated, almost stationary spectrum of tearing modes*. This is a striking advantage with respect to Tokamaks, where the determination of the "plasma response" is still an issue, and makes the RFP an ideal test-bed to study the behavior of RMPs. Eigenfunctions are evaluated for RFX-mod with the code NCT [157], which solves the Newcomb's equations [86] in toroidal geometry (the constraint are the magnetic fluctuations measured at the conductive shell). ORBIT adopts the so-called "Boozer" coordinates [15]: as radial coordinate the poloidal flux ψ_p, labeling the poloidal magnetic surfaces, the poloidal angle, θ, the general toroidal angle ζ which is an approximation of the toroidal angle, φ. (We will anyway explain extensively the code structure in Sec. 2.2.) ORBIT allows to perform magnetic field and "kinetic" Poincaré plots, and to study the parallel connection length to the wall, $L_\parallel$. The connection length is a standard metric used in the context of tokamak stochastic edge, to determine the topology and width of the scrape-of layer (SOL): short-connection length regions are called "laminar" zones, since are characterized by large plasma wall interaction and low electron temperatures, while long-connection length regions are called "ergodic", in the sense that are connected to the core, and are characterized by large heat fluxes and high temperature (see Sec. 1.3).

In Fig. 1.10 is shown the $L_\parallel$ map for the RFX discharge shown in Fig. 1.8(a). To facilitate the comparison with the magnetic topology, an equatorial Poincaré section is over plotted. The Poincaré is done with the 0/1 mode only, to highlight the dominant helicity, while $L_\parallel$ is calculated with the full mode spectrum taking into account the recycling of the wall, which, at least in the RFX, is almost unity (it means that particles released from the wall make up almost the totality of plasma density [101]). The domain for the $L_\parallel$ calculation is limited radially by $\psi_{p,2} < \psi_p < \psi_{p,1}$: particles (electrons) are deposited at $\psi_{p,1} = 0.093$ (deposit surface), recycled by the wall, and recovered at their exit $\psi_{p,2} = 0.079$ (recovery surface). There is a modulation of $L_\parallel$ with the same symmetry of the 0/1 mode. Two regions can be seen: a low-connection length region ($10 - 100\ m$), corresponding to the OP of the island, and a long-connection length region ($L_\parallel > 10\ km$) near the XP. Similarly to the tokamak, the RFX edge is composed of a "laminar" and "ergodic" region. It is worth noting that a similarity with tokamaks, with a separation in laminar and ergodic regions along the helical angle, can be drawn also in the helical, 1/7 state of the RFX, as shown in [140]. The physical reason is that electron orbits have a longer period around the XP: this is the classical pendulum, which shows a period diverging to infinity as approaching the XP along the separatrix [22]. With $m = 1$ perturbations to the 0/1 island [124] and electron collisions, the period around the XP does not diverge, but it is still larger than the period around the OP. In addition to this, the 0/1 island touches the wall [112], so that the period around the OP is further decreased.

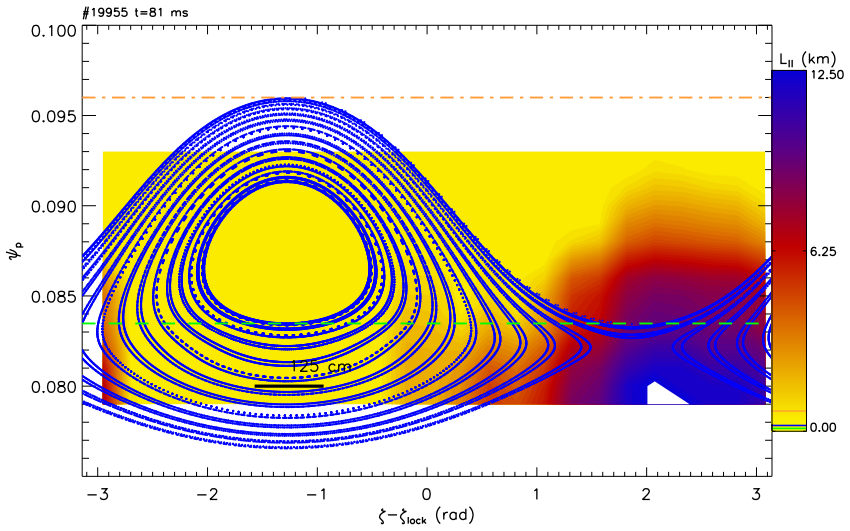

Figure 1.10: Contour plot of the connection length $L_\parallel$ defined as the distance (parallel to the magnetic field) traveled by electrons from the deposit surface $\psi_{p,1} = 0.093$ to the recovery surface $\psi_{p,1} = 0.079$. The map describes $L_\parallel(\zeta_i, \psi_{p,j})$, each point $(\zeta_i, \psi_{p,j})$ of the grid being the initial toroidal angle and an intermediate radius where $L_\parallel$ is recorded. The dashed, horizontal line corresponds to the reversal surface, the dash-dotted line to the wall, $\psi_p = \psi_{p,w}$. Over plotted, a Poincaré section of the 0/1 island. The Poincaré is done with the 0/1 mode only, the $L_\parallel$ with the full spectrum of tearing modes.

On the basis of these results, a model of electrostatic potential to include in ORBIT to get the ambipolar condition $\Gamma_e = \Gamma_i$ at the recovery surface $\psi_{p,2}$ can be built up. The simplest geometry is that of RFX with the 0/1 mode, so that the helical angle is simply $u = -\zeta$ (Figs. 1.8(a) -1.9(a) - 1.10). The approach exploits the fact that the GC Hamiltonian (see Sec. 2.2) can be written as $H = 1/2\rho_\parallel^2 B^2 + \mu B + \Phi$, where $\rho_\parallel = v_\parallel/B$ and μ is the magnetic moment: in this way, if an analytical guess of the potential is available, Φ can be added easily to the GC equations of motion [141], as it will be shown in detail in Sec. 4.4. This is not a self-consistent approach, but it is easy to implement, and requires small computational time, since electron and ion simulations can be run separately. Since Φ is a model of ambipolar potential, it will be described on the plane perpendicular to the equilibrium field, which in the RFP edge is B^θ. Therefore, $\Phi = \Phi(\psi_p; \zeta)$ and $\delta\Phi/\delta\theta = 0$. The radial profile of the model Φ can be derived from existing data from Langmuir probes, showing that E^r has an almost constant value in the region $0.85 < r/a < 1$, and changes sign according to the phase of the 0/1 mode (see Fig. 1.11(a), which is adapted from Ref. [102]). Therefore,

E^{ψ_p} is

$$E^{\psi_p} = E_a + \frac{1}{2} E_{r,w} \left[\tanh \left(\frac{\psi_p - \psi_{p,rv}}{\sigma_{\psi_p}} \right) + 1 \right] , \tag{1.2.2}$$

where $\psi_{p,rv}$ is the reversal surface (resonance of the 0/1 mode and therefore center of the potential well), and σ_{ψ_p} is the radial (half) width of the potential well, chosen to be $\sim 2.5\rho_i$. This choice is consistent with Fig. 1.11(a) and the width of the domain in Fig. 1.10 (in fact, $\psi_{p,1} - \psi_{p,2} \sim 2\sigma_{\psi_p}$). Eq. (1.2.2) takes the form of Fig. 1.11(b), dash-triple dot line: in the potential well (i.e. center of the convective cell) the radial electric field in the edge is positive, and changes sign at $\psi_p = \psi_{p,rv} - \sigma_{\psi_p} = 0.077$, which corresponds to $\sim 38\ cm$ ($r/a = 0.83$). In Eq. (1.2.2) the value E_a is chosen to match the values of $E_r(a)$ far from the convective cell (open circles in Fig. 1.11(a)), and is a value that levels off in the core (it does not make any role in computations, since these simulations never explore $\psi_p < 0.079$). In the end, the only free parameter left is $E_{r,w}$, which plays the role of the amplitude of the ambipolar potential.

The angular dependence is derived from the GPI data shown in Fig. 1.8(a), and is modeled as

$$\mathcal{A}(\zeta) = 2e^{-(\zeta-\zeta_0)^2/2\sigma_\zeta^2} - 1 , \tag{1.2.3}$$

which fundamentally is a 0/1 dependence along the toroidal angle ζ (the same as the helical angle), with the possibility of choosing the toroidal amplitude of the potential well, σ_ζ. Following the GPI data, σ_ζ is chosen $\sigma_\zeta = 50°$ (whole width 100° toroidally). The free parameter in Eq. (1.2.3) is the phase of the ambipolar potential, ζ_0.

By combining Eq. (1.2.2) and Eq. (1.2.3) one obtains

$$\Phi(\psi_p; \zeta) = -E_a \psi_p + V(\psi_p)\mathcal{A}(\zeta) , \tag{1.2.4}$$

where $V(\psi_p)$ is the integral of Eq. (1.2.2)

$$V(\psi_p) = -\frac{1}{2} E_{r,w} \left[\sigma_{\psi_p} \log \left(\cosh \left(\frac{\psi_p - \psi_{p,rv}}{\sigma_{\psi_p}} \right) \right) + \psi_p \right] . \tag{1.2.5}$$

Details of the derivation of this model can be found in Ref. [123]. A contour plot of the potential in Eq. (1.2.4) is shown in Fig. 1.12(a), for a guess of the phase $\zeta_0 = 3/2\pi$. In the edge, a potential hill (at $\zeta = \zeta_0 - \pi$) and a potential well (at $\zeta = \zeta_0$) are visible. Looking more in detail (white inset), a feature of this potential model is the presence of a saddle point at $\zeta = \zeta_0$: along the radius the potential shows a peak at $\psi_p = \psi_{p,rv}$, while along the angle it has a minimum at $\zeta = \zeta_0$, which is evident as an X-shaped contour in the inset of Fig. 1.12(a). Actually, the equipotential surfaces already define the shape of the convective cell measured by the GPI in RFX, and the $\vec{E} \times \vec{B}$ flow can be defined as the motion of electrons and ions along the equipotential surfaces, $\vec{v}_{E\times B} \cdot \nabla\Phi = 0$, that conserves kinetic energy and can drive the macroscopic

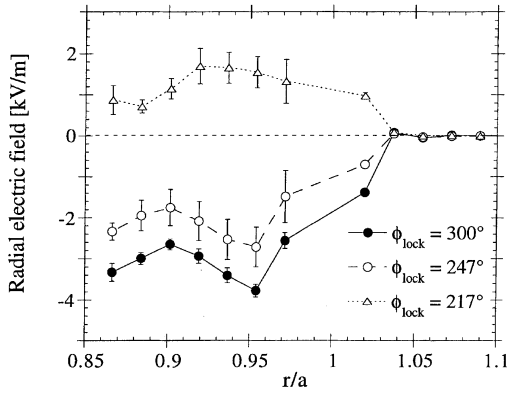

(a)

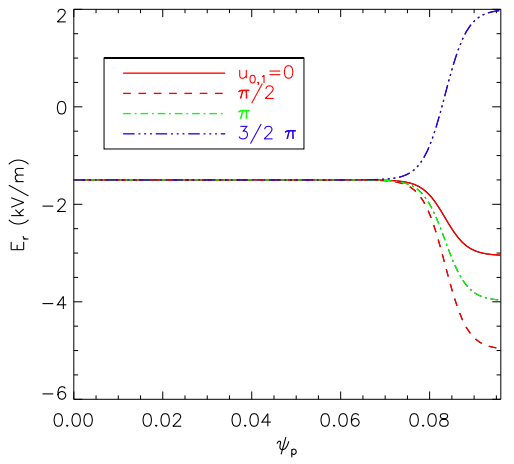

(b)

Figure 1.11: (a) Experimental radial profiles of the radial electric field E^r, at different toroidal angles; (b) The model for E_r derived from measurements.

transport features which are seen near the Greenwald limit [98, 127]. The presence of the convective cell is made evident by differentiating Eq. (1.2.4), and obtaining the map of (E^ζ, E^{ψ_p}), shown in Fig. 1.12(b) as the expanded inset of panel (a): the radial electric field is negative, except for the inner part of the convective cell, where $E^r > 0$.

The analytical model for the potential can now be used to get ambipolarity in ORBIT runs: the domain is the same as in Fig. 1.10, with $\psi_{p,2} < \psi_p < \psi_{p,1}$. The technique is similar to that used in the stellarator community: vary the free parameters until $\Gamma_e = \Gamma_i$ (the "root" in the stellarator jargon). In RFX-mod case is only slightly more complicated, since

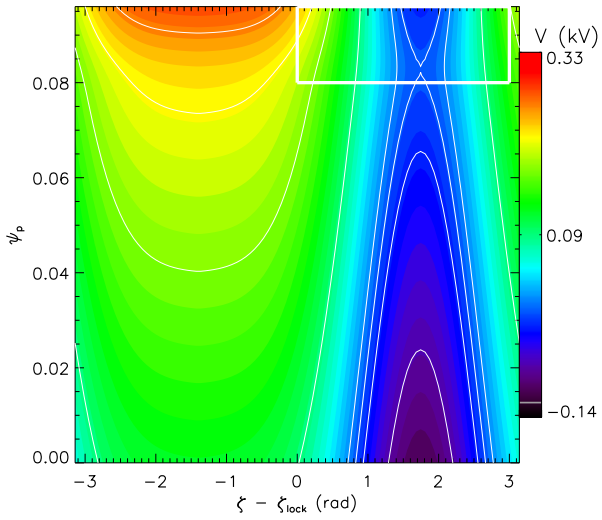

(a)

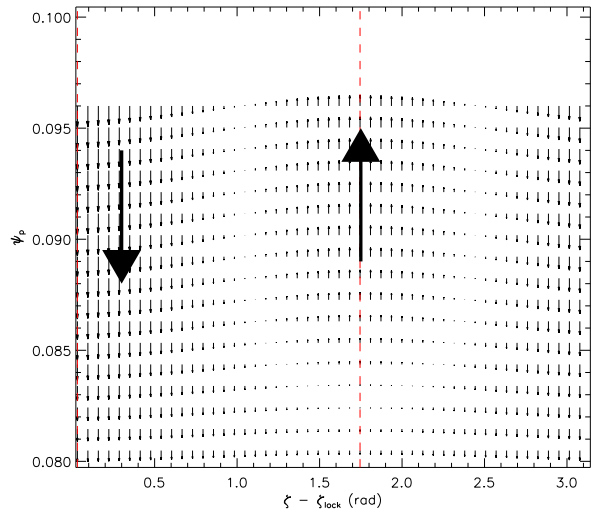

(b)

Figure 1.12: (a) Contour plot of the model of potential, in the 0/1 symmetry. The phase has been chosen as $\zeta_0 = 3/2\pi$, in order to match the experimental data. The white inset encloses the region of the convective cell measured by the GPI diagnostic, shown in Fig. 1.8(a); (b) By differentiating the potential, we get the electric field in the plane perpendicular to $\vec{B}$, with its two components (E^ζ, E^r). Note that the region of $E^r > 0$ corresponds to the center of the cell, or, equivalently, to the potential well.

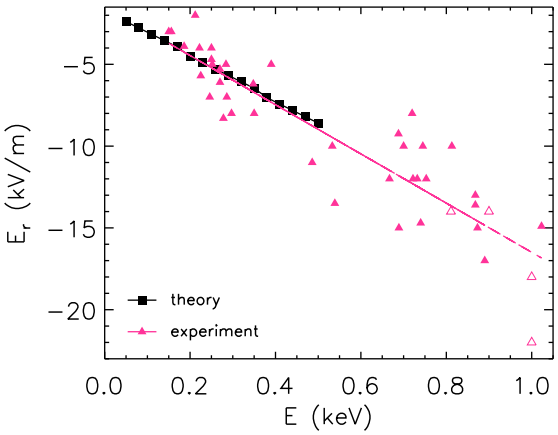

(a)

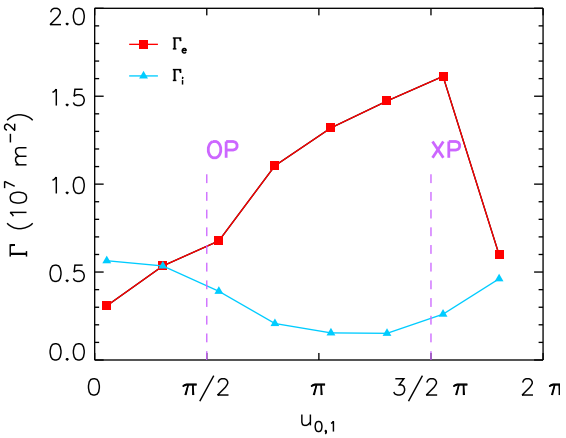

(b)

Figure 1.13: Determination of the potential amplitude and phase: (a) Radial electric field at the wall as a function of electron energy (code: squares, data: triangles); (b) electron and ion flux as a function of the potential phase. The phase has been expressed in terms of helical angles, so that $u_{0,1} = \pi/2$ corresponds to the OP of the 0/1 island, while $u_{0,1} = 3/2\pi$ corresponds to the XP (the same as in Figs. 1.8(a) and 1.10). ORBIT gives as a result of an ambipolar condition an amplitude well in agreement with data, but a phase which corresponds to the OP of the island, and not the XP, as in Fig. 1.8(a)

two parameters, amplitude and phase, exist. A basic requirement of the potential allows to guess the potential amplitude: it must be able to trap electrons. Then the free parameter $E_{r,w}$ varies in single-particle runs (no perturbations), until electrons are trapped around $\zeta = \zeta_0 - \pi$ (the potential hill). Finally varying the electron energy, one obtains another value of the

amplitude. The radial electric field at the wall, $E^{\psi_p}(\psi_w) = E_a - E_{r,w}$, can be computed as a function of the electron energy: the result is shown in Fig. 1.13(a), which is the rather expected linear dependence with energy. In fact, one can expect the radial electric field to be $E^{\psi_p}(\psi_w) = -T_e/2e\sigma_{\psi_p}$. Inserting the numerical value for σ_{ψ_p} , one obtains the values shown in Fig. 1.13(a). E^r can be also evaluated from the GPI measurements of flow neglecting the diamagnetic term. The result are the purple triangles of Fig. 1.13(a). There is a striking agreement between theory and experiment, showing that the E^r field at the edge of RFX is likely to be ambipolar.

The phase can now be determined with the standard technique: for $E = 260\ eV$ one gets $E_{r,w} = 4\ kV/m$, and ζ_0 is a free parameter. Let 6×10^4 particles diffuse between the deposit $\psi_{p,1}$ and the recovery surface $\psi_{p,2}$, subject to the full spectrum of perturbations and collisions (pitch angle scattering only). Each run is performed by varying ζ_0: look at the fluxes Γ_e and Γ_i at the recovery surface, and find a "root" $\Gamma_e = \Gamma_i$ as a function of ζ_0. The result is shown in Fig. 1.13(b) as a function of the helical phase $u_{0,1}$ (given by $u_{0,1} = -\zeta_0$). There is one root, and ambipolarity is reached at $u \approx \pi/2$, i.e. when the potential well is in the proximity of the OP of the magnetic island. The result is not unreasonable, since the potential well means $E^r > 0$ (see Fig. 1.12), and *a positive electric field avoids further losses of electrons where D_e is already large*, as seen in Tokamaks with the RMP [107] and in the electron-root of Stellarators (see Sec. 1.1.2). Nevertheless, measurements in RFX show the opposite, the potential well stays at the XP of the 0/1 island (Fig. 1.8(a)).

1.3 The TEXTOR tokamak

The TEXTOR tokamak (Tokamak Experiment for Technology Oriented Research) [85] is a medium-sized tokamak with major plasma radius $R = 1.75\ m$ and circular plasma cross section, located at the Research Centre Jülich, Germany at the Institute for Energy Research - Plasma Physics. The plasma is limited on the High Field Side (HFS) by the Dynamic Ergodic Divertor (DED) target located at $r = 0.477\ m$, and on the Low Field Side (LFS) by the movable ALT-II target located at $r = 0.45 \div 0.47\ m$. The toroidal field at the plasma center reaches up to $B_t = 3\ T$ inducing plasma currents of up to $I_p = 800\ kA$ with pulse length of up to $10\ s$.

1.3.1 The Dynamic Ergodic Divertor

The DED [44] consists of 16 helical coils covered by ceramic tiles and by 2D shaped graphite tiles for protection during plasma discharges, forming a smooth toroidal surface, that is, the *divertor target plate*. They are installed on the inboard side of the TEXTOR vessel at $r = 0.5325\ m$ and aligned parallel to the magnetic field lines on the $q = 3$ surface (see Fig. 1.14). The

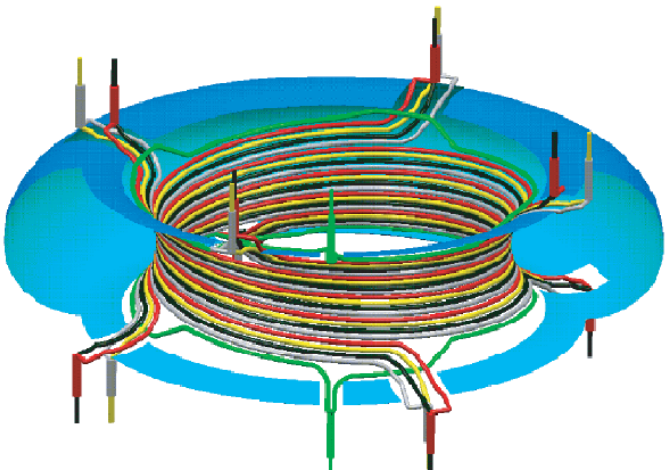

Figure 1.14: Sketch of the DED coils.

coils are bundled such that the outlets are at 4 toroidal locations, 4 on top of TEXTOR and 4 at the bottom. This grouping of the coils is technically favorable, but it requires the installation of a pair of compensation coils. Each coil performs one toroidal turn and covers a poloidal angle of $\Delta\theta \approx 70°$ (including compensation coils $\Delta\theta \approx 80°$). This wiring of the coils creates a perturbation field resonating at the plasma edge around the $q = 3$ surface (at $r = 0.43 \approx m$) with poloidal and toroidal base mode numbers $m/n = 3/1,\ 6/2,\ 12/4$, called DED mode operations. Each one is limited to DED currents $I_d^{12/4} = 15\ kA$, $I_d^{6/2} = 7.5\ kA$ and $I_d^{3/1} = 3.75\ kA$. The two compensation coils are switched on during the $m/n = 12/4$ mode operation to compensate the net perturbation field of $n = 0$ toroidal mode. Coil currents can be either static or dynamic with rather large frequencies, of the order $1 \div 10\ kHz$. The original idea of the DED is to introduce a stochastic layer next to the wall of a tokamak, in order to spread heat and particle fluxes over a large area of the divertor target plate. This increases the scrape-off layer (SOL) width, which is a good condition for improving plasma-wall interaction (in some sense, the whole idea of the tokamak divertor, and of the "island divertor" of W7-X, is to enlarge the volume of the SOL [41]). Since the plasma exposed surface area is completely determined by the helical pattern of the magnetic field structure, this scenario is also referred to as *helical divertor*.

1.3.2 Diagnostic tools

In order to resolve experimentally the 3D structure and correlated transport characteristics of the stochastic layer, TEXTOR is equipped with highly

spatially resolved edge diagnostics. The electron density, n_e, and the electron temperature, T_e, are measured through an active beam emission spectroscopy (BES) on thermal helium beams [116], a Thomson scattering system [138], and an electron cyclotron emission imaging (ECE-I) system [94]. The first two diagnostics perform radial measurements with high spatial resolution ($\sim 1\ mm$): the BES at $\theta = 185°$ on the HFS and at $\theta = 5°$ on the LFS, and the Thomson scattering at $\theta = 280°$. The ECE-I system has a 2D spatial resolution in radius and poloidal angle allowing a simultaneous two dimensional observation. Finally, TEXTOR is equipped with CCD cameras with viewing chords tangentially along and perpendicular to the DED target. In case of rotating RMP fields measurements of n_e and T_e are performed with the supersonic helium beam diagnostic (SHE) [70], optimized for high temporal and radial resolution ($\Delta t = 20\ \mu s$ and $\Delta r = 2\ mm$), enabling the detection of fast small scale variations of the observables in the plasma edge.

Besides these, more diagnostic permits to measure plasma flow and plasma potential at the edge of the device. An hydrogen diagnostic beam performs charge exchange recombination spectroscopy (CXRS) and measures the toroidal and poloidal rotation as well as the ion temperature on fully ionized carbon by means of Doppler shifted spectra [25]. Two Langmuir probe arrays installed at the LFS at two different toroidal locations covering both the ergodic and the laminar zones, allows to measure the floating potential, from which together with the electron temperature, one can derive the plasma potential [153].

1.3.3 Numerical tools

A set of numerical tools has been adapted to TEXTOR to support and model the experimental data provided by diagnostics. At TEXTOR the ATLAS [45] and GOURDON [35] codes for magnetic topology modeling, and the EMC3-EIRENE code [69], for transport modeling of the 3D stochastic edge layer, are deeply employed. ATLAS, a simplecting mapping code for magnetic field lines, and GOURDON, a numerical field line tracing code, are used to reconstruct the magnetic topology of the edge through the so-called *Poincaré plots*, showing the intersections of the magnetic field lines with an arbitrary poloidal plane and to study the transport features of the stochastic regions producing the so-called laminar plots. The laminar plot quantifies the connection length, L_c, of the field lines as field line length from target to target. The approach of both the codes uses the vacuum approximation, i.e. a linear superposition of an equilibrium magnetic field and an external perturbation field. EMC3/EIRENE is a fully 3D Monte Carlo code based on a kinetic neutral particle transport model that solves the Braginskii fluid equation (EMC3) taking into account the particle, energy and momentum sources and sinks in front and on the wall (EIRENE). Numerical simulations realized with the EMC3/EIRENE code show the magnetic topology,

calculated by superposing the external RMP components, is in fair agreement with experimental findings in highly resistive edge plasmas with static RMP [115].

1.3.4 Studies on 3D structure and transport characteristics of the stochastic layer

The electron density and temperature profile reactions with static RMPs are compared with the modeled magnetic "vacuum" topology. The combination of ATLAS and GOURDON results demonstrate that the magnetic topology consists of three domains with very different transport characteristic (see Fig.1.15):

- at the innermost perturbed rational flux surface with sufficient RMP field amplitude, at small radii (i.e. $r \approx 0.35\ m$), magnetic islands are created: this is the *main island chain*;
- further outside, a fragmented remnant island appears: these are the *remnant islands*;
- Finally in the outermost region island chains from neighboring rational flux surfaces overlap and forming the so-called *laminar zone* characterized by ergodic stochastically distributed field lines, finger-like shaped, with long $L_{\|}$ ($> 50\ m$). These "ergodic fingers" are embedded by the so-called *laminar flux tubes*, composed by field lines with short $L_{\|}$ ($20 \div 30\ m$).

The TEXTOR edge appears to be much more complicated and full of structures, with respect to the RFP edge of Fig. 1.8. This is due to the rather rich spectrum of modes which are generated by the DED (see Fig. 3.8). On the contrary, the RFX feedback system is capable of acting individually on the different n modes, by reducing the sidebands with the CMC [80, 155]. As a result, the RFP edge is dominated by a single 0/1 mode. The measured n_e and T_e distributions clearly exhibits a poloidal and radial modulation of the electron density and temperature fields closely correlated with the calculated magnetic topology as shown in Fig. 1.16. In correspondence of short L_c field lines (laminar flux tubes), a strong local reduction in n_e and T_e with respect to the no-RMP case due to fast parallel particle transport to the wall is measured. In the adjacent regions with longer L_c field lines (ergodic fingers) both n_e and T_e are higher. As a result the laminar zone shows to impose a modulation to the n_e and T_e fields along the poloidal angle [115].

For rotating RMPs this modulation is preserved, but depending on the relative rotation with respect to the plasma, it differs in phase and size from the structures of the calculated magnetic vacuum topology [129]. In case

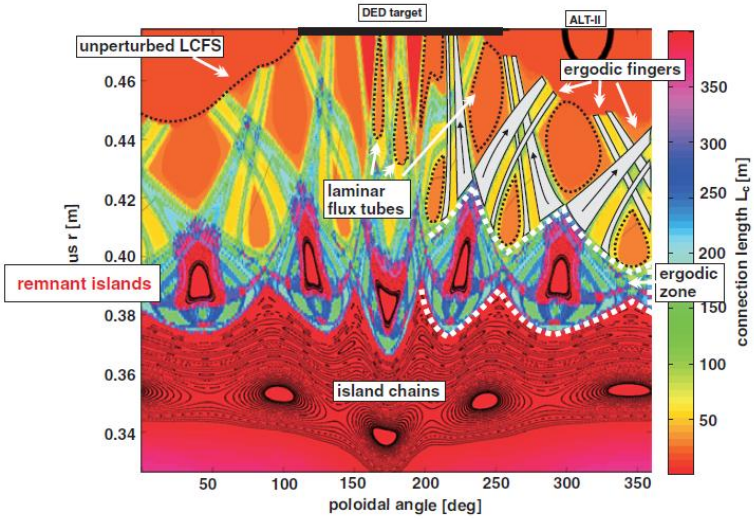

Figure 1.15: An overview of the magnetic topology in the stochastic edge for $m/n = 6/2$ base mode configuration obtained with the GOURDON code. Shown here is a superposition of a Poincaré plot (black colored intersection points with the chosen poloidal plane), a laminar plot (color coded connection length distribution) and highlighted are the characteristic topological domains [115].

of low relative rotation ($\sim -0.2\ kHz$) and high perturbation field strength the modulation is still correlated with the local magnetic vacuum topology [129]: the geometrical properties of the laminar zone follow the same trends as the modeled magnetic vacuum topology. In case of high relative rotation ($\sim 1.8\ kHz$) or low relative rotation level at low RMP field strength, measurements and simulations indicates that the laminar zone is reduced, while in the inner region the remnant island width grows. However, the loss of particles and energy in the laminar flux tubes in terms of the absolute reduction of the plasma parameters remains independent of the relative rotation. Moreover, a shift by $\pi/2$ of the OP and XP of the remnant island is observed in the modulation with respect to the magnetic vacuum topology. These findings suggest the magnetic vacuum topology to be valid for static RMP fields and low toroidal plasma rotation with high perturbation field strength, while, for high relative rotation and low relative rotation level at low perturbation field strength, a new shifted magnetic topology due to screening currents on the rational flux surface occurs [105]. The inductive electric field due to the rotating island can also be important. In fact, we can work out a simplified expression [145] for the inductive contribution as:

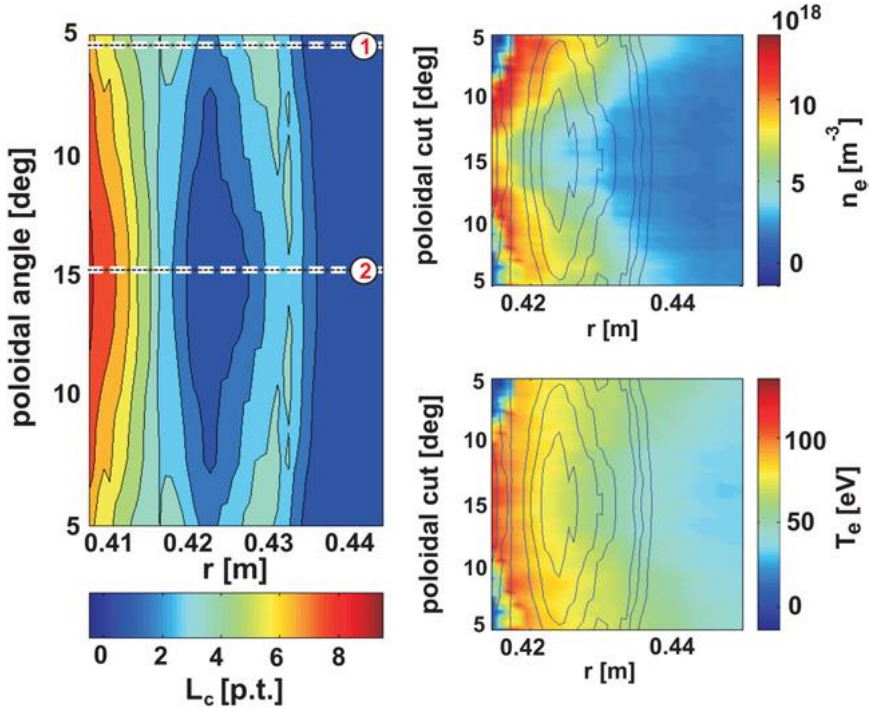

Figure 1.16: Two dimensional n_e and T_e distributions measured with the BES system at LFS performed in $m/n = 12/4$ configuration shifting the magnetic topology in the poloidal direction. The plot on the left shows the corresponding L_c distribution as convolution of ATLAS output with the beam divergence in the poloidal and toroidal directions. Dashed lines mark the extremal points of maximum L_c (1), i.e. ergodic domain and short L_c (2), i.e. laminar flux tube [115].

$$E^r = -\omega r^{m-1} q B_0 \tag{1.3.1}$$

Data typical of Textor, $B_0 = 2\ T$, $r = 0.5\ m$, $q = 4$ and $\omega = 3\ kHz$ give as a result $E^r = -6\ kV/m$, which is not negligible.

Several measurements show the RMP changes the sign of the radial electric field and of the associated plasma flow, which is the topic we are most interested in. In [26] measurements of plasma rotation with the CXRS system are shown. They demonstrate that RMP causes a spin-up in the toroidal and poloidal rotation, in the co-current and ion-diamagnetic drift directions, respectively, with magnitudes depending on the amount of perturbation (see Fig. 1.17). The inferred radial electric field increases, following the spin-up of the rotation, mainly due to the poloidal component. In [153] measurements of plasma potential through the Langmuir probe array show a change of sign of the radial electric field in the ergodic and laminar zones (see Fig. 1.18).

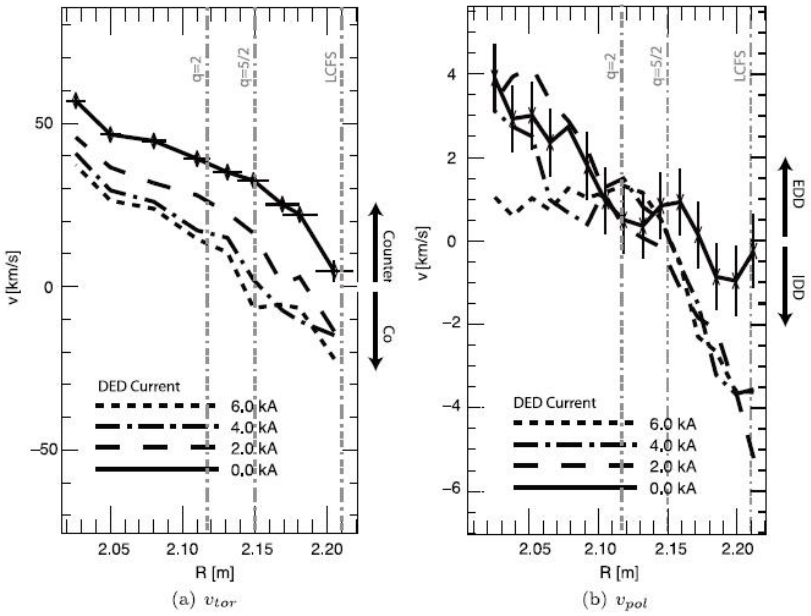

Figure 1.17: Toroidal (a) and poloidal (b) rotation profiles in the plasma edge during a scan of the external perturbation [26]. On the right side of the plots are indicated the co-current and counter-current directions for (a) and the electron drift direction (EDD) and ion-diamagnetic drift (IDD) for (b).

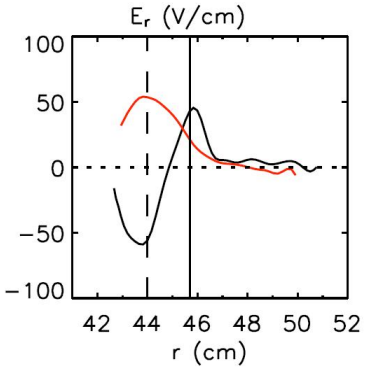

Figure 1.18: Radial profiles of the radial electric field during a $m/n = 6/2$ DED discharge before (black line) and during (red line) the application static RMP, measured by fast reciprocating Langmuir probe arrays. The vertical solid line indicates the limiter position and the vertical dashed line roughly separates the ergodic (left side) and the laminar (right side) zones [153].

1.4 Thesis contents

The main topic of the Thesis is the study of magnetic islands embedded in the chaotic edge of a tokamak, when RMPs are applied, and related electric field E^r and flows. Results are compared with the known phenomenology and theory in the chaotic edge of a RFP, which has been briefly recalled in Sec. 1.2. Proxies of the two configurations are the tokamak TEXTOR, with the application of the DED; and the RFX-mod RFP. The main tool used for simulations of islands, two-fluid transport (electrons and ions), and ambipolar E^r field, is the Hamiltonian guiding-center code ORBIT. This work has been developed by the Student: as such, Chapters 2, 3 and 4 contain original work by the Student.

As an initial step, to validate the reconstruction of the edge topology of TEXTOR and RFX, the ORBIT code has been validated against the volume-preserving code NEMATO (Chapter 2). This work has been done in collaboration with Drs. Susanna Cappello, Daniele Bonfiglio and Marco Veranda, at Consorzio RFX in Padova, and Luis Chacón at Oak Ridge laboratories, USA. In the limit of low energy, ORBIT, can be used to trace the magnetic field topology, in a way in all respects similar to field line-tracing codes. NEMATO is a field-line tracing code, implemented to integrate solenoidal flows for incompressible fluid dynamics, with automatic volume preservation [47]. The question is, how accurate is the description of the magnetic field with ORBIT, given that it is a Hamiltonian code (therefore, with a simplectic matrix), but it uses a Runge-Kutta (RK) integrator instead of a fully implicit solver (which is the case of NEMATO). Besides this, ORBIT describes perturbations in terms of a scalar field α, such that $\delta\vec{B} = \nabla \times \alpha\vec{B}_0$, with B_0 the equilibrium field. The two codes are validated on the structure of the $q = 0$ island chain, which characterizes the MH configuration in RFP. As input for both codes we use the snapshot of a cylindrical 3D nonlinear, MHD visco-resistive simulation (SpeCyl code [20]). The first benchmarking test employs a Hamiltonian (single-mode) magnetic field configuration. Both codes successfully yield field lines which follow flux surfaces in both the $m = 1$ and $m = 0$ cases. The comparison between the codes is extended to a chaotic magnetic field configuration, including many modes. The result is that the scalar field representation of ORBIT and the RK integrator do not include measurable differences in the Poincaré maps and in the calculation of the correlation length of the chaotic field. The work has been presented as a poster at the 2011 APS Division of Plasma Physics meeting in Salt Lake City and published on [24].

As a second step in this Thesis, in order to develop a common picture of particle transport with edge magnetic islands in Tokamaks and RFPs, test particle transport simulations are carried out in TEXTOR following the steps of the study performed in RFX-mod [123] (Chapter 3). The RMP configurations studied are the $m/n = 12/4$ and $3/1$. The ORBIT code has been

adapted to the equilibrium of TEXTOR (circular equilibrium with pressure [144], and a proper form for the eigenfunctions has been developed, on the basis of the analytical formula used in TEXTOR using as input the current flowing in the DED. This work has been done in collaboration with Drs. Oliver Schmitz and Sadrilla Abdullaev at Forschungszentrum Jülich, during two mobility contracts in the periods 18/06/2012-16/07/2012, 07/09/2012-05/10/2012, and 18/02/2013-29/03/2013. The resulting Poincaré plots show basic features of TEXTOR stochastic edge, such as the inner island chain, the remnant islands, and the laminar flux tubes embedded in the ergodic fingers, which is consistent with previous works on this subject, we recalled in Sec. 1.3. Maps in the $(\theta - r)$ plane of the electron and ion parallel connection length to the wall, $L_{\|}(r, \theta)$, highlight the properties of the magnetic structures observed in the Poincaré plot: while ions, having a large Larmor radius, are weakly affected by the magnetic topology, electron trajectories are linked to the magnetic field lines. The behavior of $L_{\|}$ entails a characteristic modulation of the radial electric field E^r with large positive values in the zone with electron $L_{\|} \approx 0$ (the so-called laminar flux tubes, which occupy a region in between the main island chain and the remnant islands). The result on the ion/electron and associated E^r behavior in the TEXTOR stochastic edge, is the main original result of the Thesis, and has been presented as:

- a contributed oral by Giovanni Ciaccio at the Workshop on Stochasticity in Fusion Plasmas (Jülich, May 2013) (it will appear as a paper in a special issue of Nuclear Fusion in 2014);
- a poster at the 40th EPS Conference on Plasma Physics in Espoo, Finland (1-5 July 2013);
- a poster at the Joint 19th ISHW and 16th IEA-RFP workshop (Padova, September 2013);
- an invited talk given by Gianluca Spizzo at the 55th annual meeting of the APS Division of Plasma Physics (Denver, CO, November 2013).

The work on TEXTOR is also an important part of a proposal of funding approved by the EUROfusion consortium for fiscal year 2014, and it will be part of an invited talk which will be given by Nicola Vianello at the 41st EPS Conference in Berlin, in June 2014. Finally, the collaboration with TEXTOR is part of the discussion in the Pedestal & Edge Physics Topical Group (ITPA-PEP) of which Dr. Oliver Schmitz takes part as an expert.

Chapter 4 regards the evaluation of the local radial transport of particles, i.e. ion and electron diffusion coefficients (D_i and D_e, respectively), which is carried on along a helical path from the OP through the XP of an $m/n = 4/1$ remnant island. The result shows that D_i is rather constant along the path, and it is almost neoclassical, while D_e is larger ($4 \div 40\ m^2/s$), and

is strongly modulated (larger at the XP, lower at the OP), consistently with the $L_{\parallel}$ maps. Finally, an analytic 3D formulation of the ambipolar potential for the 3/1 DED configuration is developed on the basis of the geometry of the $m/n = 4/1$ magnetic island, that balances electron and ion fluxes inside the island. The result is compared to measurements of plasma potential inside an $m/n = 4/1$ island in the edge of the TEXTOR device and with the analysis on RFX-mod edge. In RFX-mod ORBIT predicts the potential well to stay in proximity of the OP of the main island ($m/n = 0/1$), while measurements show the potential well near the XP. In the TEXTOR experiment fast Mirnov probe measurements show that the potential well corresponds to the XP of the $m/n = 4/1$ island, i.e. the region with larger D_e, consistently with ORBIT results.
The difference between RFX and TEXTOR could be ascribed to a collisional dependence (the case of RFX is highly collisional, contrary to TEXTOR); to a different level of chaos, in RFX compared to TEXTOR; or to a more pronounced plasma-wall interaction (measured particle fluxes to the wall in the RFP are 2 orders of magnitude larger than in tokamaks, being $\sim 10^{20}\ m^{-2}s^{-1}$ [101]). This shows that the work done in this Thesis has been fundamental to assess the validity of the model developed with ORBIT, and to explain the electrostatic response to a RMP 3D field in a Tokamak.

Chapter 2

Benchmark ORBIT-NEMATO

2.1 Introduction

In this chapter, we will present the code ORBIT and its verification (benchmark) with the NEMATO code in their common application to the mapping of a chaotic magnetic field. ORBIT adopts a Hamiltonian guiding center (GC) drift orbit formalism, allowing for an efficient calculation of particle trajectories in an electromagnetic field. In the limit of low particle energy, it can be used to trace the magnetic field line. In ORBIT, magnetic fields are restricted to the form $\delta\vec{A} = \alpha\vec{B}$. In this way, the perturbed Hamiltonian of field lines assumes the very compact form $H = H_0 + \alpha H_1$. The code controls the conservation of the Hamiltonian (particle energy) asymptotically, by reducing the step size if required. NEMATO solves the magnetic field line equation for any solenoidal field on a grid (in an arbitrary geometry) exactly preserving the solenoidality of the field: this makes the code suitable to study weakly chaotic magnetic fields, typical of the quasi-single helicity RFP [14]. In its present form, the code does not allow as an efficient implementation of particle dynamics as obtained with ORBIT.

Both codes have been used in recent years in experimental and simulation studies of the RFP [37, 79, 124] to study ion and electron transport associated with fluctuations. In the RFX-mod reversed field pinch device [92], it has been demonstrated that, when a single mode dominates the magnetic spectrum of perturbations, there is a transition from chaos (which was long believed the "standard" for this type of configuration [90]) to order (QSH states), with a significant reduction of particle and energy transport [77, 103], as predicted by theory [20]. To understand the change that takes place in transport properties depending on magnetic features, a good reconstruction of magnetic topology is mandatory. In fact, when the fluctuation is magnetic in nature and magnetic chaos is present, particles streaming along the magnetic field line may result in substantial perpendicular transport, and this mechanism can be much more efficient than

perpendicular collisional processes (the parallel diffusivity is $\sim 10^8$ the perpendicular one [17, 31, 122]). This provides strong motivation to control and possibly reduce magnetic perturbations.

The benchmark between the two codes aims at strengthening the validity of their reconstruction of the magnetic topology. In particular, the benchmark allows to verify whether the description of the radial perturbation fields with a vector potential $\delta\vec{A} = \alpha\vec{B}$, used by ORBIT, introduces errors in the magnetic topology reconstruction. Such a verification is a fundamental issue since ORBIT is the main tool used for the transport analysis presented in Chapters 3 - 4. The two codes are used to compare the structure of islands that appear in a reversed-field pinch. As input, we use the snapshot of a 3D nonlinear MHD visco-resistive simulation (SpeCyl code [18]). First, a single-mode configuration is analyzed, since in this case the field lines can be described by a scalar function (which can be considered as a time-independent Hamiltonian with conserved flux surfaces [48]). The two codes successfully yield field lines which follow flux surfaces in both the $m = 1$ and $m = 0$ cases, and flux surfaces given by the two codes do overlap up to numerical error. The comparison between the codes has then been extended to a fully 3D configuration, by including many modes and comparing the Poincaré plots. Finally, the correlation length of field lines in a stochastic bounded domain has been evaluated, in order to produce a quantitative comparison between the two codes. Since NEMATO is primarily used in RFX to distinguish chaotic and ordered domains in space during QSH, while ORBIT is mainly used for transport studies in the chaotic edge and analogies with the resonant magnetic perturbations (RMPs) in tokamaks, this benchmark gives confidence to the results in both areas of research.

The content of the chapter is organized as follows. In Sec. 2.2, we introduce ORBIT: flux coordinate system, Hamiltonian form of GC equations and field lines, perturbation eigenfunctions. In Sec. 2.3, a brief introduction of NEMATO is given. In Sec. 2.4 we describe the SpeCyl simulation used for the benchmark. In Sec. 2.5, we show a qualitative benchmark of ORBIT and NEMATO, with the comparison of the single-mode flux surfaces ($m = 0$ and $m = 1$ cases), and of the Poincaré plots in the chaotic case. In Sec. 2.6, the quantitative benchmark with the evaluation of the correlation length is shown. Finally, we summarized and draw some conclusions in Sec. 2.7.

2.2 ORBIT

ORBIT is a Hamiltonian guiding center code developed by Dr. Roscoe White, and vastly employed in Tokamak community for studies of ion transport (stochastic losses), fast particle-wave interaction and neoclassical effects (for a review of recent results, see Ref [143]). In 2001 ORBIT was adapted to the RFP configuration, in the framework of a collaboration between RFX

and the Plasma Physics laboratories (PPL) in Princeton, NJ (USA). It was used as a Poincaré plotter and for simple estimations of transport, such as the loss time of electrons and ions [50, 96], in RFX and in the University of Wisconsin, Madison, MST reversed-field pinch [34]. The task was facilitated by the fairly precise knowledge of the radial shape of the eigenfunctions in the RFP, where experimental dynamo (kink-tearing) modes are described by the Newcomb's equations in toroidal geometry [157]. ORBIT was then used to analyze the output of the nonlinear, visco-resistive code SpeCyl [18] and helped in describing the topology of $m = 0$ islands providing a transport barrier at the reversal surface $q = 0$ in the edge of the RFP [124]. Using as input the same SpeCyl code, ORBIT was used to evaluate the local ion diffusion coefficient D in the chaotic, MH state, and was a fundamental tool for revealing the nonlocal, subdiffusive nature of chaos in the RFP [125, 126]. The same local evaluation of D was used also in helical case in RFX-mod [57, 58] to characterize the onset of the internal electron transport barrier. Following indications that the QSH state was a "stellarator-like" phenomenon, ORBIT helped in characterizing the trapped particle population within the helical structure [59]. More recently, transport evaluation with ORBIT was extended in determining the size and spatial geometry of the ambipolar electric field in the RFX-mod edge [123]. Other studies with ORBIT of single-particle effects in the RFP include the evaluation of what should be a population of fast ions in a NBI-heated reversed-field pinch, in comparison with the ASDEX Tokamak [60].

2.2.1 Flux coordinates

Toroidal flux coordinates are convenient coordinates to describe a toroidal magnetic configuration: they are defined in order that magnetic field becomes a straight line in those coordinates. Flux coordinates are not unique. ORBIT adopts the so-called "Boozer" coordinates [15]: the poloidal flux ψ_p, labeling the poloidal magnetic surfaces, the generalized poloidal angle, θ, the generalized toroidal angle $\zeta = \varphi - \nu(\psi_p, \theta)$, where φ is the toroidal angle and ν is a periodic function in θ. In the tokamak configuration, the toroidal flux, ψ, could be chosen instead of ψ_p to define the radial flux label. It is worth noting that the choice of ψ_p in ORBIT is fundamental for a RFP configuration, since the ψ function is not monotonic along the radius (see Fig. 2.1(a) - 2.1(b)).

To derive a formulation of the equilibrium and the GC drift motion in toroidal flux coordinates it is necessary to introduce a covariant basis and a contravariant basis for the system. This defines the mapping from flux coordinates to orthonormal euclidean coordinates $\vec{r}(x, y, z)$. The covariant basis is

$$\vec{e}_{\psi_p} = \delta_{\psi_p}\vec{r} \quad \vec{e}_\theta = \delta_\theta \vec{r} \quad \vec{e}_\zeta = \delta_\zeta \vec{r} \tag{2.2.1}$$

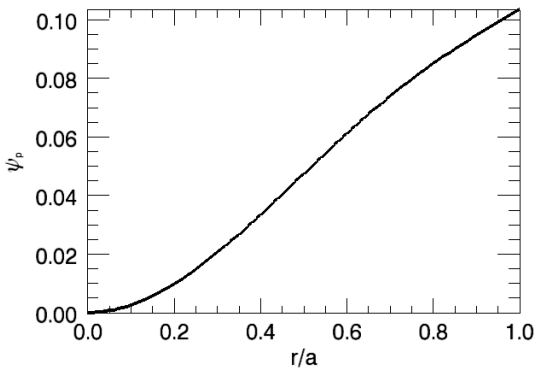

(a)

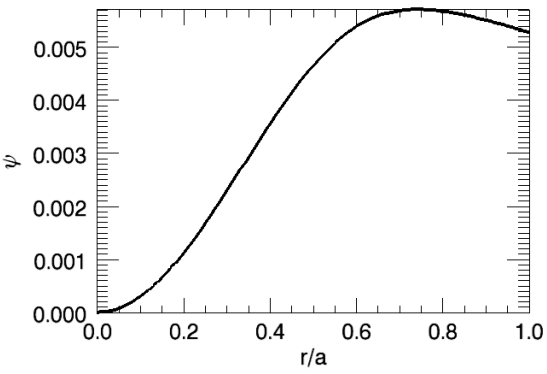

(b)

Figure 2.1: Pololoidal (a) and toroidal (b) fluxes as a function of the normalized minor radius, in an RFP configuration. Since ψ is not monotonic, the choice of ψ_p as radial coordinate is mandatory.

while the contravariant basis is

$$\vec{e}^{\psi_p} = \nabla\psi_p \quad \vec{e}^{\theta} = \nabla\theta \quad \vec{e}^{\zeta} = \nabla\zeta \ , \tag{2.2.2}$$

with Jacobian

$$\mathcal{J} = \vec{e}_{\psi_p} \cdot (\vec{e}_\theta \times \vec{e}_\zeta) = (\vec{e}^{\psi_p} \cdot (\vec{e}^{\theta} \times \vec{e}^{\zeta}))^{-1} \ . \tag{2.2.3}$$

In the "Boozer" coordinates, ζ is chosen to make the field lines straight in the (θ, ζ) plane, while θ is chosen by selecting a particular simple form of $\mathcal{J}$. These two choices result in a unique representation of $\vec{B}$, that can be written in covariant form

$$\vec{B} = g(\psi_p)\nabla\zeta + I(\psi_p)\nabla\theta + \delta\nabla\psi_p \ , \tag{2.2.4}$$

and in contravariant form

$$\vec{B} = \nabla\psi \times \nabla\theta - \nabla\psi_p \times \nabla\zeta \,, \tag{2.2.5}$$

where g and I are the toroidal and poloidal covariant components, respectively. In this coordinate system

$$\frac{\vec{B}\cdot\nabla\zeta}{\vec{B}\cdot\nabla\theta} \equiv q(\psi_p) \,, \tag{2.2.6}$$

meaning that the helicity of the field lines is described by the function $q(\psi_p)$, the so-called safety factor and $\mathcal{J} \propto B^{-2}$. Note that g is a flux function, i.e. it depends only on ψ_p.

2.2.2 Equations of motion

The symplectic formulation of ORBIT's GC equations of motion is a notable achievement by Roscoe White, and can be found in this book (Ref. [146]). Here we rapidly sketch the main features, in order to get the numerical advantages of ORBIT over other guiding center codes.

The GC equations of motion can be obtained starting from the GC Lagrangian, which was derived on the path of Littlejohn (see Ref. [147]).

$$\mathcal{L} = (\psi + \rho_\parallel I)\dot{\theta} + (\rho_\parallel g - \psi_p)\dot{\zeta} + \mu\dot{\xi} - H \tag{2.2.7}$$

where $\rho_\parallel = v_\parallel/B$ is the normalized parallel velocity (namely, with $m_i = 1$, $e = 1$), μ is the magnetic moment, and ξ the gyro-phase. It is immediately shown that Eq. (2.2.7) is equivalent to

$$\mathcal{L} = P_\theta\,\dot{\theta} + P_\zeta\,\dot{\zeta} + \mu\dot{\xi} - H \,, \tag{2.2.8}$$

where the Hamiltonian (i.e. total energy) is given by

$$H = \frac{1}{2}\rho_\parallel^2 B^2 + \mu B + \Phi \,. \tag{2.2.9}$$

The two conjugate momenta are P_θ and P_ζ, given by

$$P_\theta = \psi + \rho_\parallel I \,, \tag{2.2.10}$$

$$P_\zeta = \rho_\parallel g - \psi_p \,. \tag{2.2.11}$$

While P_θ can vary along a particle orbit, P_ζ is conserved if the system has toroidal symmetry. This is the well-known theorem by Emmy Noether. In particular, from the conservation of P_ζ we can obtain

$$\rho_\parallel g - \psi_p = const \,, \tag{2.2.12}$$

which motivates the choice of ψ_p as the radial coordinate of the system. For an orbit that at some point $\psi_{p,0}$ has $\rho_\parallel = 0$, this gives the formula

$$\frac{\Delta\psi_p}{2} = \psi_p - \psi_{p,0} = \rho_\parallel g \tag{2.2.13}$$

that defines the banana width. Moreover, the equations for the momenta (2.2.10) and (2.2.11) show that the couple of variables P_θ, P_ζ depend only on the couple of variables $\rho_\parallel, \psi_p$ (since all of the other terms depend on the "radius" ψ_p only, $g = g(\psi_p)$, $I = I(\psi_p)$ and $\partial\psi/\partial\psi_p = q$ with $q = q(\psi_p)$). This means that, when constructing the equations of motion, one can use the couple P_θ, P_ζ or $\rho_\parallel, \psi_p$ as two equivalent forms.

The Lagrangian formalism is useful in the sense that the equations of motion are given by the Lagrange equations:

$$\frac{\mathrm{d}}{\mathrm{d}t}\frac{\partial\mathcal{L}}{\partial\dot{x}_i} = \frac{\partial\mathcal{L}}{\partial x_i}\,, \tag{2.2.14}$$

with $x_i = \xi, \theta, \zeta$. The Lagrange equations (2.2.14) immediately lead to the GC Hamiltonian equations of motion

$$\begin{aligned} \dot{\theta} &= \frac{\partial H}{\partial P_\theta} \qquad & \dot{P}_\theta &= -\frac{\partial H}{\partial \theta} \\ \dot{\zeta} &= \frac{\partial H}{\partial P_\zeta} \qquad & \dot{P}_\zeta &= -\frac{\partial H}{\partial \zeta}\,, \end{aligned} \tag{2.2.15}$$

The motion along ξ can be ignored since

$$\frac{\mathrm{d}}{\mathrm{d}t}\frac{\partial\mathcal{L}}{\partial\dot{\xi}} = \frac{\mathrm{d}\mu}{\mathrm{d}t} = 0 = \frac{\partial\mathcal{L}}{\partial\xi}\,. \tag{2.2.16}$$

Eq. (2.2.16) is zero at all orders, since μ is a constant of motion: this is the reason for using the guiding center formalism.

If we place the vector of the solutions in the form $(\theta, P_\theta, \zeta, P_\zeta)$, then the Hamilton equations (2.2.15) can be cast in matrix form:

$$\begin{pmatrix} \dot{\theta} \\ \dot{P}_\theta \\ \dot{\zeta} \\ \dot{P}_\zeta \end{pmatrix} = \begin{vmatrix} 0 & 1 & 0 & 0 \\ -1 & 0 & 0 & 0 \\ 0 & 0 & 0 & 1 \\ 0 & 0 & -1 & 0 \end{vmatrix} \cdot \begin{pmatrix} \partial_\theta H \\ \partial_{P_\theta} H \\ \partial_\zeta H \\ \partial_{P_\zeta} H \end{pmatrix} \tag{2.2.17}$$

where the 4×4 matrix is a *symplectic matrix*, $\mathbb{S}$.

Perturbations can be easily inserted in the Lagrangian through a scalar term. Perturbations primarily orthogonal to the original $\vec{B}$, such as tearing and Alfvén perturbations, are described as having the vector potential with gauge $\delta\vec{A} = \alpha\vec{B}$, or $\delta\vec{B} = \nabla \times \alpha\vec{B}$, where α is an arbitrary scalar function which contains information about all the three components (radial,

toroidal, poloidal). The radial component of the perturbed $\delta\vec{B}$ is the one mainly responsible for deforming flux surfaces in presence of tearing modes. Therefore, it is advantageous [58, 96] to match the radial component coming from the curl of $\alpha\vec{B}$, to the experimental measurements or the evaluation coming from the output of an MHD simulation code as we will show in the following paragraphs. The Lagrangian is changed only in the modification of the parallel velocity

$$\rho_\parallel \to \rho_\parallel + \alpha \tag{2.2.18}$$

and Eq. (2.2.7) becomes

$$\mathcal{L} = (\psi + \rho_\parallel I + \alpha I)\dot{\theta} + (\rho_\parallel g + \alpha g - \psi_p)\dot{\zeta} - H \tag{2.2.19}$$

where we dropped the $\dot{\xi}$ term that plays no role.

Choosing the couple (P_θ, P_ζ) as canonical momenta entails that the only explicit coordinates are (θ, ζ), and to get the fields one should obtain them in implicit form from Eqs. (2.2.10) and (2.2.11), which quite complicates the numerical scheme. In fact, if one e.g. wants to evaluate g at ψ_p^*, Eq. (2.2.11) has to be used:

$$P_\zeta = \rho_\parallel g(\psi_p^*) - \psi_p^* \tag{2.2.20}$$

where, for a given P_ζ and $\rho_\parallel$, g has to be evaluated in implicit form from ψ_p^*. In order to maintain an explicit form for the solver, ORBIT equations of motion are build up using $(\rho_\parallel, \psi_p)$ as canonical momenta.

Let's now write out the Lagrange equations for the Boozer coordinates (ψ_p, θ, ζ) and the "velocity" $\rho_\parallel$. The radial coordinate, ψ_p, is made explicit as:

$$\begin{aligned} 0 =& \frac{\mathrm{d}}{\mathrm{d}t}\frac{\partial \mathcal{L}}{\partial \dot{\psi}_p} = \frac{\partial \mathcal{L}}{\partial \psi_p} = \\ =& [\psi' + (\rho_\parallel + \alpha)I' + I\alpha']\dot{\theta} + [(\rho_\parallel + \alpha)g' + g\alpha' - 1]\dot{\zeta} - \partial_{\psi_p} H \\ =& [q + (\rho_\parallel + \alpha)I' + I\alpha']\dot{\theta} + [(\rho_\parallel + \alpha)g' + g\alpha' - 1]\dot{\zeta} - \partial_{\psi_p} H \ . \end{aligned} \tag{2.2.21}$$

Here consider that prime $'$ indicates derivative with respect to ψ_p, there is no explicit dependence on $\dot{\psi}_p$, and $\rho_\parallel$ is function of P_θ, P_ζ only, so $\rho'_\parallel = 0$.

The poloidal angle term is

$$\begin{aligned} &\frac{\mathrm{d}}{\mathrm{d}t}(\psi + \rho_\parallel I + \alpha I) = \\ &= \alpha'_\theta(I\dot{\theta} + g\dot{\zeta}) - \partial_\theta H(\psi' + \rho_\parallel I' + \alpha I' + \alpha' I)\dot{\psi}_p + \\ &\quad + \dot{\rho}_\parallel I + I\dot{\alpha} + \alpha'_\theta I\dot{\theta} + \alpha'_\zeta I\dot{\zeta} = \\ &= \alpha'_\theta(I\dot{\theta} + g\dot{\zeta}) - \partial_\theta H[q + (\rho_\parallel + \alpha)I' + \alpha' I]\dot{\psi}_p + \\ &\quad + I\dot{\rho}_\parallel + (I\alpha'_\zeta - g\alpha'_\theta)\dot{\zeta} = \\ &= -\partial_\theta H \ - I\partial_t \alpha \ . \end{aligned} \tag{2.2.22}$$

The equation for ζ is similar to that for θ,

$$\begin{aligned}
&\frac{\mathrm{d}}{\mathrm{d}t}(\rho_{\|}g + \alpha g - \psi_p) = \\
&= \alpha'_\zeta(I\dot{\theta} + g\dot{\zeta}) - \partial_\zeta H[-1 + (\rho_{\|} + \alpha)g' + g\alpha']\dot{\psi}_p + \\
&\quad + g\dot{\rho}_{\|} + g\dot{\alpha} + \alpha'_\zeta g\dot{\zeta} + \alpha'_\theta g\dot{\theta} = \\
&= \alpha'_\zeta(I\dot{\theta} + g\dot{\zeta}) - \partial_\zeta H[-1 + (\rho_{\|} + \alpha)g' + g\alpha']\dot{\psi}_p + \\
&\quad + g\dot{\rho}_{\|} + (g\alpha'_\theta - I\alpha'_\zeta)\dot{\zeta} = \\
&= -\partial_\zeta H - g\partial_t\alpha \, .
\end{aligned} \tag{2.2.23}$$

Here too, observe the skew-symmetry and the additional term $g\partial_t\alpha$ in the r.h.s. of Eq. (2.2.23).

Finally, the equation for $\rho_{\|}$ is straightforward, since, symmetrically to the equation for ψ_p, we have that $\partial\mathcal{L}/\partial\rho_{\|} = 0$, and therefore

$$\begin{aligned}
\frac{\mathrm{d}}{\mathrm{d}t}\frac{\partial\mathcal{L}}{\partial\dot{\rho}_{\|}} = \frac{\partial\mathcal{L}}{\partial\rho_{\|}} &= 0 \\
I\dot{\theta} + g\dot{\zeta} - \partial_{\rho_{\|}}H &= 0 \, .
\end{aligned} \tag{2.2.24}$$

Eqs. (2.2.21)-(2.2.24) can be cast into matrix form as follows:

$$-[q + (\rho_{\|} + \alpha)I' + I\alpha']\dot{\theta} - [(\rho_{\|} + \alpha)g' + g\alpha' - 1]\dot{\zeta} = -\partial_{\psi_p}H \tag{2.2.25}$$

$$[q + (\rho_{\|} + \alpha)I' + \alpha' I]\dot{\psi}_p + I\dot{\rho}_{\|} + (I\alpha'_\zeta - g\alpha'_\theta)\dot{\zeta} = -\partial_\theta H - I\partial_t\alpha \tag{2.2.26}$$

$$[-1 + (\rho_{\|} + \alpha)g' + g\alpha']\dot{\psi}_p + g\dot{\rho}_{\|} + (g\alpha'_\theta - I\alpha'_\zeta)\dot{\zeta} = -\partial_\zeta H - g\partial_t\alpha \tag{2.2.27}$$

$$-I\dot{\theta} - g\dot{\zeta} = -\partial_{\rho_{\|}}H \, . \tag{2.2.28}$$

Redefine the quantities in parenthesis, which depend on ψ_p and α only, as

$$\begin{aligned}
A &= q + (\rho_{\|} + \alpha)I' + I\alpha' \\
C &= (\rho_{\|} + \alpha)g' + g\alpha' - 1 \\
F &= g\alpha'_\theta - I\alpha'_\zeta = \mathcal{J}B^{\psi_p} \, .
\end{aligned} \tag{2.2.29}$$

In this way, Eqs. (2.2.25) and (2.2.28) can be cast in the condensed form:

$$\begin{vmatrix} 0 & -A & -C & 0 \\ A & 0 & -F & I \\ C & F & 0 & g \\ 0 & -I & -g & 0 \end{vmatrix} \cdot \begin{pmatrix} \dot{\psi}_p \\ \dot{\theta} \\ \dot{\zeta} \\ \dot{\rho}_{\|} \end{pmatrix} = \begin{pmatrix} -\partial_{\psi_p}H \\ -\partial_\theta H - I\partial_t\alpha \\ -\partial_\zeta H - g\partial_t\alpha \\ -\partial_{\rho_{\|}}H \end{pmatrix} \tag{2.2.30}$$

which is of the type $\mathbb{A}\dot{\vec{X}} = Y$. The matrix $\mathbb{A}$ is skew-symmetric (or anti-symmetric), which means, $a_{ij} = -\delta_{ij}a_{ji}$. From the definition, the diagonal contains only zeroes. It can be demonstrated that a 4×4 skew-symmetric

matrix is equivalent to a symplectic matrix $\mathbb{S}$: namely, there exists a non-singular matrix $\mathbb{P}$ so that

$$\mathbb{P}^t \mathbb{A} \mathbb{P} = \mathbb{S} = \begin{vmatrix} 0 & 1 & 0 & 0 \\ -1 & 0 & 0 & 0 \\ 0 & 0 & 0 & 1 \\ 0 & 0 & -1 & 0 \end{vmatrix} \tag{2.2.31}$$

It is a quite general result of classical mechanics (see e.g. Goldstein [61]) that solving a Hamiltonian system is equivalent to inverting a skew-symmetric (or a symplectic) matrix. This is the reason why codes that solve equations in Hamiltonian form are called *symplectic codes*. To be precise, if we use the 4 coordinates $(\psi_p, \theta, \zeta, \rho_\parallel)$ to solve the GC system, the matrix is *only* anti-symmetric $\mathbb{A}$; if on the contrary we use the conjugate variables of the Hamiltonian $(\theta, P_\theta, \zeta, P_\zeta)$ the matrix is in the simplest possible form, i.e. the symplectic $\mathbb{S}$, whose inverse is the transpose, $\mathbb{S}^{-1} = \mathbb{S}^t$ (see Ref. [148] and Eq. (2.2.17) in matrix form). In this case, the matrix $\mathbb{P}$ represents the change of variables from $(\theta, P_\theta, \zeta, P_\zeta)$ to $(\psi_p, \theta, \zeta, \rho_\parallel)$.

If we stick with solving the system in the explicit variables $(\psi_p, \theta, \zeta, \rho_\parallel)$, we end up with the situation where the matrix $\mathbb{P}$ is not orthogonal. In this way, the decomposition (2.2.31) cannot be used to invert the matrix, as it is the case for symmetric matrices. But to calculate the inverse $\mathbb{A}^{-1}$ it is necessary to calculate only $n(n-1)/2$ co-factors, and not the original n^2, since the inverse of a skew-symmetric matrix is skew-symmetric. The determinant of $\mathbb{A}$ is the square of a polynomial in A, g, C, I, which is named the *Pfaffian*

$$D = Ag - CI \tag{2.2.32}$$

D can be expanded in terms of fields and α as follows

$$\begin{aligned} D =& gq + (\rho_\parallel + \alpha) g I' + I g \alpha' + I - (\rho_\parallel + \alpha) I g' - I g \alpha' = \\ =& gq + I + (\rho_\parallel + \alpha)(g I' - I g') \ . \end{aligned} \tag{2.2.33}$$

Using D, in the end it can be shown that

$$\mathbb{A}^{-1} = \frac{1}{Ag - IC} \begin{vmatrix} 0 & g & -I & -F \\ -g & 0 & 0 & C \\ I & 0 & 0 & -A \\ F & -C & A & 0 \end{vmatrix} \tag{2.2.34}$$

The problem with this choice is not the matrix inversion, but the fact that the coefficients A, C, F, g, I depend on the variables (ψ_p, θ, ζ), and this is a source of numerical error in the conservation of energy when advancing the variables in a time step through the Runge Kutta integrator used in ORBIT. On the contrary, using the canonical variables, the matrix is made of $0, 1$, which is machine-precision. In ORBIT, in order to keep the convenient

variables $(\psi_p, \theta, \zeta, \rho_\parallel)$ and fulfill the energy conservation principle, a single particle trajectory is integrated over a time interval adjusted at each time step to minimize the error on the energy conservation. In this way, the energy conservation typically stays within $\Delta E/E \sim 10^{-6}$.

Recently, the stepping equations have been modified, by solving the Lagrangian in terms of P_ζ, ψ_p, θ and ζ. This means that P_ζ is used instead of $\rho_\parallel$ as a primary variable, producing a much more accurate time step. Residual error in the energy, due to the fields in (ψ_p, θ, ζ), is reduced to machine precision by means of a Newton iteration along the orbit. In this way, error in energy can be dropped to $\sim \Delta E/E \sim 10^{-15}$. The new version of the code is called ORBITEP, and has been already applied to simulations of TAE (Toroidal Alfén eigenmodes) in the tokamak [142]. In this thesis we will use the standard distribution of ORBIT, since α is of the order $10^{-2} \div 10^{-3}$, much larger than typical TAE amplitude ($\alpha \sim 10^{-4}$), and the error on the step size depends on α.

2.2.3 Magnetic field lines

In the limit of low energy ORBIT can be used to trace the magnetic field topology. In fact, it can be shown that, in the limit of low kinetic energy of the particle ($\rho_\parallel \to 0$), the GC canonical equations (2.2.15) collapse to the usual Hamiltonian formulation of field lines in Boozer coordinates. Assuming the normalized parallel velocity $\rho_\parallel \sim 0$, i.e. starting the particles with very low energy, the Lagrangian (2.2.19) becomes

$$\mathcal{L} = (\psi + \alpha I)\dot{\theta} + (\alpha g - \psi_p)\dot{\zeta} - H \ . \tag{2.2.35}$$

From the Lagrange equations

$$\frac{\mathrm{d}}{\mathrm{d}t}\frac{\partial \mathcal{L}}{\partial \dot{q}} = \frac{\partial \mathcal{L}}{\partial q} \tag{2.2.36}$$

we can write the equations of motion for the three Boozer coordinates ψ_p, θ, ζ, retaining only the terms in the fields g, I and in α

$$\begin{aligned} -(q + \alpha I' + I\alpha')\dot{\theta} - (\alpha g' + g\alpha' - 1)\dot{\zeta} &= -\,\partial_{\psi_p} H \\ (q + \alpha I' + I\alpha')\dot{\psi_p} + (I\alpha'_\zeta - g\alpha'_\theta)\dot{\zeta} &= -\,\partial_\theta H \\ (\alpha g' + g\alpha' - 1)\dot{\psi_p} + (g\alpha'_\theta - I\alpha'_\zeta)\dot{\theta} &= -\,\partial_\zeta H \ . \end{aligned} \tag{2.2.37}$$

Note that the equation for $\rho_\parallel$ vanishes altogether. The prime $'$ indicates differentiation with respect to ψ_p, and $\alpha'_\zeta = \partial\alpha/\partial\zeta$, $\alpha'_\theta = \partial\alpha/\partial\theta$. The r.h.s. of the three equations (2.2.37), namely, the partial derivatives of H, contain only the ripple $\dfrac{\partial B}{\partial \theta}$, $\dfrac{\partial B}{\partial \zeta}$, the derivatives of the potential Φ, and time

derivatives of α. As long as we do not consider those terms, they all vanish. By dividing the two terms of the first line of Eq. (2.2.37) gives

$$\frac{\mathrm{d}\zeta}{\mathrm{d}\theta} = \frac{\dot{\zeta}}{\dot{\theta}} = \frac{q + \alpha I' + I\alpha'}{1 - \alpha g' - g\alpha'} \approx q + \mathcal{O}(\alpha) \tag{2.2.38}$$

which is the first canonical equation of the field line in Hamiltonian form (2.2.43a), up to order of α, which is typically $10^{-2} \div 10^{-3}$. The second equation can be obtained by dividing the two terms in the third line of Eq. (2.2.37), i.e.

$$\begin{aligned} \frac{\mathrm{d}\psi_p}{\mathrm{d}\theta} = \frac{\dot{\psi}_p}{\dot{\theta}} = \frac{g\alpha'_\theta - I\alpha'_\zeta}{1 - \alpha g' + g\alpha'} = \\ = \frac{(mg + nI)\alpha_{m,n}\cos(m\theta - n\zeta)}{1 - \mathcal{O}(\alpha)} = \mathcal{J}B^{\psi_p} \end{aligned} \tag{2.2.39}$$

which is the second canonical equation of the field line (2.2.45).

Magnetic field lines trajectories can be alternatively derived from the magnetic field contravariant representation (2.2.5). By definition, a field line is in any point tangent to the magnetic field $\vec{B}$:

$$\frac{\vec{B}}{\mathrm{d}\vec{R}} = c\ . \tag{2.2.40}$$

If the magnetic field line is parametrized by arc length s, then

$$\frac{\vec{B}}{B} = \frac{\mathrm{d}\vec{R}}{\mathrm{d}s}\ . \tag{2.2.41}$$

This means also that, using the contravariant components of both $\vec{B}(B^\psi, B^\theta, B^\zeta)$ and $\mathrm{d}\vec{R}(\mathrm{d}\psi, \mathrm{d}\theta, \mathrm{d}\zeta)$ the above equation leads to

$$\begin{aligned} \frac{B}{\mathrm{d}s} = constant = \frac{B^\psi}{\mathrm{d}\psi} = \frac{B^\theta}{\mathrm{d}\theta} = \frac{B^\zeta}{\mathrm{d}\zeta} \\ \frac{\vec{B}\cdot\nabla\psi}{\mathrm{d}\psi} = \frac{\vec{B}\cdot\nabla\theta}{\mathrm{d}\theta} = \frac{\vec{B}\cdot\nabla\zeta}{\mathrm{d}\zeta}\ . \end{aligned} \tag{2.2.42}$$

Using the gradient of ψ given by $\nabla\psi = \partial_{\psi_p}\psi\nabla\psi_p + \partial_\theta\psi\nabla\theta + \partial_\zeta\psi\nabla\zeta$, one gets two equations in Hamiltonian form:

$$\begin{aligned} \frac{\mathrm{d}\zeta}{\mathrm{d}\theta} = \frac{\vec{B}\cdot\nabla\zeta}{\vec{B}\cdot\nabla\theta} = \frac{(\nabla\psi\times\nabla\theta)\cdot\nabla\zeta}{-(\nabla\psi_p\times\nabla\zeta)\cdot\nabla\theta} = \\ = \frac{\partial_{\psi_p}\psi(\nabla\psi_p\times\nabla\theta)\cdot\nabla\zeta}{(\nabla\psi_p\times\nabla\theta)\cdot\nabla\zeta} = \frac{\partial\psi}{\partial\psi_p} \end{aligned} \tag{2.2.43a}$$

$$\begin{aligned} \frac{\mathrm{d}\psi_p}{\mathrm{d}\theta} = \frac{\vec{B}\cdot\nabla\psi_p}{\vec{B}\cdot\nabla\theta} = \frac{(\nabla\psi\times\nabla\theta)\cdot\nabla\psi_p}{-(\nabla\psi_p\times\nabla\zeta)\cdot\nabla\theta} = \\ = \frac{\partial_\zeta\psi(\nabla\zeta\times\nabla\theta)\cdot\nabla\psi_p}{-(\nabla\zeta\times\nabla\theta)\cdot\nabla\psi_p} = -\frac{\partial\psi}{\partial\zeta} \end{aligned} \tag{2.2.43b}$$

with $\psi(\psi_p, \theta, \zeta)$ the Hamiltonian, ψ_p the canonical momentum, ζ the canonical coordinate, and θ plays the role of "time".
The first canonical equation (2.2.43a) gives simply the safety factor q (Eq. (2.2.6)):

$$\frac{\mathrm{d}\zeta}{\mathrm{d}\theta} = q = \frac{\partial\psi}{\partial\psi_p} \,. \tag{2.2.44}$$

The second equation (2.2.43b) is equal to *zero* if the equilibrium $\vec{B}$ is not perturbed. If a perturbation term $\delta\vec{B}$ is added then it becomes:

$$\begin{aligned} \frac{\mathrm{d}\psi_p}{\mathrm{d}\theta} &= \frac{\vec{B}\cdot\nabla\psi_p}{\vec{B}\cdot\nabla\theta} = \frac{(\vec{B}+\delta\vec{B})\cdot\nabla\psi_p}{\vec{B}\cdot\nabla\theta} = \\ &= \mathcal{J}(\delta\vec{B}\cdot\nabla\psi_p) = \mathcal{J}\delta\vec{B}^{\psi_p} = \mathcal{J}(\nabla\times\alpha\vec{B})^{\psi_p} \,. \end{aligned} \tag{2.2.45}$$

The curl can be made explicit by using the covariant representation of $\vec{B}$ (2.2.4)

$$\nabla\times\alpha\vec{B} = \frac{1}{\mathcal{J}} \begin{vmatrix} \vec{e}_{\psi_p} & \vec{e}_\theta & \vec{e}_\zeta \\ \partial_{\psi_p} & \partial_\theta & \partial_\zeta \\ \alpha\delta & \alpha I & \alpha g \,. \end{vmatrix} \tag{2.2.46}$$

Then, expanding in Fourier $\alpha = \sum_{mn}\alpha_{mn}(\psi_p)\sin(m\theta - n\zeta + \phi_{mn})$ Eq. (2.2.45) becomes

$$\begin{aligned} \frac{\mathrm{d}\psi_p}{\mathrm{d}\theta} &= \mathcal{J}(\nabla\times\alpha\vec{B})^{\psi_p} = g\delta_\theta\alpha - I\delta_\zeta\alpha = \\ &= \sum_{m,n}(mg+nI)\alpha_{mn}(\psi_p)\cos(m\theta - n\zeta + \phi_{mn}) = -\frac{\partial\psi}{\partial\zeta} \,. \end{aligned} \tag{2.2.47}$$

Integrating the canonical equations term by term, one obtains:

$$\begin{cases} \frac{\partial\psi}{\partial\zeta} = -\sum_{m,n}(mg+nI)\alpha_{mn}(\psi_p)\cos(m\theta - n\zeta + \phi_{mn}) \\ \frac{\partial\psi}{\partial\psi_p} = q \end{cases} \tag{2.2.48}$$

and summing up the equilibrium and perturbation terms, one gets the toroidal flux:

$$\psi(\psi_p, \theta, \zeta) = \int q\mathrm{d}\psi_p + \sum_{m,n}\frac{mg+nI}{n}\alpha_{mn}(\psi_p)\sin(m\theta - n\zeta + \phi_{mn}) \,. \tag{2.2.49}$$

We emphasize that the choice of the toroidal flux to be the Hamiltonian is mandatory in the RFP due to the reversal of the toroidal magnetic field at the edge. We will use the toroidal flux Hamiltonian in the $m = 0$ case, where Eq. ((2.2.49)) simplifies to

$$\psi(\psi_p, \theta, \zeta) = \int q\mathrm{d}\psi_p + \sum_n I\alpha_{0n}(\psi_p)\sin(-n\zeta + \phi_{0n}) \,. \tag{2.2.50}$$

Eq. (2.2.50) clearly shows the advantage of using the scalar function α to describe perturbations, since with this choice the toroidal flux assumes the form $H = H_0 + \alpha H_1$, which is the standard form of a perturbed Hamiltonian in classical mechanics.
An analogue derivation can be done taking the poloidal flux ψ_p as the Hamiltonian, as it is usage in the tokamak community (see e.g. Eq.(36) in Ref. [15]). In particular, by combining the fluxes as $\psi_h = m\psi_p - n\psi$ one can derive the helical flux function [48, 82]. If we choose (Tokamak choice):

$$\begin{cases} \text{Hamiltonian} = & \psi_p \\ \text{momentum} = & \psi \\ \text{coordinate} = & \theta \\ \text{time} = & \zeta \end{cases} \tag{2.2.51}$$

then the two canonical equations are:

$$\begin{aligned} \frac{\mathrm{d}\psi}{\mathrm{d}\zeta} &= \frac{\vec{B}\cdot\nabla\psi}{\vec{B}\cdot\nabla\zeta} = -\frac{\nabla\psi\cdot(\nabla\psi_p\times\nabla\zeta)}{(\nabla\psi\times\nabla\theta)\cdot\nabla\zeta} = \\ &= -\frac{\partial\psi_p}{\partial\theta}\,\frac{\nabla\psi\cdot(\nabla\theta\times\nabla\zeta)}{(\nabla\psi\times\nabla\theta)\cdot\nabla\zeta} = -\frac{\partial\psi_p}{\partial\theta} \end{aligned} \tag{2.2.52a}$$

$$\begin{aligned} \frac{\mathrm{d}\theta}{\mathrm{d}\zeta} = \frac{1}{q} &= \frac{\vec{B}\cdot\nabla\theta}{\vec{B}\cdot\nabla\zeta} = -\frac{(\nabla\psi_p\times\nabla\zeta)\cdot\nabla\theta}{(\nabla\psi\times\nabla\theta)\cdot\nabla\zeta} = \\ &= -\frac{\partial\psi_p}{\partial\psi}\frac{(\nabla\psi\times\nabla\zeta)\cdot\nabla\theta}{(\nabla\psi\times\nabla\theta)\cdot\nabla\zeta} = \frac{\partial\psi_p}{\partial\psi} \end{aligned} \tag{2.2.52b}$$

where we used $\nabla\psi_p = \partial_\psi\psi_p\nabla\psi + \partial_\theta\psi_p\nabla\theta + \partial_\zeta\psi_p\nabla\zeta$ and $(\nabla\psi\times\nabla\theta)\cdot\nabla\zeta = 1/\mathcal{J}$.
Eq. (2.2.52a) is not trivial: if the flux surfaces do not depend on the ζ the equation is reduced to the identity $0 = 0$, otherwise [1]

$$\frac{\mathrm{d}\psi}{\mathrm{d}\zeta} = \frac{\vec{B}\cdot\nabla\psi}{\vec{B}\cdot\nabla\zeta} = \frac{(\vec{B}+\delta\vec{B})\cdot\nabla\psi}{\vec{B}\cdot\nabla\zeta} = \mathcal{J}(\nabla\times\alpha\vec{B})^\psi \tag{2.2.53}$$

using the ORBIT expression for perturbations, $\delta\vec{B} = \nabla\times\alpha\vec{B}$. We made explicit the curl using the covariant components of $\vec{B} = \delta\nabla\psi + I\nabla\theta + g\nabla\zeta$

$$(\nabla\times\alpha\vec{B})^\psi = \frac{1}{\mathcal{J}}\,\det\begin{vmatrix} \vec{e}_\psi & \vec{e}_\theta & \vec{e}_\zeta \\ \partial_\psi & \partial_\theta & \partial_\zeta \\ \alpha B_\psi & \alpha B_\theta & \alpha B_\zeta \end{vmatrix} = \begin{vmatrix} \vec{e}_\psi & \vec{e}_\theta & \vec{e}_\zeta \\ \partial_\psi & \partial_\theta & \partial_\zeta \\ \alpha\delta & \alpha I & \alpha g \end{vmatrix} . \tag{2.2.54}$$

Thus, Eq. (2.2.53) becomes

$$\frac{\mathrm{d}\psi}{\mathrm{d}\zeta} = \mathcal{J}(\nabla\times\alpha B)^\psi = g\partial_\theta\alpha - I\partial_\zeta\alpha\ . \tag{2.2.55}$$

[1] $\vec{B}\cdot\nabla\zeta = \nabla\psi\times\nabla\theta\cdot\nabla\zeta - \nabla\psi_p\times\nabla\zeta\cdot\nabla\zeta = 1/\mathcal{J}$

If we expand in Fourier series the function α:

$$\alpha = \sum_{m,n} \alpha_{mn}(\psi) \sin(m\theta - n\zeta + \phi_{mn}) \tag{2.2.56}$$

we obtain

$$\frac{\mathrm{d}\psi}{\mathrm{d}\zeta} = \sum_{m,n} (mg + nI)\alpha_{mn}(\psi) \cos(m\theta - n\zeta + \phi_{mn}) = -\frac{\partial \psi_p}{\partial \theta} \tag{2.2.57}$$

Finally Eqs. (2.2.52) are

$$\frac{\partial \psi_p}{\partial \theta} = -\sum_{m,n} (mg + nI)\alpha_{mn}(\psi) \cos(m\theta - n\zeta + \phi_{mn}) \ , \tag{2.2.58a}$$

$$\frac{\partial \psi_p}{\partial \psi} = \frac{1}{q} \ , \tag{2.2.58b}$$

which can be separately integrated, getting:

$$\psi_p(\psi, \theta, \zeta) = \int \frac{\mathrm{d}\psi}{q} - \sum_{m,n} \frac{mg + nI}{m} \alpha_{mn}(\psi) \sin(m\theta - n\zeta + \phi_{mn}) \ . \tag{2.2.59}$$

combining the fluxes as $\psi_h = m\psi_p - n\psi$ one can derive the helical flux function:

$$\psi_h = m\psi_p - n\psi - \sum_{m,n} (mg + nI)\alpha_{mn}(\psi) \sin(m\theta - n\zeta + \phi_{mn}) \ . \tag{2.2.60}$$

We will use the helical flux formula (2.2.60) when dealing with single $m \neq 0$ modes.

2.2.4 Magnetic field perturbation components

The radial component of the curl of $\alpha\vec{B}$ is determined by matching it with experimental measurements or with the output of a MHD code (such as SpeCyl), as already mentioned above. Let us consider the case of SpeCyl, where the constraint is the radial perturbation b^r (defined in cylindrical coordinates) given as output of a test run, which will be described later, in Sec. 2.4. The radial component of $\alpha\vec{B}$, in cylindrical coordinates, b^r_{orb}, is

$$b^r \equiv b^r_{orb} = (\nabla \times \alpha\vec{B})^r = \left(\frac{1}{r} \frac{\partial(\alpha g)}{\partial \theta} - \frac{\partial(\alpha I)}{\partial \zeta} \right) . \tag{2.2.61}$$

It is worth mentioning that, if one calculates the curl in Boozer coordinates [58], then the result corresponds to a different gauge and a different α. A rapid check shows that this does not affect significantly the output

Poincaré plot. Inserting the Fourier expression for α, it is possible to get from (2.2.61) the relationship between α and the radial perturbation b^r:

$$\alpha_{m,n}(r) = \frac{b^r}{mg/r + nI} \,. \tag{2.2.62}$$

Fixing the radial component of $\nabla \times \alpha\vec{B}$ by satisfying the condition $b^r \equiv b^r_{orb}$ automatically fixes also the other two longitudinal components b^θ_{orb} and b^ζ_{orb}, given by the curl of α along the poloidal and toroidal directions. Those components are also present in SpeCyl outputs, and do not necessarily coincide with b^θ_{orb} and b^ζ_{orb} (SpeCyl does not satisfy $b^r = (\nabla \times \alpha\vec{B})^r$). Therefore, there is a potential mismatch between the θ and ζ components in ORBIT and SpeCyl which can be summarized as follows:

$$\begin{aligned} b^\theta \neq b^\theta_{orb} &= (\nabla \times \alpha\vec{B})^\theta = \left(\frac{\partial(\alpha B_r)}{\partial\zeta} - \frac{\partial(\alpha g)}{\partial r}\right) = -\frac{\partial(\alpha g)}{\partial r} \\ b^\zeta \neq b^\zeta_{orb} &= (\nabla \times \alpha\vec{B})^\zeta = \frac{1}{r}\left(\frac{\partial(r\alpha I)}{\partial r} - \frac{\partial(\alpha B_r)}{\partial\theta}\right) = \frac{1}{r}\frac{\partial(r\alpha I)}{\partial r} \end{aligned} \tag{2.2.63}$$

This is shown in Figs. 2.2 and 2.3 for two sample $m = 0$ and $m = 1$ modes. The ORBIT radial component matches the radial perturbation of the SpeCyl run by construction. As expected, the α-profile is very similar to the radial perturbation. However, the profiles of the longitudinal component of $(\nabla \times \alpha\vec{B})$ clearly differ from the SpeCyl perturbations, with the exception of the toroidal component for the $m = 0$ case (Fig. 2.2(d)), whose longitudinal component is mainly poloidal. The fact that NEMATO accepts the full 3D spectrum of perturbations without any assumption (see Sec. 2.3) gives the unique opportunity to verify if the gauge of the vector potential adopted by ORBIT produces significant differences in the outputs.

2.3 NEMATO

NEMATO is a volume-preserving integrator for any solenoidal fields on a 3D grid (for arbitrary geometries). It solves the magnetic field line equation $\mathrm{d}\vec{x}/\mathrm{d}\tau = \vec{B}(\vec{x})$ where $\vec{B}$ is the magnetic field given on the 3D grid $\vec{x}$, and the "time" τ represents a coordinate along the field line. The two main features of the code are the interpolation method over the grid and the volume-preserving integration scheme: both of these features aim at ensuring the respect of the solenoidality of the magnetic field in all the computational processes, exactly preserving $\nabla \cdot \vec{B} = 0$ to numerical round-off along each magnetic field line everywhere in the domain. As a result, integrable and chaotic field lines are well distinguished one from the other [47].

Magnetic field lines are curves in the three dimensional space that are always tangential to the magnetic field vector $\vec{B}$. NEMATO does not use

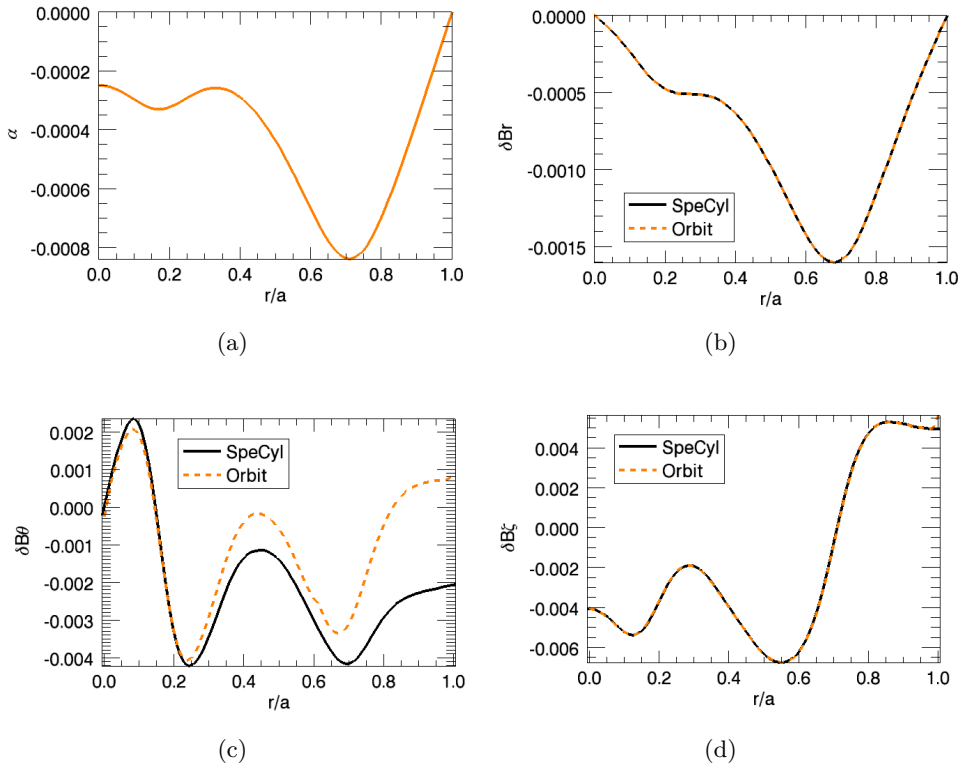

Figure 2.2: α-profile and comparison of SpeCyl and ORBIT perturbation component for an $m = 0$ $n = 4$ mode. The ORBIT radial component matches the radial perturbation of the SpeCyl run by construction (b). As expected, the α-profile is very similar to the radial perturbation (a). The ORBIT toroidal component (d) does not show a big difference from SpeCyl perturbation, on the contrary of (c) the poloidal one which is the only longitudinal component for an $m = 0$ mode. The α has dimension m, here it is normalized to the major radius. Magnetic perturbations are normalized to the field on axis.

the Hamiltonian for field lines, but solves directly the magnetic field line equation, given by:

$$\frac{d\vec{x}}{d\tau} = \vec{B}(\vec{x}). \tag{2.3.1}$$

Eq. (2.3.1) is a system of ordinary autonomous differential equations. The study of a system of ordinary autonomous differential equation of the type:

$$\frac{dx}{dt} = F(x), \qquad x \in \mathbb{R}^n, \qquad F \in \mathbb{R}^n\ , \tag{2.3.2}$$

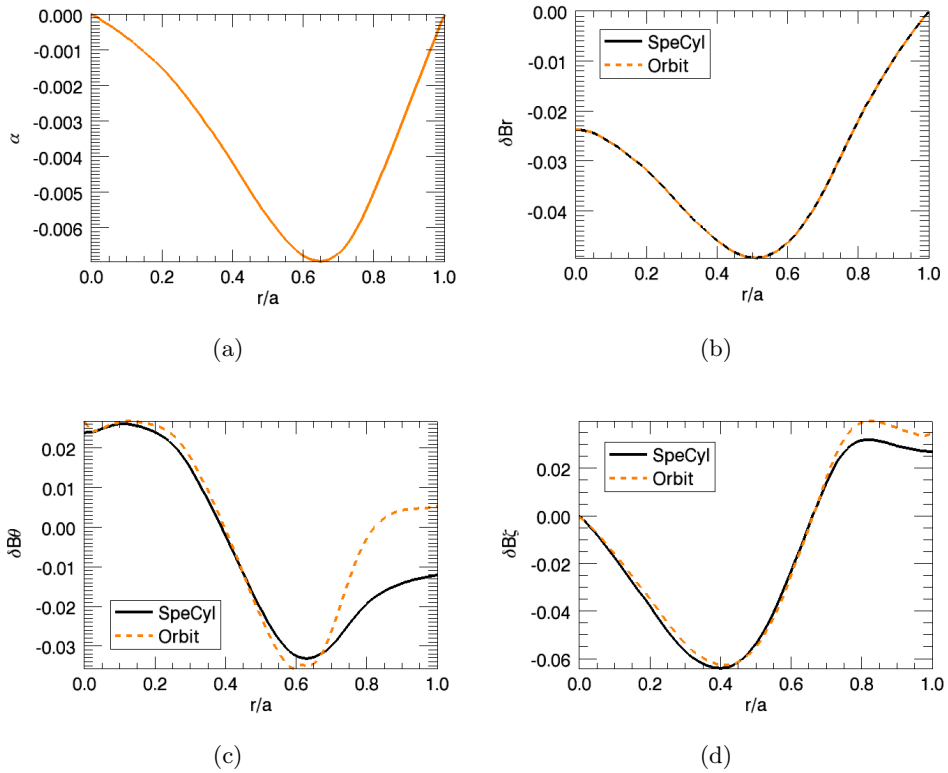

Figure 2.3: α-profile and comparison of SpeCyl and ORBIT perturbation component for an $m = 1$ $n = 11$ mode. The ORBIT radial component matches the radial perturbation of the SpeCyl run by construction (b). As expected, the α-profile is very similar to the radial perturbation (a). However, the profiles of the longitudinal component of $(\nabla \times \alpha \vec{B})$ clearly differ from the SpeCyl perturbations (c-d). The α has dimension m, here it is normalized to the major radius. Magnetic perturbations are normalized to the field on axis.

makes use of some tools from the study of dynamical systems. An important quantity is the map $\Phi^t(x)$ of the vector field $F(x)$, defined as the value at the time t of the solution of (2.3.2) that has x as starting condition. The quantity $\{\Phi^t(x), x \in \mathbb{R}^n\}$ is called *flow map* of the vector field $F(x)$.
Consider a closed surface S_0 in the n-dimensional space. Under the action of the vector field $F(x)$ the evolution of the points inside the volume enclosed by S_0 has some interesting properties, that depend on the vector field features. The following theorem shows how the volume of a set of initial conditions A varies under the action of the vector field $F(x)$.
Theorem: volume of the solutions [62] Let $A \subset \mathbb{R}^n$ be a measurable

set. Then the volume $\mathrm{Vol}(\Phi^t(A))$ varies in time according to:

$$\frac{d}{dt}\mathrm{Vol}\big(\Phi^t(A)\big) = \int_{\Phi^t(A)} \nabla \cdot F(x) dV. \tag{2.3.3}$$

For a solenoidal field (like $\vec{B}$) the volume of the solutions cannot vary in time. There is, thus, a parallelism between the properties of a magnetic field and the ones of an Hamiltonian system (whose divergence is equal to zero too). Both Eq. (2.3.1) and Eqs. (2.2.43a)-(2.2.43b) need to fulfill the constraint of conservation of the volume of the solutions. The numerical integration of the magnetic field line equation thus requires volume preserving integrators.

To integrate Eq. (2.3.1) when the magnetic field $\vec{B}(\vec{x})$ is known on a grid, a numerical scheme has to fulfill two main conditions. The first is that the integrator must conserve the volume of the solution. NEMATO uses a composition of two Crank-Nicolson time steps, each one being exactly volume preserving in a two dimensional space [47]. It is worth underlining that $\vec{B}(\vec{x})$ can be a generic, solenoidal 3D field. The approach is volume-preserving in 3D also.
The second is that the process to obtain the value of the field $\vec{B}(\vec{x})$ in points out of the grid must preserve its solenoidality. To fulfill this requirement two steps are performed: first the vector potential $\vec{A}$ is calculated on the grid, then it is interpolated using high order spline interpolation, finally the magnetic field is *analytically* calculated taking the curl of $\vec{A}$ in every desired point of the domain.

2.4 Test run

The run used for the benchmark is a SpeCyl OPCD (Oscillating Poloidal Current Drive) simulation (pinch parameter $\Theta = B_\theta(a)/\langle B_\phi \rangle = 1.6$, Lundquist number $S = 3 \times 10^4$, Prandtl number $P = 500$), shown in Fig. 2.4. SpeCyl calculates the nonlinear evolution of 25 n-modes for the $m = 0$ and 55 n-modes for the $m = 1$; the dynamical evolution of 145 different MHD modes with $m = 2, 3, 4$ has also been calculated but is not used in this benchmark. The OPCD process drives a (poloidal) current into the plasma by a controlled oscillation of the safety factor at the wall, $q(a)$. Empirical observations show that this poloidal current, and associated electric field E_θ, interact with the dynamo process that sustains the RFP configuration, and result in increased temperature and confinement time [134]. The concept of an inductive application of a poloidal electric field to a reversed-field pinch was pioneered in the University of Wisconsin, Madison, MST device, as a means of reducing the need for a turbulent dynamo and a cheap alternative to the radio-frequency heating and beam injection [110]. A drawback is the intrinsic, pulsed nature of the process, which is difficult to extrapolate to a real fusion reactor [100].

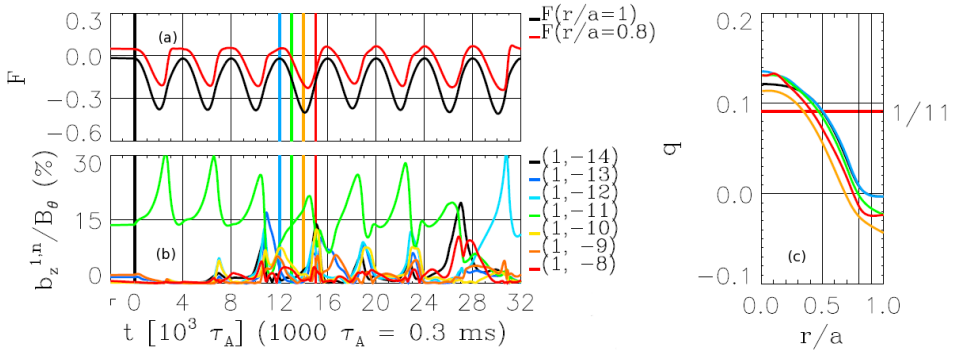

Figure 2.4: OPCD SpeCyl run. Time evolution of (a) q_a, (b) the radial magnetic field perturbation $m = 1$ component, (c) of the whole safety factor profile. The time instant (13500 τ_A) is chosen at half-drop of q_a, i.e. when the dominant $m = 1$ $n = 11$ mode is maximum (green vertical line).

In Fig. 2.4(a), the time evolution of the reversal parameter $F = B_\phi(a)/\langle B_\phi \rangle$ is shown. In panel (c), the temporal evolution of the whole safety factor profile is shown. SpeCyl simulations show that the OPCD induces a controlled and periodic increase of the dominant kink-tearing mode ($m = 1$ $n = 11$ in SpeCyl spectrum), as shown in Fig. 2.4(b), and this is confirmed by the experiment [27]. In the experiment there is also a clear statistical correlation between high temperatures, obtained in the OPCD, and high amplitude of the dominant mode [27]. As such, OPCD is a promising way of obtaining a pulsed, quasi-stationary helical state (QSH), which can be an alternative to obtaining a long-lasting QSH state at high currents [103].

To select the snapshot for the benchmark, we decided to choose a time instant (13500 τ_A, where τ_A is the Alfvén time) at half-drop of q_a, i.e. when the dominant $m = 1$, $n = 11$ mode is maximum (see Fig. 2.4(b)). This time instant corresponds in experiment to the maximum temperature (as explained above), and also to the maximum applied poloidal electric field, since E_θ is proportional to the time derivative of $B_\phi(a)$ during the current drive [27]. Maximun E_θ corresponds also to the maximum co-dynamo phase of the OPCD process [6]

The spectrum for the snapshot at 13500 τ_A ($m = 0$ and $m = 1$ modes) is shown in Fig. 2.5(a), along with the q profile (panel (b)). The radial profiles of the kink-tearing modes, B^r components, are shown in Fig. 2.5(c) for the $m = 0$, and in Fig. 2.5(d) for the $m = 1$. The dominant $m = 0$ mode is the $n = 4$, while the dominant $m = 1$ is the $n = 11$, as already mentioned. The $m = 0$ eigenfunction is peaked at the *reversal surface*, i.e., the radius where $q = 0$, while the $m = 1$ mode has a broad peak more or less at mid-radius. This is a striking difference between the usual tearing

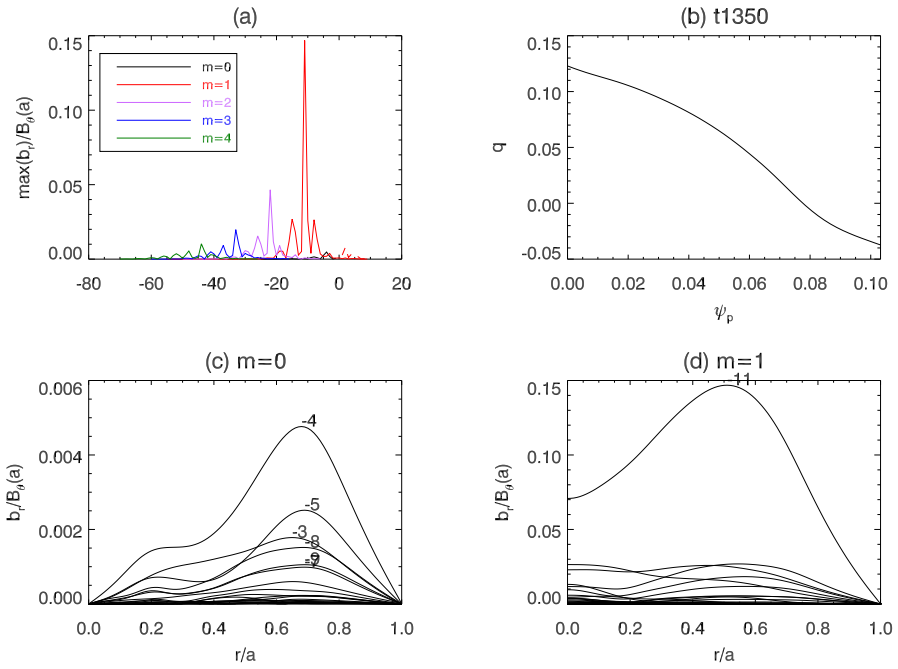

Figure 2.5: (a) Spectrum for the snapshot at 13500 τ_A; (b) q profile; radial profiles of the kink-tearing modes (c) for the $m = 0$, and (d) for the $m = 1$.

modes in the Tokamak (small and very localized in radius), and the $m = 1$ tearing modes in the RFP (broad and with a kink-like behavior; thus the definition of *kink-tearing* modes [20]). Since the $m = 1$ eigenfunction is broad in the RFP, when two modes interact, the destruction of conserved flux surfaces cannot be described by ad-hoc quasi-linear methods, such as those common in the Tokamak community (at least before the introduction of the resonant magnetic perturbations in those devices, see e.g. Ref [106]). Thus the necessity of advanced codes, such as ORBIT and NEMATO.

2.5 Qualitative benchmark

In this section, a qualitative benchmark of the codes will be presented. First, we will show the comparison of the conserved flux surfaces for two different symmetries. In the first case, a single $m = 0$, $n \neq 0$ MHD mode is added to the SpeCyl equilibrium field. In the second case, a $m = 1$, $n = 11$ mode is considered. In a final stage, the Poincaré plots (created by NEMATO and ORBIT) for the chaotic case, where more than one MHD mode is considered, will be compared.

2.5.1 Conserved flux surfaces

As a preliminary test, we will demonstrate that the Poincaré plot made by ORBIT matches the analytical curves of a single $m = 0$ or $m = 1$ mode. Flux surfaces are calculated analytically according to Eqs. (2.2.50) and (2.2.60), respectively. Fig. 2.6 shows the comparison for the $m = 1$, $n = 11$ case. An analogue benchmark has been published for NEMATO [14]. We conclude that comparing the analytical flux surfaces is the same as comparing the Poincaré for a single mode.

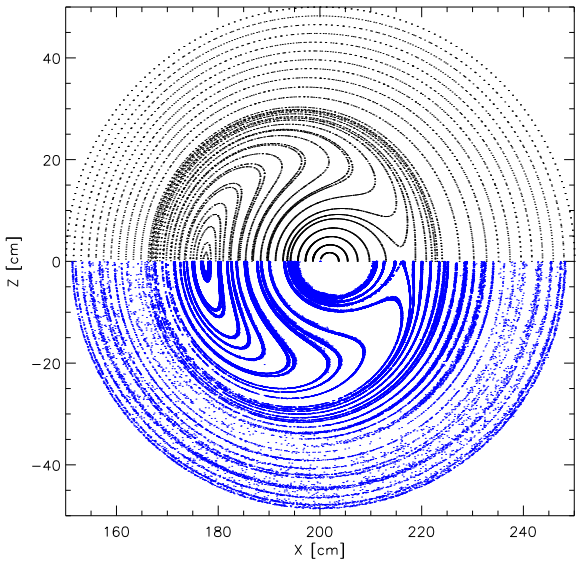

Figure 2.6: Analytic flux surfaces (black) match ORBIT Poincaré plot (blue) for an $m = 1$ $n = 11$ mode.

In Fig. 2.7, a comparison of the flux surface contours for the $m = 0$ case, $n = 1$ and $n = 1 - 25$, for ORBIT and NEMATO, respectively, is shown. In Fig. 2.8, the same is done for the $m = 1$, $n = 11$ mode. The ORBIT and NEMATO curves match each other exactly. As a more quantitative estimate, we can calculate the values of the island widths in the linear approximation (i.e., by expanding q around the unperturbed flux surface ψ_0 at the resonance, see Ref. [146]):

- $m = 0$ $n = 1$:

$$\Delta\psi_p = 4\left|\frac{\alpha_{0,1} I}{q'}\right|^{1/2} \Rightarrow \begin{cases} \Delta\psi_{p,O} = 5.214\ 10^{-3} & \text{i. w. ORBIT} \\ \Delta\psi_{p,N} = 5.215\ 10^{-3} & \text{i. w. NEMATO} \end{cases}$$

- $m = 1$ $n = 11$:

$$\Delta\psi = 4\left|\frac{\alpha_{1,11}(mg + nI)q(\psi_0)^2}{q'}\right|^{1/2} \Rightarrow \begin{cases} \Delta\psi_O = 6.1\ 10^{-3} & \text{i. w. ORBIT} \\ \Delta\psi_N = 6.2\ 10^{-3} & \text{i. w. NEMATO} \end{cases}$$

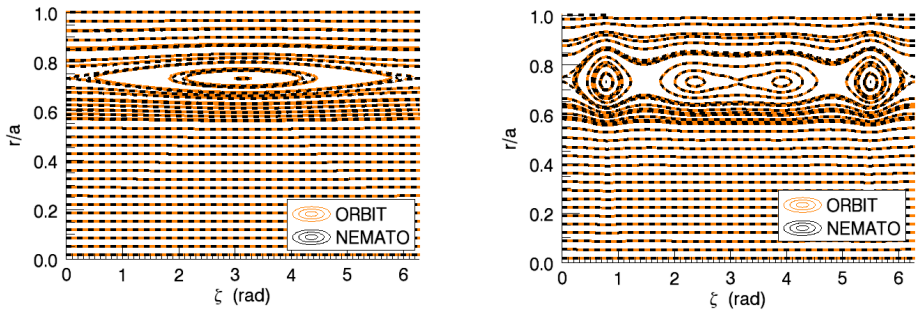

(a) (b)

Figure 2.7: Conserved flux surfaces contours for the (a) $m = 0$ $n = 1$ and (b) $m = 0$ $n = all$ modes. ORBIT (red) and NEMATO (black) curves match each other exactly.

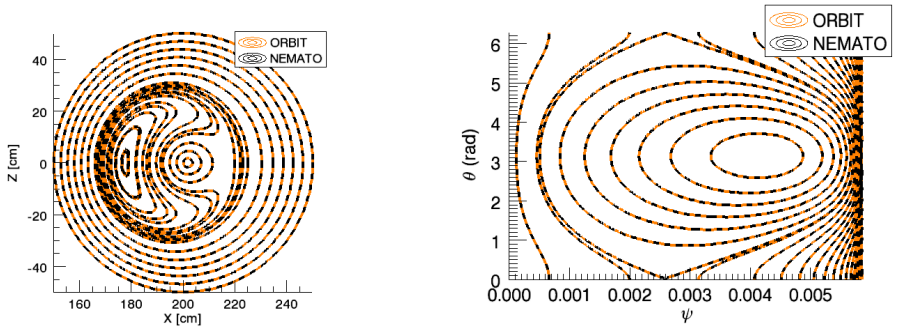

(a) (b)

Figure 2.8: Conserved flux surfaces for the $m = 1$ $n = 11$ mode in (a) poloidal section and (b) helical section. ORBIT (red) and NEMATO (black) curves match each other exactly.

2.5.2 Poincaré plots, chaotic case

The benchmark is now extended to the full spectrum of $m = 0$ and $m = 1$ modes, by comparing the Poincaré plots directly. In this case, we

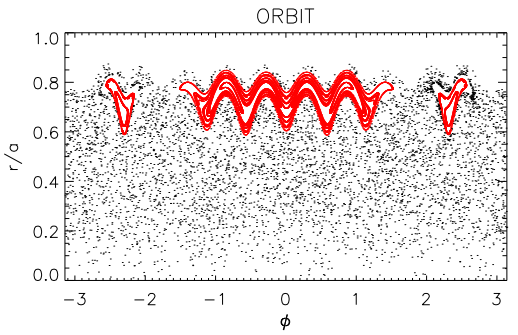

(a)

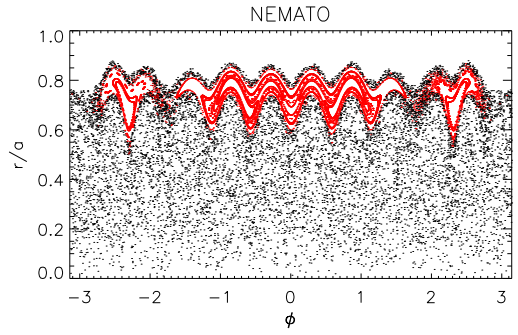

(b)

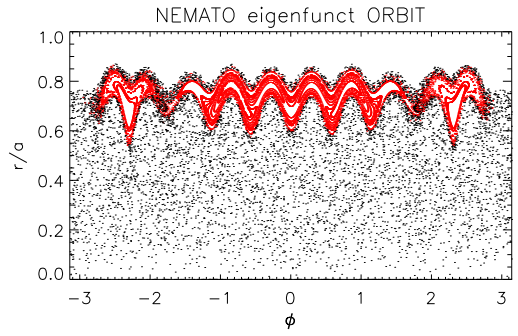

(c)

Figure 2.9: Poincaré plots generated with 52 field lines with the same initial conditions (=the reversal radius), and following them for a length equivalent to 150 toroidal turns. Poincaré with ORBIT (a), and two different plots with NEMATO: one with the α-profiles (c), and the other with the original SpeCyl perturbations (b). The three plots have conserved structures (red points) with similar shape and dimension, differing just in small details.

cannot make use of the analytical formulas (2.2.50) and (2.2.60), since the non-linear interaction between different n's in the $m = 1$ spectrum causes chaos to develop in most of the spatial domain.
The plots have been generated with 52 field lines with the same initial conditions (at reversal radius, $\theta = 0$, equally spaced in ϕ), and following them for a length equivalent to 150 toroidal turns. In Fig. 2.9, we show the Poincaré with ORBIT (panel (a)) and NEMATO (panel (b)). The two plots have conserved structures with similar shape and dimension, differing just in small details, that is, small secondary islands near the major conserved structures (at $r/a = 0.8$ and $\phi \sim -\pi/2$), present in NEMATO and not in ORBIT.

These small differences *can not* be ascribed to the α vector potential description of the perturbations adopted by ORBIT, that entails an approximation of the toroidal and poloidal perturbation components, in contrast with NEMATO, that uses the exact SpeCyl perturbation components. This can be shown running NEMATO with the same approximated toroidal and poloidal perturbations of ORBIT. In other words we made use of the exact SpeCyl radial perturbation b^r, and of the spurious toroidal and poloidal components given by ORBIT, b^θ_{orb} and b^ζ_{orb} of Eq. (2.2.63). The corresponding Poincaré plot (Fig. 2.9, panel (c)) shows the same small structures present in the plot obtained running NEMATO with the original SpeCyl perturbations (panel (b)). This proves that the α vector potential description of the perturbations does not modify the magnetic topology, in spite of quite different longitudinal components (see Figs. 2.2 and 2.2). This result was somewhat expected, since the radial component is the one solely responsible for perturbations of the flux surfaces given by a tearing mode.

We conclude that the small differences between ORBIT (panel (a)) and NEMATO (panel (b)) Poincaré plots are due the different numerical schemes (volume-preserving in NEMATO, step-size adapting in ORBIT). However, the small structures present in NEMATO have a typical size $\Delta r \approx 1$ cm, comparable to the ion Larmor radius in the RFX device at plasma current $I_p = 1.2$ MA (the electron Larmor radius is of the order of few mm). This means that the details seen in the Poincaré plots are of minor importance in the dynamics of electrons and ions, and generally speaking on transport. But if one is interested in the description of very detailed topological structures, such as cantori and transport barriers associated to shearless regions [32], NEMATO is more apt than ORBIT. This can be the case of the dynamical transition between chaos and order which takes place in the RFP.

2.6 Quantitative benchmark

In order to produce a quantitative estimate of the agreement between the two codes, we studied two basic metrics of the properties of chaos: the Lyapunov exponent [158] and the diffusion rate of the magnetic field lines

through the direct evaluation of magnetic diffusivity [28].

2.6.1 Lyapunov exponent

The Lyapunov exponent characterizes the exponential growth of the separation δ between two initially close ($\delta_0 \ll \delta$) trajectories (=field lines)

$$\delta(L) = \delta_0 e^{\lambda L} \tag{2.6.1}$$

where L is the length along the field lines. As pointed out by Zaslavsky [158], the definition (2.6.1) is correct in the limits $\delta_0 \to 0$ and $L \to \infty$. While getting the limit $\delta_0 \to 0$ is relatively easy with stepping codes (you define an array of exponentially separated δ), to get the limit $L \to \infty$ is obviously impossible in finite domains. For this reason, a Finite Size Lyapunov Exponent (FSLE) can be defined [7], by analyzing the average exponential divergence of an ensemble of pairs of field lines, initially separated by δ_0, over a grid of thresholds $\delta_n = r^n \delta_0$, $n = 1, \ldots, N$. The maximum δ_N is approximately the system size. By measuring the parallel length $L(\delta_n, \delta_{n+1})$ to get from one point in the grid to the next ("doubling time", or "doubling length"), from Eq. (2.6.1) the (finite) Lyapunov exponent is found as

$$\lambda(\delta_n) = \left\langle \frac{\log r}{L(\delta_n, \delta_{n+1})} \right\rangle , \tag{2.6.2}$$

where the average $\langle \ldots \rangle$ is performed over many pairs of field lines. The FSLE is defined as the limit $\delta \to 0$ of expression (2.6.2), or

$$\lambda = \lim_{\delta \to 0} \lambda(\delta) = \lim_{\delta \to 0} \left\langle \frac{\log r}{L(\delta_0, \delta)} \right\rangle . \tag{2.6.3}$$

It is worth noting that the Lyapunov exponent is a diagnostic of a very local property the field [133].
By calculating the FSLE with the two codes for a run with 3500 pairs of field lines started at $\psi_p = 0.05$ ($r \approx 33$ cm), we get $\lambda \approx 6.5\ 10^{-4}$ cm^{-1} for ORBIT and $\lambda \approx 19.\ 10^{-4}$ cm^{-1} for NEMATO. In terms of Kolmogorov lengths $L_k = 1/\lambda$, the values are 15.1 m and 5.4 m, respectively.

2.6.2 Correlation length

A second metric of the stochastic properties of the RFP is the magnetic diffusivity of field lines [28]. Again, because of the finite size of the stochastic domain, a diffusive regime can be identified only locally for lengths of the order of the so-called *correlation length* L_{corr} of the magnetic field.

In fact, let us start from the definition of the stochastic diffusion coefficient D_{st} in an unlimited stochastic domain [104]:

$$D_{st} = \lim_{L \to \infty} F(r_0, L) = \int_0^\infty \mathrm{d}L C(L) \tag{2.6.4}$$

with $C(L)$ the auto-correlation function and F the correlation function of field lines:

$$F(r_0, L) = \int_0^L \mathrm{d}L^{'} C(L^{'}) \equiv \frac{1}{2} \frac{\mathrm{d}\langle (r - r_0)^2 \rangle}{\mathrm{d}L} \tag{2.6.5}$$

Here the quadratic mean square displacement $\langle (r - r_0)^2 \rangle$ has been introduced, which corresponds to a random walk of the field lines on a plane perpendicular to the path L along the field line. The average has to be intended as a spatial average over many iterates on the same plane, which defines the Poincaré plot.

The definition of D_{st} fails in a bounded domain where $\lim_{L \to \infty} F(r_0, L) = 0$. This is shown in Fig. 2.10. The function F takes its maximum value close to $L = 0$, vanishes for $L = L_w$ and then oscillates around zero, without reaching a diffusion regime. The length L_w is the parallel length a field line traverses to reach the boundary of the chaotic domain (which is the area of the conserved $m = 0$ islands at the reversal, evident in Fig. 2.9), and then being bounced back to the center. In this process, the auto-correlation function $C(L)$ experiences a large domain of negative values, where the field trajectories are anti-correlated to one other. This means that the probability of a radial jump having an opposite sign with respect to the preceding one is larger than that of retaining the same sign. This is the definition of a *subdiffusive regime* [109]. This behavior has also been found in analysis of tracer flows on outputs of gyrokinetic simulations (see Figure 2(b) in Ref. [84]).
When the system is subdiffusive one can rely on an approximate definition of the quadratic mean square displacement, as follows [28]

$$\langle (r - r_0)^2 \rangle \approx 2 \int_0^{L_w} \mathrm{d}L^{'} F(r, L^{'}) = 2F(L_*)L_w \tag{2.6.6}$$

where $L_* \in [0, L_w]$. A reasonable definition for the diffusion coefficient is

$$D_{st} = \frac{\langle (r - r_0)^2 \rangle}{2L_w} = \frac{2F(L_*)L_w}{2L_w} = F(L_*) \tag{2.6.7}$$

where L_w is determined by the first zero of F and $L_* = L_{corr}$ by definition. A confirmation of the subdiffusive nature of chaos is shown in Fig. 2.10(a): after a ballistic regime with $\langle (r - r_0)^2 \rangle \sim L^{1.8}$ and $C \approx 1$, field lines reach subdiffusion with $\langle (r - r_0)^2 \rangle \sim L^{0.3}$. It is interesting to notice that the access to the subdiffusive regime corresponds to the large negative minimum of $C(L)$, at $L \sim 0.1$ toroidal turns, namely at $L \simeq L_{corr}$. The subdiffusive nature of chaotic field lines has a counterpart in the subdiffusive nature of ion transport, as already shown elsewhere [125, 126].

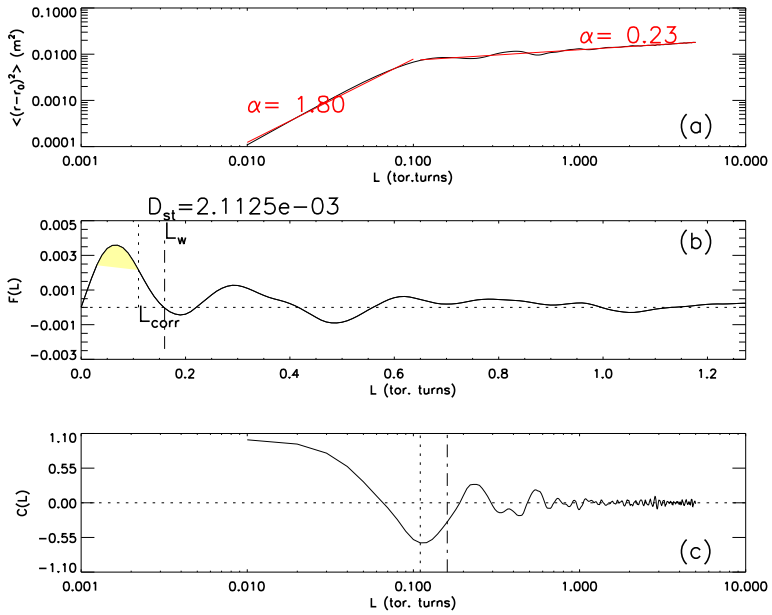

Figure 2.10: The quadratic mean square displacement (a), the correlation (b) and auto-correlation (c) functions for a bounded domain from ORBIT code. Run with number of field lines (10000), initiated at $\psi_p = 0.05$ and following them for 150 toroidal turns. The function F takes its maximum value close to $L = 0$, vanishes for a $L = L_w$ and then oscillates around zero, without reaching a diffusion regime. At the same time, the auto-correlation function $C(L)$ experiences a large domain of negative values, where the field trajectories are anti-correlated one to each other. This means that the probability of a radial jump having an opposite sign with respect to the preceding one is larger than that of retaining the same sign. This fundamentally is the definition of a *subdiffusive regime*.

For the calculation of the correlation length, we run the codes with the same number of field lines (10000), initiated at $\psi_p = 0.05$ ($r \approx 33\ cm$) and following them for 150 toroidal turns. The $C(L)$, $F(L)$ and $\langle (r-r_0)^2 \rangle$ curves (Figs. 2.10 - 2.11) show a similar behavior. The corresponding correlation lengths are

- $L_{corr} = 1.38\ m$ for ORBIT;
- $L_{corr} = 1.35\ m$ for NEMATO;

demonstrating again a very good agreement between the two codes.

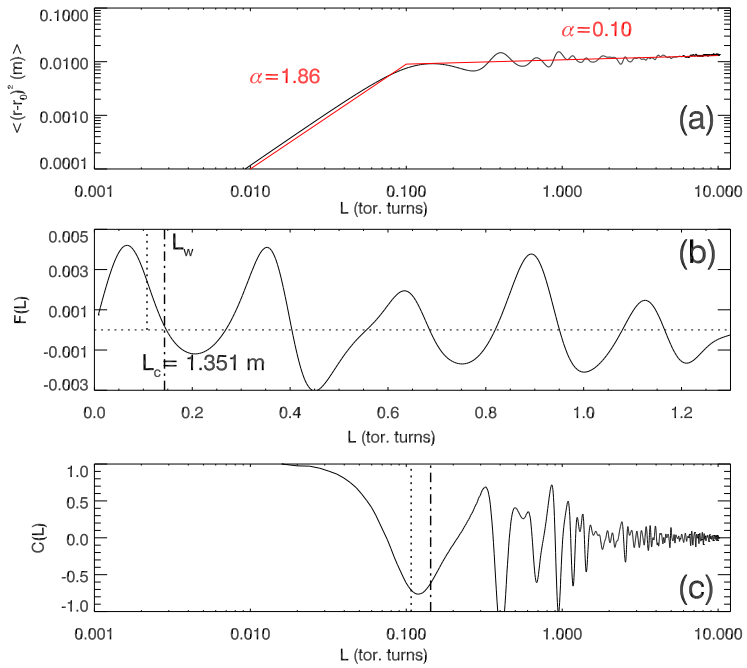

Figure 2.11: The quadratic mean square displacement (a), the correlation (b) and auto-correlation (c) functions for a bounded domain from NEMATO code. Run with number of field lines (10000), initiated at $\psi_p = 0.05$ and following them for 150 toroidal turns. NEMATO finds the subdiffusive regime, though with a more oscillatory behavior of the correlation function $F(L)$.

2.7 Summary and remarks

In this chapter, the benchmark between the guiding center code ORBIT and the solenoidal, field-line tracing code NEMATO has been shown. The code NEMATO is a volume-preserving integrator for solenoidal fields on a (cylindrical or toroidal) 3D grid, while ORBIT is a Hamiltonian guiding center code which describes test-particle motion in an electromagnetic field.

The aim of this numerical verification study is to assess the reconstruction of the magnetic topology in a reversed-field pinch, and to verify the validity of the gauge for the vector potential of the perturbations made in ORBIT. The benchmark can be divided into a qualitative and a quantitative test. In the first one, it has been verified that both codes give the same description of the flux surfaces when a single $m = 0$ and $m = 1$ mode is considered. Then, the comparison has been extended to the chaotic case, by direct evaluation of the Poincaré plots and with a quantitative estimate of the correlation length of field lines. The evaluation of the Poincaré plots shows a qualitative agreement in the spatial scales relevant for overall transport, while minor changes in the fine topological structure can be detected. These minor changes are not ascribed to the gauge assumption made by ORBIT on the magnetic field (which is fundamentally correct for a tearing mode), but on the different numerical scheme used for integration, namely, volume-preserving for NEMATO, step-adapting in ORBIT. As for the quantitative test is concerned, similar results can be drawn: the main features of the chaotic system are captured in the same way by NEMATO and ORBIT, in particular, the correlation length is the same in the two codes. More local metrics, such as the Lyapunov exponents and Lyapunov lengths, are of the same order of magnitude, but differ more than the correction length.

Chapter 3

Ion and electron transport with TEXTOR-DED

3.1 Introduction

In this chapter we deal with test-particle transport simulations at the stochastic edge of TEXTOR for a discharge in the $m/n = 12/4$ DED configuration, through the code ORBIT. The equilibrium of TEXTOR is reconstructed in circular approximation starting from experimental data. The magnetic field perturbations generated by the DED are included through an analytical formulation developed at TEXTOR [2, 45] re-adapted for ORBIT. As a first step magnetic field line structures are displayed with a Poincaré map and compared with previous results [115]. Kinetic Poincaré plots are performed to study the differences in drift motion of electrons and ions. Finally, two-fluid effects near the magnetic structures are analyzed through the calculation of the parallel connection length of ions and electrons and a rough estimation of the ambipolar, radial electric field. The whole analysis is carried out following what has been done in RFX-mod (see Sec. 1.2).

The chapter is organized as follows: in Sec. 3.2 TEXTOR equilibrium and magnetic field perturbation reconstructions are introduced; in Sec. 3.3 test-particle simulations (Poincaré plots, parallel connection length and radial electric field maps) are presented; in Sec. 3.4 we draw a summary and final remarks.

3.2 Magnetic configuration

In order to run ORBIT, the magnetic configuration of the TEXTOR device needs to implemented in the code, that is, equilibrium magnetic field and perturbations. The equilibrium is reconstructed from experimental data of the run considered. A magnetic field perturbation formulation is built starting from the current distribution over the coils of the DED.

3.2.1 Equilibrium

Being the TEXTOR device a circular tokamak the equilibrium can be derived analytically in circular approximation. For a toroidally symmetric equilibrium the Grad-Shafranov (GS) written in magnetic flux coordinates has the form

$$\nabla \cdot \frac{\nabla \psi_p}{X^2} + p' + \frac{gg'}{X^2} = 0 \tag{3.2.1}$$

where primes ($'$) indicate derivatives with respect to ψ_p. Eq. (3.2.1) can be expanded using the inverse aspect ratio as expansion parameter, $\epsilon = a/R$ (a and R are the minor and major radius of the torus, respectively). When the expansion is stopped at the second order the equilibrium surfaces consist of shifted circles, centered at the major radius $X(r, \theta) = 1 + r\cos\theta - \Delta(r)$, where $\Delta(r)$ is the shift, r and θ the geometrical minor radius and poloidal angle, respectively (see Fig. 3.1). Note that in ORBIT the shift is *zero* at minor radius $r = 0$. As such, $X = 1$ is the magnetic axis location in units of major radius [149].

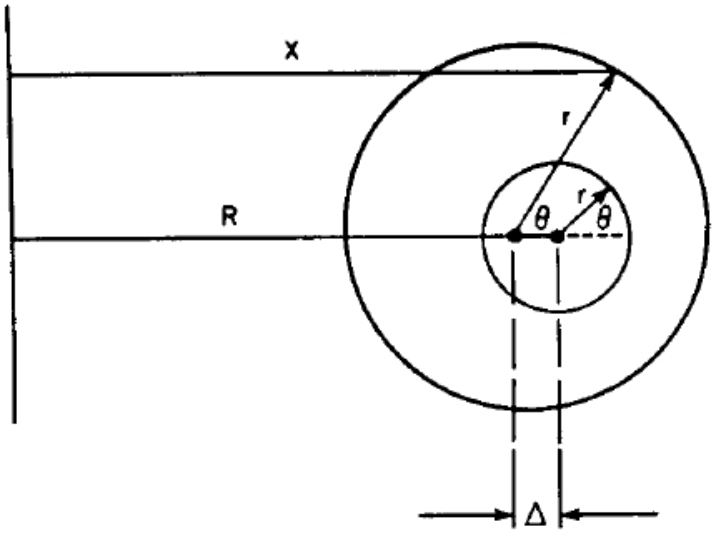

Figure 3.1: Flux surfaces for a second order equilibrium.

Expanding in ϵ (and assuming that the flux surfaces consist of shifted circles), Eq. (3.2.1) decouples in two parts, one θ-independent (Eq. (3.2.2a)) and the other θ-dependent (Eq. (3.2.2b)), with the latter being a 2nd order

toroidal effect.

$$p' + gg' + \frac{1}{q}\left(\frac{r^2}{q}\right)' = 0 \tag{3.2.2a}$$

$$\Delta'' + \left(\frac{2(r^2/q)'}{r^2/q} - \frac{1}{r}\right)\Delta' - \frac{2(r^2/q)'}{r/q} - 1 - \frac{2rgg'}{r^2/q^2} = 0 \tag{3.2.2b}$$

The first part does not take into account the corrections due to the toroidal geometry, and expresses the radial pressure balance equation for a cylindrical screw-pinch. Of the three functions p, g and q, only two can be chosen to define the equilibrium, the third comes from Eq. (3.2.2a). The second part, Eq. (3.2.2b), determines $\Delta(q, g)$, and thus the physical location of the flux surfaces in terms of the two functions defining the equilibrium. Therefore the equilibrium is completely defined choosing two functions among pressure, p, toroidal field, g, and safety factor, q.

To reconstruct TEXTOR equilibrium we use as input q, whose profile is obtained from the experimental measurements, and put $p = 0$ to calculate g. On the other hand, Δ is matched with the measured shift of flux surfaces, that contains the real pressure contribution. q and Δ experimental profiles are fitted with a high order polynomial whose parameters are given as input to the equilibrium module `eqs.f` of ORBIT. In Figs. 3.2 and 3.3 the experimental profile and those given by ORBIT are shown, for a sample run.

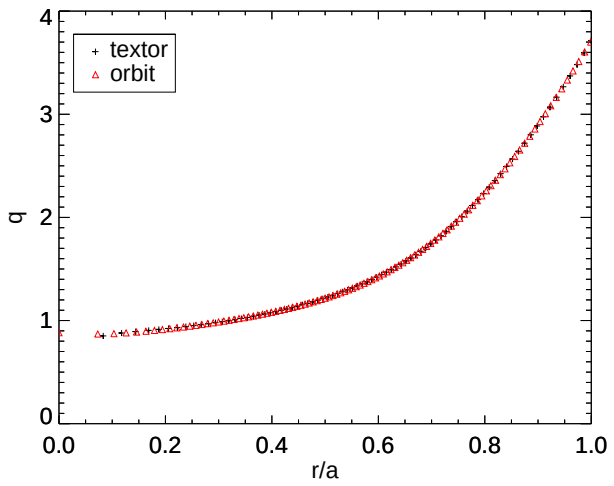

Figure 3.2: Experimental (black plus) and ORBIT reconstructed (red triangle) q profiles.

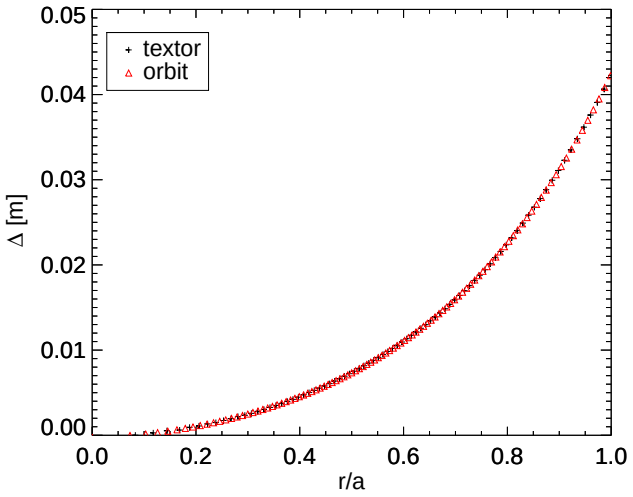

Figure 3.3: Experimental (black plus) and ORBIT reconstructed (red triangle) Δ profiles.

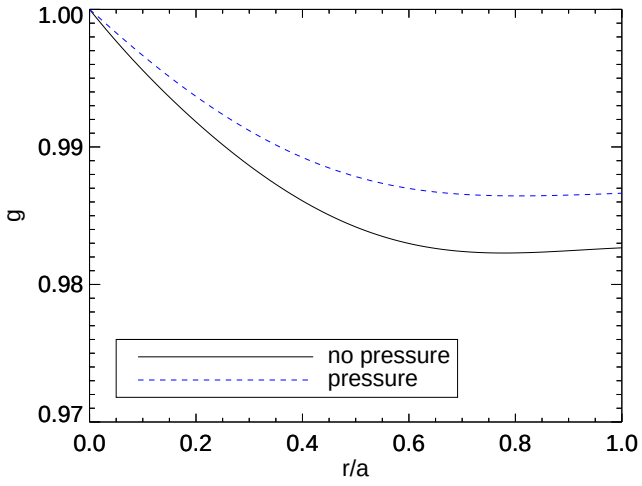

Figure 3.4: g profiles normalized to the field at the magnetic axis, without pressure (black line) and with pressure (dashed blue line).

It is worth to say that g could be derived from q and Δ. Introducing $f = r/q$, Eq. (3.2.2b) can be written as

$$\Delta'' + \left[\frac{2(rf)'}{rf} - \frac{1}{r}\right]\Delta' - \frac{2(rf)'}{f} - 1 - \frac{2rgg'}{f^2} = 0 \,, \tag{3.2.3}$$

from which the derivative of p with respect to ψ_p can be found:

$$p' = -\frac{f^2}{2r}\Delta'' + \left[\frac{f^2}{2r^2} - \frac{f(rf)'}{r^2}\right]\Delta' + \frac{f^2}{2r} \,. \tag{3.2.4}$$

Thus, inserting (3.2.4) in Eq. (3.2.2a) and explicating f, we find the g:

$$g^2(r^*) = 1 - 2\int_0^{r^*}\left[p'(r) + \frac{1}{q}\left(\frac{r^2}{q}\right)'\right]\mathrm{d}r \,. \tag{3.2.5}$$

In Fig. 3.4 the resulting g profile (normalized to the field at the magnetic axis) is shown together with the one calculated in force-free ($p = 0$) approximation: they only differ of 0.4%. Therefore, for the considered run, we can neglect the pressure term in the computation of the toroidal field, g, without complicating the equilibrium module.

3.2.2 Magnetic field perturbations

Magnetic field perturbations are calculated from the current distribution over the coils of the DED [44], whose configuration is sketched in Fig. 3.5 in the (θ,φ) plane. The model we are going to describe, developed by Sadrilla Abdullaev at TEXTOR [2, 45], does not take into account the plasma screening, but is based on the assumption of full penetration, the so-called "vacuum" approximation. Numerical simulations utilizing such approach, e.g. realized in the EMC3-Eirene code, were shown to be in good agreement with experimental findings in highly resistive edge plasmas with static RMP fields at high resonant field amplitudes [51]. The basic DED current distribution of the j-th coil (j=1,2,...,16) can be described as

$$I_j^{(n)} = I_d \sin\left(n\frac{2\pi j}{16} \mp \omega t + \chi_n\right) \qquad n = 1, 2, 4. \tag{3.2.6}$$

Here I_d stands for the amplitude of the current, and ω is a frequency of rotation of the magnetic field perturbation. The minus sign describes the co-rotating magnetic field perturbation, while the plus the counter-rotating one. In the remainder of this section, we will consider static RMP only, i.e. $\omega = 0$. The DED can operate in the so-called $m/n = 3/1,\ 6/2,\ 12/4$ operational modes creating magnetic perturbation with toroidal mode numbers

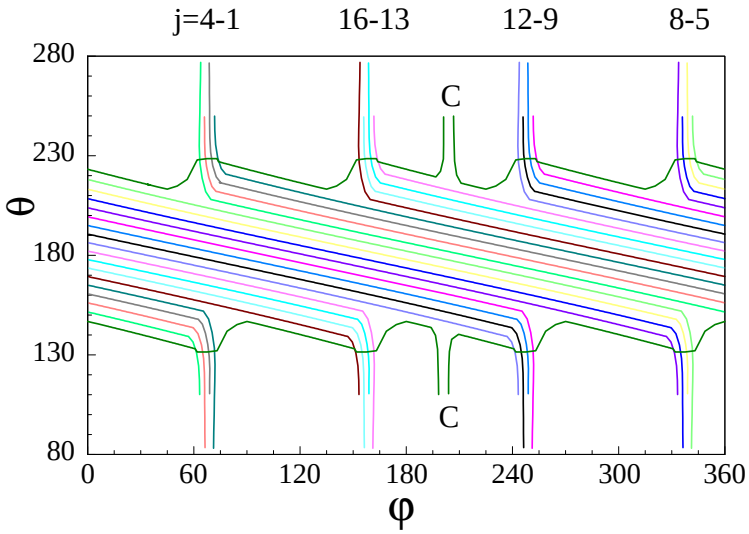

Figure 3.5: DED coil configuration in the (θ,φ) plane. Magnetic field perturbations are created by the current distribution over 16 helical coils located at the high field side and aligned parallel to the magnetic field lines, plus two compensation coils, which are switched on during the 12:4 mode operation to compensate the net perturbation field of n =0 toroidal mode.

$\hat{n} = n + 4s$ (s=0,1,2,...). An arbitrary DED current distribution is a linear combination of $I_j^{(n)}$:

$$I_j = \sum_n \iota_n I_j^{(n)} = I_d \sum_n \iota_n \sin\left(n\frac{2\pi j}{16} \mp \omega t + \chi_n\right) \qquad n = 1, 2, 4\ , \quad (3.2.7)$$

where the coefficients ι_n and the phases χ_n (see Appendix A) are

$$\iota_n = \left[\frac{\sin(\pi/4)}{4\sin(\pi/16)}, \frac{1}{2\sin(\pi/8)}, \sqrt{2}\right], \qquad \chi_n = \left[\frac{3\pi}{16}, \frac{3\pi}{8}, \frac{5\pi}{4}\right] \quad (3.2.8)$$

for the modes $n = 1, 2, 4$, respectively.
In order to find a magnetic perturbation formulation we introduce the density of DED current

$$\begin{aligned} &\vec{J} = J_r\vec{e}_r + J_\theta\vec{e}_\theta + J_\varphi\vec{e}_\zeta\ , \\ &J_r = 0\ , \\ &J_\theta = J(r,\theta,\varphi)\sin\alpha_0\ , \\ &J_\varphi = J(r,\theta,\varphi)\cos\alpha_0\ , \end{aligned} \quad (3.2.9)$$

where $\vec{e}_r$, $\vec{e}_\theta$, $\vec{e}_\zeta$ are unit vectors along the coordinates r, θ, ζ, respectively, $\alpha_0 \simeq 4.6^\circ$ is the angle between current direction and toroidal axis and

$$J(r,\theta,\varphi) = \delta(r-r_c)\sum_{j=1}^{16} I_j r_c^{-1}\delta(\theta-\theta_j(\varphi)) \tag{3.2.10}$$

is the module of the current density (θ_j is the poloidal position of the j-th coil and r_c =53.25 cm is the DED radius). Otherwise, considering the basic coil density current (i.e. considering only a single n mode) and explicating $I_j^{(n)}$, we get

$$\begin{aligned} J^{(n)}(r,\theta,\varphi) =& \delta(r-r_c)g(\theta,\varphi)\frac{I_d}{r_c} \\ & \sum_{j=1}^{16}\sin\left(n\frac{2\pi j}{16}+\chi_n\right)\delta(\theta-\theta_j(\varphi)) \ , \end{aligned} \tag{3.2.11}$$

where $g(\theta,\varphi)$ is a step function equal to 1 in the coil space and *zero* elsewhere:

$$\begin{aligned} & g(\theta,\varphi) = \begin{cases} 1, & \text{for } \pi-\theta_c(\varphi) < \theta < \pi-\theta_c(\varphi), \\ 0, & \text{elsewhere,} \end{cases} \\ & \theta_c(\varphi) = \theta_{c0} - \frac{2\Delta\theta}{\pi}(\varphi-\varphi_l) \qquad \text{for } \varphi_l < \varphi < \varphi_{l+1}, \\ & \varphi_l = \varphi_c + (l-1)\frac{\pi}{2}, \qquad 0 < \varphi_c < \frac{\pi}{2}, \qquad l = 0,1,2,3,4. \end{aligned} \tag{3.2.12}$$

The current density (3.2.11) can be transformed in the sum of continuous distributions (see Appendix B), using the delta Dirac function properties:

$$\begin{aligned} J^{(n)}(r,\theta,\varphi) =& \delta(r-r_c)g(\theta,\varphi)J_d \\ & \sum_{s=-\infty}^{\infty}\cos\left(\frac{m_0(16s-n)}{4}\theta+\frac{n_0(16s-n)}{4}\varphi+\chi_s^{(n)}\right) \ , \end{aligned} \tag{3.2.13}$$

where

$$\chi_s^{(n)} = \chi_n - \frac{m_0(16s-n)}{4}\theta_0 - \frac{\pi}{2} \ . \tag{3.2.14}$$

In Eq. (3.2.13) we introduced the following notation

$$\begin{aligned} J_d &= \frac{I_d}{r_c\delta\theta} \ , \\ m_0 &= \frac{\pi}{2\delta\theta} \simeq 20 \ , \\ n_0 &= \frac{\theta_c}{2\delta\theta} \simeq 4 \ , \\ \theta_0 &= \theta_{01} + \delta\theta \ , \end{aligned}$$

where $\theta_c = 35.49°$ is the half poloidal extension of a set of coils, $\delta\theta = 4.3364°$ is the angular distance between two coils, θ_{01} is the poloidal angle of the first coil at the toroidal angle $\varphi = 0$, $\theta_0 = 169.35°$ is the starting poloidal angle of the first coil.
Since $J(\theta, \varphi)$ is periodic along the toroidal angle with period 2π, n_0 is an integer equal to $n_0 = 4l$ with $l = 1, 2, ...$ Setting $n_0 = 4$ the term $s = 0$ gives the main contribution to the perturbed field in the plasma. If, for the sake of simplicity we consider only the term $s = 0$, we obtain:

$$J_0^{(n)}(r, \theta, \varphi) = \delta(r - r_c) g(\theta, \varphi) J_d \cos\left(\frac{m_0 n}{4}\theta + \frac{n_0 n}{4}\varphi - \chi_0^{(n)}\right) \tag{3.2.15}$$

and in complex representation

$$\tilde{J}_0^{(n)}(r, \theta, \varphi) = \delta(r - r_c) g(\theta, \varphi) J_d e^{i\left(\frac{m_0 n}{4}\theta + \frac{n_0 n}{4}\varphi - \chi_0^{(n)}\right)} . \tag{3.2.16}$$

For the calculation of the magnetic field it is convenient to present the current density (3.2.16) in Fourier series in θ and φ, with m and $\hat{n} = n + 4s$ positive:

$$\tilde{J}_0^{(n)}(r, \theta, \varphi) = \sum_{m,\hat{n}} \tilde{J}_{m\hat{n}}(r) e^{i(-m\theta + \hat{n}\varphi + \chi_{m\hat{n}})} , \tag{3.2.17}$$

with Fourier coefficients

$$\begin{aligned} \tilde{J}_{m\hat{n}}(r) =& \delta(r - r_c) J_d \frac{1}{(2\pi)^2} \\ & \int_0^{2\pi} \int_0^{2\pi} \mathrm{d}\theta \mathrm{d}\varphi \; g(\theta, \varphi) e^{-i\left(-m - \frac{m_0 n}{4}\right)\theta - i(\hat{n} - n)\varphi} . \end{aligned} \tag{3.2.18}$$

The Fourier coefficients corresponding to the term $s = 0$ ($\hat{n} = n$), which gives the main contribution to the perturbed field, are obtained in Appendix C and we get

$$\tilde{J}_{mn}(r) = e^{inm_0\pi/4} J_{mn}(r) , \tag{3.2.19}$$

where

$$J_{mn}(r) = \delta(r - r_c) J_d g_{mn} C_{mn} . \tag{3.2.20}$$

For the function $g(\theta, \varphi)$ given by Eq. (3.2.12) the coefficients g_{mn} and C_{mn} are determined by the expressions,

$$g_{mn} = \frac{\sin[(m - n\frac{m_0}{4})\theta_c]}{(m - n\frac{m_0}{4})\pi} \tag{3.2.21}$$

and $C_{mn} = 1$ for the ideal coil configuration shown in Fig. 3.6 (a), and

$$C_{mn} = \frac{\sin[(m - n\frac{m_0}{4})\frac{\Delta\theta}{2}]}{(m - n\frac{m_0}{4})\frac{\Delta\theta}{2}} . \tag{3.2.22}$$

for the non-ideal coil configuration (Fig. 3.6 (b)).

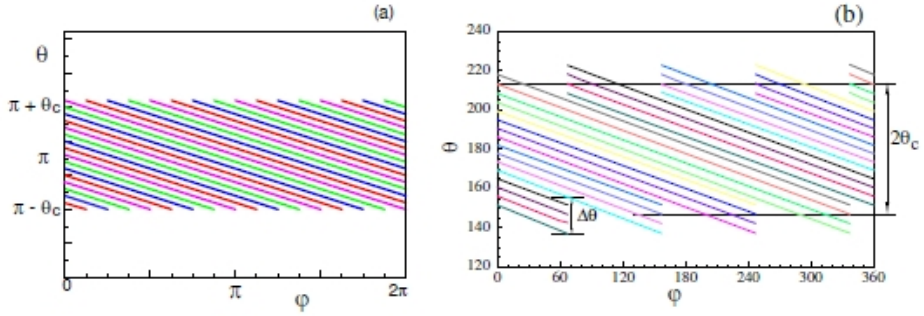

Figure 3.6: Models of DED coil configuration: ideal (a) and non-ideal (b) configuration.

Finally the perturbation current density in Fourier series is

$$J(r,\theta,\varphi) = \sum_{mn} J_{mn}(r)\cos(-m\theta + n\varphi + \chi_{mn}) \;, \tag{3.2.23}$$

with amplitude $J_{mn}(r)$ and phase

$$\chi_{mn} = \frac{m_0 n}{4}(\pi - \theta_0) - \chi_n + \frac{\pi}{2} \;. \tag{3.2.24}$$

where the phase χ_n is defined in Eq. (3.2.8).

The magnetic field created by the current (3.2.23) can be expressed, in cylindrical approximation, by the scalar potential

$$\Phi_{mn}(r,\theta,\varphi) = \begin{cases} a^i I_m(nr/R_c)\sin(-m\theta + n\varphi + \chi_{mn}) & \text{for } r < r_c, \\ a^e K_m(nr/R_c)\sin(-m\theta + n\varphi + \chi_{mn}) & \text{for } r > r_c, \end{cases} \tag{3.2.25}$$

where I_m and K_m are modified Bessel functions. From the boundary conditions at $r = r_c$

$$\begin{aligned} &B_r\big|_{r=r_c-0} - B_r\big|_{r=r_c+0} = 0 \\ &B_\theta\big|_{r=r_c-0} - B_\theta\big|_{r=r_c+0} = \mu_0 J_{mn} r_c \cos(-m\theta + n\varphi + \chi_{mn})\cos\alpha_0 \;, \end{aligned} \tag{3.2.26}$$

one can find the coefficients a^i, a^e and the radial component of the scalar potential (see Appendix D)

$$\begin{aligned} \Phi_{mn}(r) = a^i I_m(z) &= \mu_0 J_{mn}\cos\alpha_0 \frac{r_c}{2m}\left(\frac{r}{r_c}\right)^m = \\ &= B_c g_{mn} C_{mn}\frac{r_c}{m}\left(\frac{r}{r_c}\right)^m \;, \end{aligned} \tag{3.2.27}$$

where

$$B_c = \frac{m_0\mu_0 I_d \cos\alpha_0}{\pi r_c} \quad . \tag{3.2.28}$$

The final formula for the scalar potential of the magnetic field created by a set of helical currents inside the toroidal surface $r < r_c$ is

$$\boxed{\Phi(r,\theta,\varphi) = \sum_{m,n} \iota_n \Phi_{mn}(r) \sin(-m\theta + n\varphi + \chi_{mn})} \,, \tag{3.2.29}$$

where the coefficient ι_n and the phase χ_{mn} are defined in Eqs. (3.2.8) and (3.2.24), respectively.
From Eq. (3.2.29) one can derive the formula of the radial magnetic field

$$B_r(r,\theta,\varphi) = \frac{\partial \Phi}{\partial r} = \sum_{m,n} \iota_n B_{mn}(r) \sin(-m\theta + n\varphi + \chi_{mn}) \,, \tag{3.2.30}$$

where

$$B_{mn}(r) = B_c \; \iota_n \; g_{mn} \; C_{mn} \left(\frac{r}{r_c}\right)^{|m|-1} \,. \tag{3.2.31}$$

where the coefficient g_{mn} and C_{mn} are defined in Eqs. (3.2.21) and (3.2.22), respectively. The profiles of $B_{mn}(r)$ are shown in Fig. 3.7, for three different modes. It is worth noting that profiles of single modes in TEXTOR are peaked at the edge, while in RFX are peaked at the center(see Figs. 2.2 and 2.3).

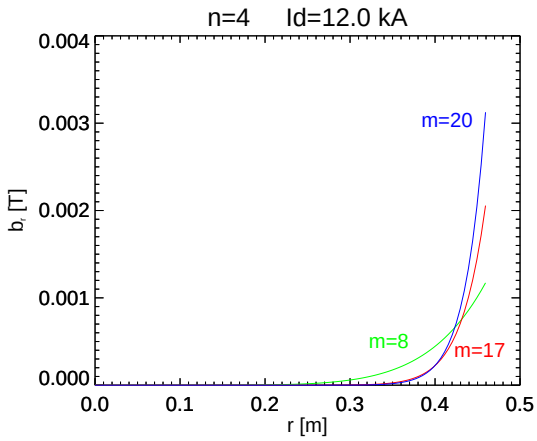

Figure 3.7: Radial magnetic perturbation profiles created by means of Eq. 3.2.31 for $I_d \sim 12\ kA$, $n = 4$, $m = 8, 17, 20$.

B_r can be used in Eq. (2.2.62) to get the α function once we find the relation between the phase, χ_{mn} and the phase of α, ϕ_{mn}. In ORBIT the radial magnetic field is defined as

$$B_r(r,\theta,\varphi) = \sum_{m,n} \iota_n B_{mn}(r) \cos(m\theta - n\varphi + \phi^{(O)}_{mn}) \,. \tag{3.2.32}$$

Thus, we impose

$$\begin{aligned}\cos(m\theta - n\varphi + \phi_{mn}^{(O)}) &= \sin(-m\theta + n\varphi + \chi_{mn}) = \\ &= \cos(m\theta - n\varphi + \pi/2 - \chi_{mn}) \ ,\end{aligned} \tag{3.2.33}$$

which means $\phi_{mn}^{(O)} = \pi/2 - \chi_{mn}$. Finally, since α is a sine function (see Sec. 2.2.3) the phase to be inserted in ORBIT is

$$\phi_{mn} = \phi_{mn}^{(O)} - \frac{\pi}{2} = -\chi_{mn} \ . \tag{3.2.34}$$

3.3 Test particle simulations

We consider a TEXTOR discharge with static RMP (DC DED current with amplitude 12 kA) in the $m/n = 12/4$ operational mode. The reconstructed spectrum including $m = 1 - 24$ modes is shown in Fig. 3.8(a). It is worth noting that the spectrum is far from being monochromatic as it is, for instance, in the RFX-mod helical states [78]. As an example, in Fig. 3.8(b), the typical spectrum of a discharge in RFX-mod with dominant mode $m/n = 0/1$ is reported to be compared with TEXTOR spectrum. The spectra are reported in terms of α and not B^r, since both in TEXTOR and RFX the toroidal effects are remarkable. This is a significant difference since in RFX-mod the symmetry of the ambipolar potential is well defined, with a monochromatic 0/1 or 1/7 magnetic spectrum [140]. This allows for an easier understanding of the behavior of E^r in a simpler environment. On the contrary, in TEXTOR, the rich spectrum of perturbation gives rise to a rather complex edge topology, with at least two chains of clearly recognizable magnetic islands, and bundles of chaotic field lines touching the wall [152, 115, 113]. As a first in analyzing ion and electron transport in this topology, we compare ORBIT results from TEXTOR to existing ORBIT analysis for both, natural multi-helicity (MH) and helical (QSH) states at RFX.

3.3.1 Poincaré plots

The Poincaré plot of the magnetic field lines in TEXTOR is shown in Fig. 3.9. We deposit 100 magnetic field lines at $\psi_n \simeq 0.89$ and 0.92, $\zeta = 0$, θ random, and follow them for 1000 toroidal turns. In the remainder of the Thesis, we will use the normalized poloidal flux, $\psi_n = \psi_p/\psi_{p,w}$, where $\psi_{p,w} \simeq 0.0205$ ($r = 46$ cm) is the value of ψ_p at the wall, as a radial coordinate in the poloidal section. Fig. 3.9 shows the typical magnetic topology of TEXTOR: in the inner region the last main island chain, in the middle the remnant island where neighboring resonant flux surfaces overlap and the field lines get stochastic, and in the outermost region the so-called laminar flux tubes embedded into ergodic finger like structures, are found. The

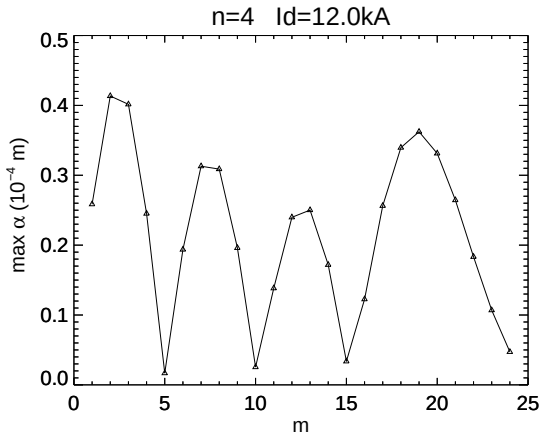

(a)

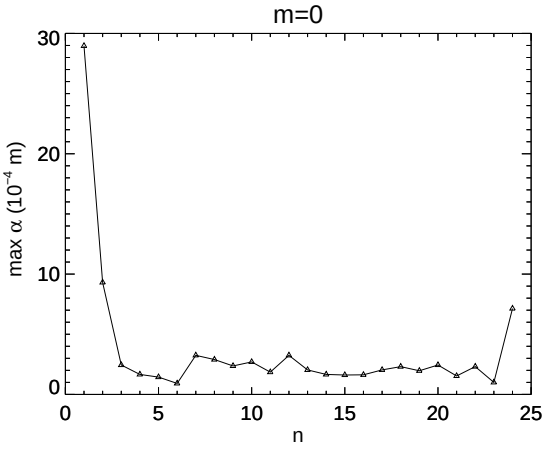

(b)

Figure 3.8: Perturbation spectra of TEXTOR, for $n = 4$ and of $Id \sim 12\ kA$(a), and of RFX for $m = 0$ (b).

topology described by ORBIT is in very good agreement with the results obtained with GOURDON [115].

In addition to the description of the magnetic topology, ORBIT is capable of giving information about particle motion, complementing studies on the effect of a chaotic magnetic field on drift motion, already done at TEXTOR [1]. As a first step, we can plot a "kinetic" Poincaré plot, which is the record of intersection points of particle crossing the poloidal section perpen-

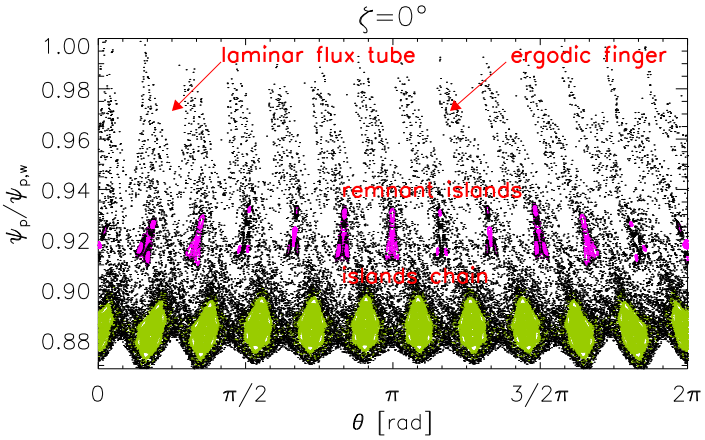

Figure 3.9: Poincaré plot at $\zeta = 0°$ of magnetic field lines. The x-axis is the poloidal angle while the y-axis is the poloidal flux coordinate normalized to the value at the wall. The last main island chain in green, the remnant island in violet, and in the outermost region the so-called laminar flux tubes embedded into ergodic finger like structures, can be observed.

dicular to the magnetic flux: it does not give any information about time (iterates on the section are a periodic function of time), and therefore about transport, but it is a fairly easy way of assessing the effect of a particular mode on a particle distribution [143]. We deposit 100 test particles (ions and electrons per run) with pitch angle $\lambda = v_{\parallel}/v = 1$ (passing particles), setting the same spatial initial conditions of the magnetic field Poincaré plot, and follow them for 1000 toroidal turns. Consider ions and electrons with a typical energy of 50 eV: we expect to see a different behavior between the two species. Ions, having a larger Larmor radius than electrons, will experience larger perpendicular displacement of their drift orbit while electrons closely follow magnetic field lines. Kinetic Poincaré plots of electrons and ions (Fig. 3.10) show that a charge separation arises and increases with the test particle energy, as expected (50 eV, 100 eV, and 1 keV). In particular, remnant islands are shifted from their original resonance in the kinetic plot for high-energy ions, which is an effect found for fast ions in RFP, too [43, 60].

3.3.2 Connection length maps

As a first quantitative indicator of the transport properties of TEXTOR edge ($\psi_n > 0.86$, $r \gtrsim 41$ cm), we analyze the parallel connection length of the topology shown in Fig. 3.9. Here, the parallel connection length is defined by $L_{\parallel}(\psi_p, \theta, \zeta) \simeq v_{th}\tau_{trav}$, with τ_{trav} being the particle travel time

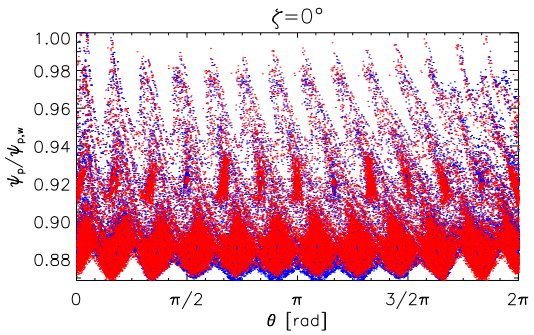

(a)

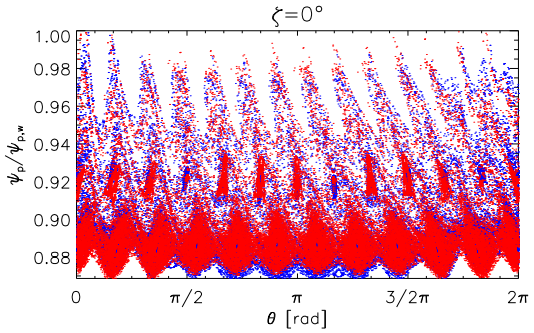

(b)

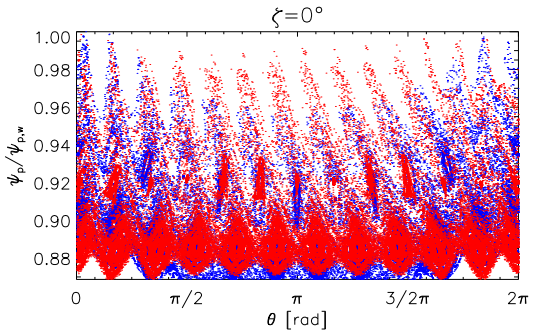

(c)

Figure 3.10: Kinetic Poincaré plot at $\zeta = 0°$ of monoenergetic electrons (red) and ions (blue) with energy 50 eV (a), 100 eV (b), 1000 eV (c). This is the record of intersection points of particle crossing the poloidal section perpendicular to the magnetic flux. Ions, having a larger Larmor radius than electrons, drift perpendicularly while electrons closely follow magnetic field lines. Then, a charge separation arises and increases with the test particle energy.

between initial $(\psi_{n,0}, \theta_0, \zeta_0)$ and final positions $(\psi_{n,1}, \theta_1, \zeta_1)$, and v_{th} the thermal velocity. Historically, the parallel connection length was first introduced in Tore Supra to describe the SOL of the Ergodic Divertor (ED) [87]. The name itself "connection length", originally described the path along $\vec{B}$ connecting a given ED module to the wall. Now it is a widely used metric of SOL-like transport when RMPs are applied [152]. parameter, λ. The implementation of a full profile, energy scattering operator in ORBIT is an ongoing work, presently no exchange of energy is considered.

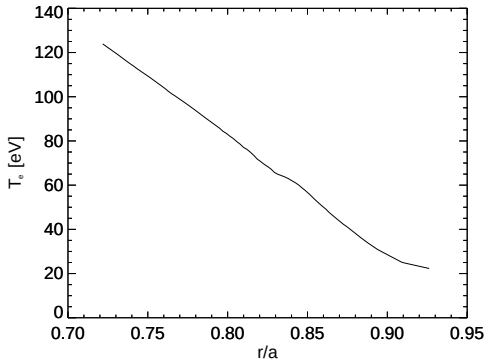

(a)

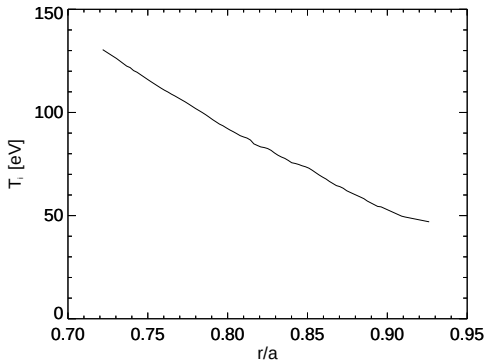

(b)

Figure 3.11: Electron (a) and ion (b) temperature radial profiles obtained through the transport code EMC3-Eirene in unperturbed conditions.

Collisions enter through a pitch-angle Monte-Carlo scattering operator, implemented by taking into account ion-ion, ion-electron, electron-electron, and electron-ion encounters, using the Kuo-Boozer approach [16]. The pitch-

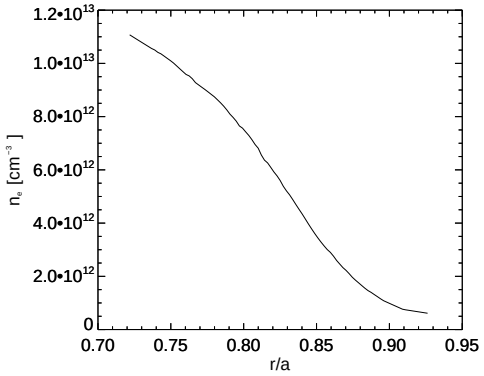

Figure 3.12: Electron density radial profile obtained through the transport code EMC3-Eirene in unperturbed conditions.

angle scattering operator thus describes the exchange of momentum between particles, due to Coulomb scattering. This is realized in the code as a diffusion operator in the space of the "pitch" parameter, λ. The implementation of a full profile, energy scattering operator in ORBIT is an ongoing work, presently no exchange of energy is considered.

Initial and final conditions are $(\psi_{n,0}, \theta_0, random)$ and $(\psi_{n,1}, random, random)$, respectively, with $\psi_{n,1} = \psi_{n,0} + \Delta\psi_n$, where $\Delta\psi_n = 2.2 \cdot 10^{-2}$. We define a grid of $(\psi_{n,0} \times \theta_0)$=(24×25) points with $\theta_0 \in [-\pi, \pi]$ and $\psi_{n,0} \in [0.86, 0.97]$ where to deposit test particles. For each point we perform a single run. We launch 1000 monoenergetic particles with energy $\in [23, 79]$ eV (depending on the radial position of the starting point) and collision frequency (per toroidal transit) $\nu_e \tau_{tor} = 1.5$ (=thermal collisions), and follow them for 5000 toroidal turns. The energy of the test particles, temperature and background density have been obtained through the transport code EMC3-Eirene in unperturbed conditions [69] and their radial profiles are shown in Figs. 3.11(a) and 3.11(b) for temperature, and Fig. 3.12 for density. Particles reaching the plasma magnetic axis ($\psi_n \approx 0.005$) are removed from the run, but the final clock that sets the end of the run is determined by particles leaving the outermost boundary, $\psi_{n,1}$. The run ends when half of the particles crosses the collection surface $\psi_{n,1}$ and τ_{trav} is the run time [123]. The choice of stopping the run with a half-loss condition is arbitrary, but it allows for evolving the system until it reaches the equilibrium between conserved and lost particles, with good statistics to define the outward fluxes [96].

Figs. 3.13 - 3.14 show contour maps of ion and electron $L_\parallel$, over-plotted to the Poincaré map of Fig. 3.9. The color map indicates the values of $L_\parallel$, obtained from each run, in function of the deposition point coordinates $(\psi_{n,0}, \theta_0)$. Electrons, having a smaller Larmor radius, follow the field lines

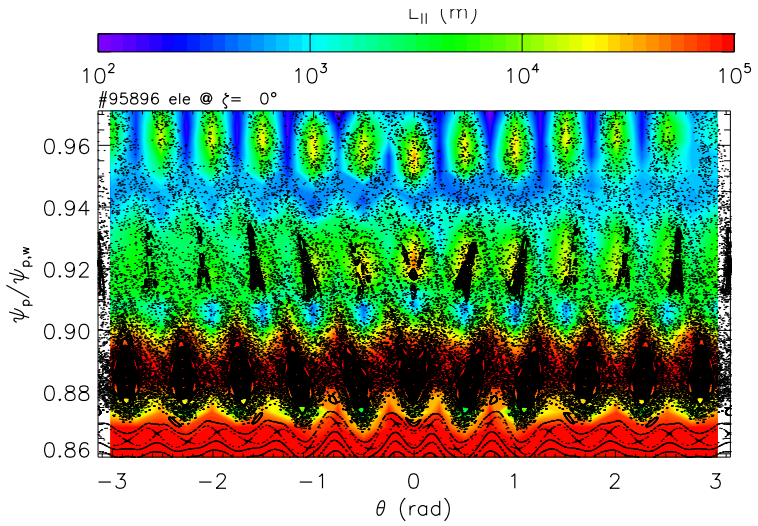

(a)

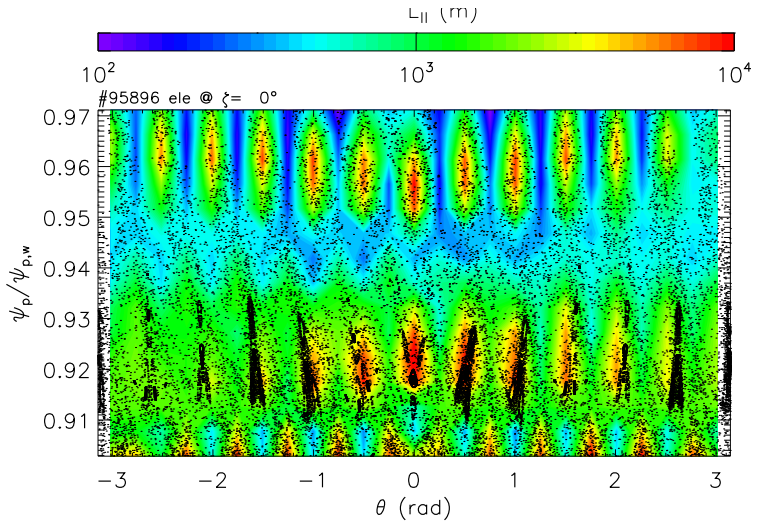

(b)

Figure 3.13: Field line Poincaré plot at $\zeta = 0°$. The color code indicates the electron $L_{\|}$ value. In panel (a) three main regions are seen: the main island chain ($\psi_p/\psi_{p,w} \simeq 0.89$), characterized by very large values ($\simeq 60\ km$), the O-point (OP) of the remnant island ($\psi_p/\psi_{p,w} \simeq 0.92$) and of the ergodic fingers ($\psi_p/\psi_{p,w} \simeq 0.96$) with large values ($\simeq$ 10-25 km). Panel (b) is a zoom of the outermost edge ($\psi_p/\psi_{p,w} > 0.90$) and shows that $L_{\|}$ decreases poloidally moving away from $\theta = 0$. This is likely to be caused by the DED being placed at $\theta = \pi$

closely and, as a consequence, $L_{\|}$ is shaped by the magnetic topology, as

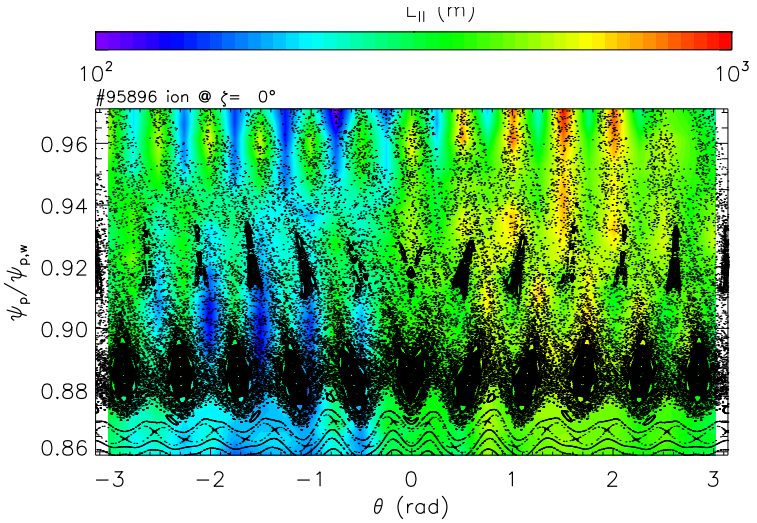

Figure 3.14: Field line Poincaré plot at ζ =0. The color code indicates the ion $L_\parallel$ value. The ion $L_\parallel$ values are small ($\lesssim 1\ km$) compared to electrons as their Larmor radius is larger. A poloidal asymmetry with slightly higher values in the positive region $\theta > 0$ (upper half of the torus) can be noticed, due to the vertical θ-pinch drift. This up-down asymmetry is averaged out over the toroidal angle φ and makes no contribution to the final E^r.

shown in Fig. 3.13(a). Three main domains can be distinguished in the radial direction: the main island chain ($\psi_n \simeq 0.89$), characterized by very large values ($\simeq 60\ km$), the O-point (OP) of the remnant island ($\psi_n \simeq 0.92$) and of ergodic fingers ($\psi_n \simeq 0.96$) with large values ($\simeq$ 10-25 km). The rest of the edge has small values $L_\parallel \approx 0$, and electrons are directly connected to the wall. Typical values of electron and ion transit times are shown in Tables 3.1 - 3.2. Poloidally, a decrease of $L_\parallel$ is seen in the outermost plasma edge ($\psi_n > 0.90$), moving away from $\theta = 0$ (see Fig. 3.13(b)). This is caused by the increasing radial field strength when approaching the vicinity of DED coils placed at $\theta = \pi$. Regarding electrons we have to remark two points:

1. the spots of high $L_\parallel$ at the intersection point of the ergodic fingers match in shape and position the results from magnetic field modeling with ATLAS [115];

2. in the remnant island chain, electron $L_\parallel$ is larger at the OP and not at the XP, as it is the case in RFX in both the $(0, 1)$ [123] and $(1, 7)$ [140] symmetries (see also Fig. 1.10). In this respect, it is worth noting that in both symmetries of the RFP, the XPs correspond to the extremum of the q profile, the helical $q'_h = 0$ in the $(1, 7)$ case [56] and the axis symmetric $q = 0$ in the $(0, 1)$ case [124]. The presence of q extrema makes the XPs resilient to chaos [32]. This could explain why $L_\parallel$ is larger at the XPs in RFX. Anyway, a run of $L_\parallel$ as a function of

mode amplitude should make clear if a dependence on the magnetic spectrum is also important. This is an ongoing work. In fact, it is worth recalling that hyperbolic fixed points (XP) are characterized by long periods T_{XP} up to a threshold in the perturbation amplitude, beyond which T_{XP} rapidly decreases [22]. Beyond this threshold, XPs are known to be seeds of stochastization [37].

Table 3.1: Typical values of ion travel times in selected regions of the TEXTOR stochastic edge, 12/4 configuration.

	ions		
	τ_{trav} (ms)	v_{th} (m/s)	$L_{\parallel}$ (km)
main island chain	1-5	1.1 10^5	0.1-0.5
OP remnant	1-5	9.0 10^4	0.1-0.5
ergodic fingers	4-9	7.2 10^4	0.3-0.7
laminar flux tubes	1-3	7.2 10^4	0.1-0.2

Table 3.2: Typical values of electron travel times in selected regions of the TEXTOR stochastic edge, 12/4 configuration.

	electrons		
	τ_{trav} (ms)	v_{th} (m/s)	$L_{\parallel}$ (km)
main island chain	7-12	4.8 10^6	35-60
OP remnant	2-4	4.0 10^6	8-16
ergodic fingers	2-4	3.1 10^6	6-12
laminar flux tubes	0.05-0.4	3.1 10^6	0.1-1

Ions, having larger Larmor radius, experience larger drift extent from the flux surface. Consequently, the ion $L_{\parallel}$ values are small ($\lesssim 1\ km$) compared to electrons. Despite this, a poloidal asymmetry with slightly higher values in the positive region $\theta > 0$ (upper half of the torus) can be noticed (Fig. 3.14). The asymmetry cannot be explained by the magnetic field perturbation (such as the DED poloidal location), but it is the effect of the vertical θ-pinch drift that is dependent on charge (note that our simulations are performed at the same φ). In order to validate this, we launched two ion simulations. The first has no perturbations and positive charge, and its $L_{\parallel}$ map (Fig. 3.15(a)) shows the same poloidal asymmetry as the case with perturbations. The second run, with no perturbations and negative charge, shows a map with specular asymmetry (Fig. 3.15(b)). The application of a

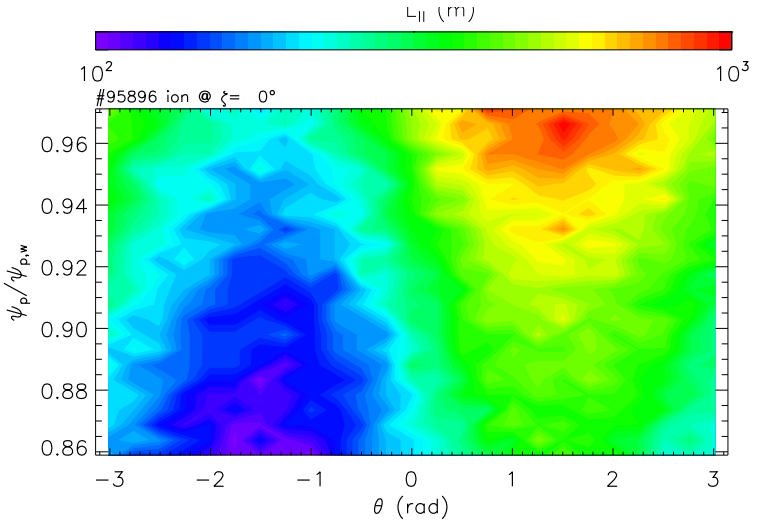

(a)

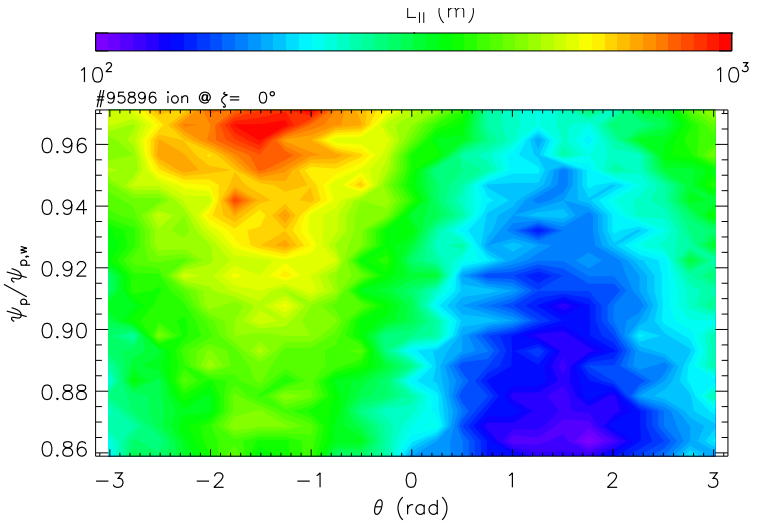

(b)

Figure 3.15: $L_{\|}$ map for positive (a) and negative (b) ions with no perturbations. The vertical θ-pinch effect pushes the positive ions in the upper half of the torus ($\theta > 0$), and the negative ions in the downer half ($\theta < 0$).

magnetic field perturbation slightly changes this downward asymmetry, as can be seen plotting the 1D distribution of the final θ position of the lost ions, i.e. the particles crossing $\psi_{p,w}$. Fig. 3.16(a) and Fig. 3.16(b) show the θ distributions of all of the ions (red), and the ions that are not lost, final $\psi_p < \psi_{p,w}$ (blue), without and with field perturbation, respectively. The difference of the red and blue distributions gives the number of ions

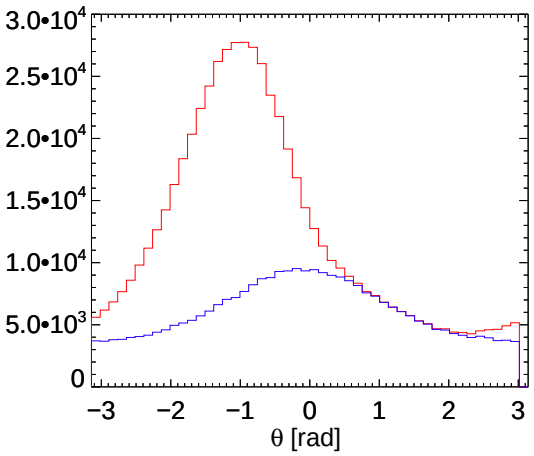

(a)

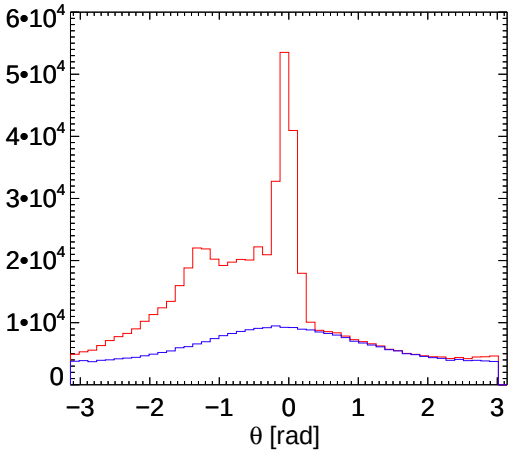

(b)

Figure 3.16: Distribution of final θ position of ions without (a) and with (b) perturbations: in red all of the ions, in blue the ions that are not lost, final $\psi_p < \psi_{p,w}$, and from their difference the number of ions lost. The application of a magnetic field perturbation slightly changes this downward asymmetry: while in the case with no perturbation the distribution is peaked at $\theta \simeq -1$, where $L_\parallel$ is small, the field perturbation shifts the peak to $\theta \simeq 0$ with still a majority of ions lost downwards, reflecting the topology.

lost. While in the case with no perturbation the distribution is peaked at $\theta \simeq -1$, where $L_\parallel$ is small (see Fig. 3.15(a)), the field perturbation shifts

the peak to $\theta \simeq 0$ with still a majority of ions lost downwards, reflecting the topology shown in Fig. 3.13(b). However, this up-down asymmetry in the ion $L_{\|}$ is finally averaged out over the toroidal angle φ and makes no contribution to the final E^r.

3.3.3 Radial electric field map

The connection lengths shown in Sec. 3.3.2 for electrons and ions are expected to generate a radial electric field, E^r, modulated along θ. E^r can be derived starting from the ion and electron radial fluxes

$$\begin{cases} \Gamma_i^{tot} = -D_i \delta^r n_i + n_i \mu_i E^r \ , \\ \Gamma_e^{tot} = -D_e \delta^r n_i + n_e \mu_e E^r \ , \end{cases} \tag{3.3.1}$$

and imposing the steady state condition ($\Gamma_i^{tot} = \Gamma_e^{tot}$). The diffusion terms are substituted with the simulated geometrical particle fluxes ($\Gamma_i = -D_i \delta^r n_i$, $\Gamma_e = -D_e \delta^r n_e$) and the ion mobility is neglected since $\mu_i \ll \mu_e$. Thus, one gets

$$E^r = \frac{1}{n|\mu_e|}(\Gamma_e - \Gamma_i) \ , \tag{3.3.2}$$

where $\Gamma \propto \frac{1}{\tau_{trav}}$ and $n = n_e = n_i$ is the background density. Then, E^r is roughly estimated assuming a classical μ_e. It is important to underline that with this calculation we neglect wall effects, such as particle recycling, which are fundamental in RFX to give the correct sign to E^r [123]. As shown in Fig. 3.17, E^r is positive almost everywhere near the wall ($\psi_n > 0.90$), which is expected when electron transport is enhanced through magnetic stochasticity, in a situation of no recycling [107]. It can also be noticed that E^r decreases within the laminar flux tubes at $\theta \in [-1, 0]$, following the asymmetry of the distribution of lost ions (see Fig. 3.16(b)): in fact, where ions are preferably lost, the ambipolar field required is also smaller. On the contrary, the region where the magnetic structures trap the electrons (main island chain, OP of remnant islands and ergodic fingers) is characterized by negative E^r values.

Generally speaking, E^r shows the same symmetry of the magnetic topology, $m = 12$, so that a modulation along θ of the ambipolar potential is expected to be measured in the TEXTOR device. This confirms the results found in RFX-mod simulations [123] and experiment [140], where the ambipolar potential has the symmetry of the main island $(m, n) = (0, 1)$ in the MH, and $(1, 7)$ in QSH [140]. On the other hand, the module of E^r is ~ 1 order of magnitude larger in TEXTOR than in RFX-mod. This can be ascribed either to the simplified calculation of Eq. (3.3.2) where the electron mobility is calculated from the classical formulas, and not self-consistently from ORBIT runs; or to the difference in the behavior of the electron $L_{\|}$, in RFX-mod vs TEXTOR. In fact, high values of E^r in TEXTOR laminar

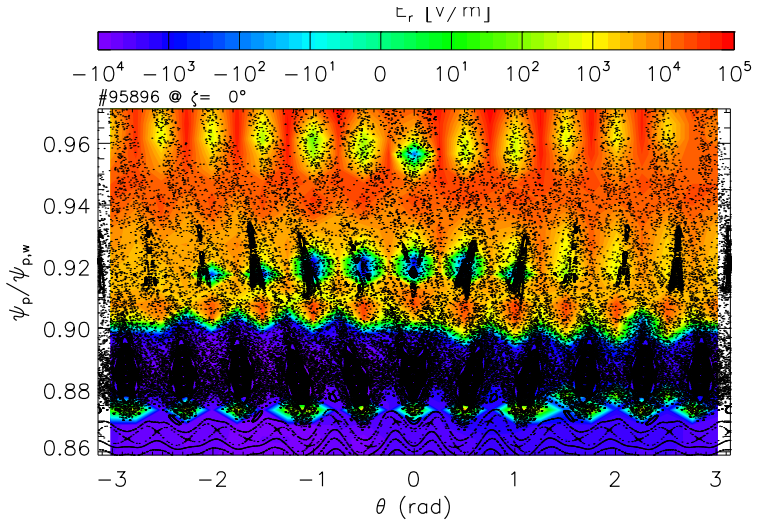

Figure 3.17: Map of the radial electric field roughly estimated, neglecting the ion mobility. The color scale indicates the radial electric field value. E^r is positive almost everywhere near the wall ($\psi_p/\psi_{p,w} > 0.90$), which is expected when electron transport is enhanced through magnetic stochasticity, in a situation of no recycling. E^r decreases within the laminar flux tubes at $\theta \in [-1, 0]$, following the asymmetry of the distribution of lost ions, since where ions are preferably lost, the ambipolar field required is also smaller. On the contrary, the region where the magnetic structures trap the electrons (main island chain, OP of remnant islands and ergodic fingers) is characterized by negative E^r values.

flux tubes are due to a ratio $\tau_{\mathrm{trav},i}/\tau_{\mathrm{trav},e} \sim 60$, while in RFX the maximum ratio is ~ 15 (see Table 1 in Ref. [127]). On the contrary, the minimum values are similar in the two devices ($\tau_{\mathrm{trav},i}/\tau_{\mathrm{trav},e} \sim 2 \div 4$). Excluding the laminar flux region, both $\tau_{\mathrm{trav},e}$ and $\tau_{\mathrm{trav},i}$ in TEXTOR are larger than in RFX by one order of magnitude. Such a difference cannot be ascribed to different density regimes in the two devices: at TEXTOR $n/n_G \simeq 0.5$, while at RFX-mod $n/n_G = 0.2 \div 1.0$ in MH configuration and $n/n_G < 0.35$ in QSH configuration [140]. Moreover, RFX-mod simulations have shown E^r to be independent of the collision frequency, and thus on the density, at least with pitch-angle scattering only (see Fig. 12 in Ref [127]). This means that islands in RFX are characterized by a larger degree of chaos (excluding laminar flux tubes), even if a more precise assessment requires a scan of the local D_e, D_i in TEXTOR islands, as a function of the perturbation amplitude, which is an ongoing work.

3.4 Summary and remarks

In this chapter we have shown a study of the magnetic topology and related transport in the edge of the TEXTOR tokamak, with the DED. Test-particle transport simulations of a discharge in the $m/n = 12/4$ DED configuration have been performed by means of the code ORBIT, similarly to what has been done in the RFX-mod RFP. ORBIT has been adapted to TEXTOR, by reconstructing the equilibrium and the magnetic field perturbations generated by the DED.

The Poincaré maps of the magnetic field show the expected structures at the TEXTOR edge: in the inner region, the last main island chain, in the middle the remnant islands and in the outermost zone the so-called laminar flux tubes embedded in the ergodic fingers. Kinetic Poincaré plots show a small charge separation between electrons and ions (as in the RFP case), and a dependence of this charge separation on energy (in experiment: electron temperature, heating).

The parallel connection length analysis highlights the properties of the magnetic structures observed in the Poincaré plot. Coulomb collisions of monoenergetic particles with exchange of momentum have been considered (no exchange of energy). While ions, having a large Larmor radius, are weakly affected by the magnetic topology, electron trajectories are more closely related to to the magnetic field lines. Electrons are trapped in the main island chain, the O-points of the remnant islands and in the ergodic fingers. The zones in between the island chain, the remnant islands and the ergodic fingers are characterized by a smaller connection length. In particular, in the zones between the ergodic fingers (the so-called laminar flux tubes) the parallel connection length is almost vanishing. This inward expansion of the SOL causes a drop in the particle confinement (pump out) [40, 114] which, however, is smaller than for cases where edge magnetic islands are present. This issue will be addressed in Chapter 4, since in this case the $m/n = 3/1$ base mode configuration of the DED has to be considered. The ion connection length shows an additional poloidal asymmetry due to the vertical θ-pinch drift, that causes a peak of lost ions downwards in the poloidal section.

Finally, we have shown that the behavior of connection lengths entails a characteristic modulation of the radial electric field, with large positive values in the zones with electron $L_\parallel \approx 0$ (laminar flux tubes, region between main island chain and remnant islands). On the contrary, $E^r < 0$ in the regions where electrons are trapped, such as the main island chain, the OP of the remnant island and the ergodic fingers. As already found in RFX-mod simulations and experimental measurements, E^r has the same symmetry as the magnetic topology, suggesting that the mechanism of the edge ambipolar potential is the same in Tokamaks and reversed-field pinches. In this respect, our studies predict that a modulation along θ of E^r should be visible in the

TEXTOR device, as well as in all of the tokamaks where RMPs are applied (DIII-D [40] and ASDEX [132]).

Chapter 4

Electrostatic response to RMP islands in TEXTOR

4.1 Introduction

In this chapter we continue the characterization of the magnetic topology at the edge of the TEXTOR device. In particular, we focus on the transport properties of the $m/n = 4/1$ islands created near the LCFS by the DED in the 3/1 configuration. At TEXTOR, measurements of electrostatic potential inside and outside the island suggest that this structure acts as a particle pump-out system. In order to investigate the transport features of such a structure, we perform with ORBIT particle transport simulations in the 3/1 configuration. We calculate the test-particle diffusion coefficients (electrons, D_e, and ions, D_i) in the $m = 4$ island by computing the particle flux in a local helical domain. This domain can be shifted along the poloidal angle to sample transport properties from the O-point through the X-point of the island. Finally, we present a model of the ambipolar potential for the 4/1 island and compare it with the measurements. Results will be compared with similar analysis done at RFX-mod for the $m/n = 0/1$ case (see Ref. [123] and Sec. 1.2.4).

The Chapter is organized as follows: in Sec. 4.2 we show the Poincaré plot of the magnetic topology with applied perturbation fields in the DED 3/1 configuration; in Sec. 4.3 we calculate D_e and D_i between the O-point and the X-point of the 4/1 island; in Sec. 4.4 we find a model of the ambipolar potential and compare it with experimental measurements; in Sec. 4.5 we present a summary and final remarks.

4.2 Poincaré plot

Similarly to what done in Chapter 3, we consider a TEXTOR discharge with static RMP, but in $m/n = 3/1$ operational mode with $I_d = 1.2\ kA$.

The reconstructed $n = 1$ spectrum including $m = 1 - 24$ modes is shown in Fig. 4.1. It is worth noting that the $n = 1$ spectrum is more peaked in the m harmonics, compared to the $n = 4$ case. This is useful for the local evaluation of the diffusion coefficients in the remnant island, since the resulting magnetic topology is simpler, as we will see in Sec. 4.4.

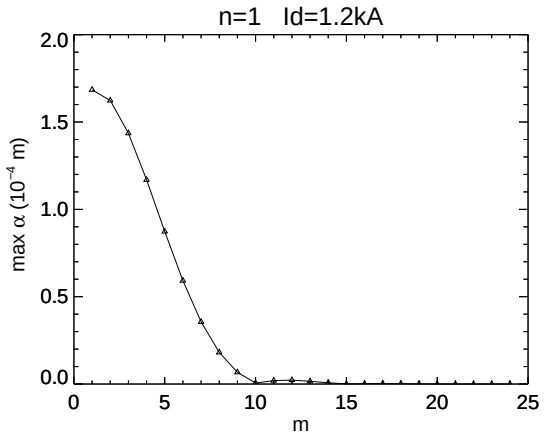

Figure 4.1: Reconstructed spectrum of the $(m, n = 1)$ modes generated by the DED in 3/1 configuration, for a current amplitude of 1.2 kA.

The Poincaré plot of the magnetic field lines for the $n = 1$ modes is shown in Fig. 4.2. We proceed similarly to the $n = 4$ case: depositing 100 magnetic field lines at $\psi_n \simeq 0.89$ and 0.92, $\zeta = 0$, θ random, and following them for 1000 toroidal turns. The plot shows in the inner region the last main island chain composed by three conserved structures, in the middle four remnant islands and in the outermost region the laminar flux tubes embedded into the ergodic "fingers".

4.3 Particle diffusion coefficients

We perform a simulation to evaluate the local radial transport of particles inside and outside the 4/1 islands. We deposit particles on an initial 4/1 closed helical flux surface $\psi_{h,1}$, and we let them diffuse until they reach a larger surface $\psi_{h,2}$, nested with the same helical axis. Then, particles are redeposited on $\psi_{h,1}$. By letting each particle to perform at least ~ 30 cycles in and out $\psi_{h,2}$, we obtain steady-state local density distributions, with a measured flow of particles across $\psi_{h,2}$: the ratio between flux and density gradients gives the local transport rate.

In fact, particle transport in toroidal configurations is usually described

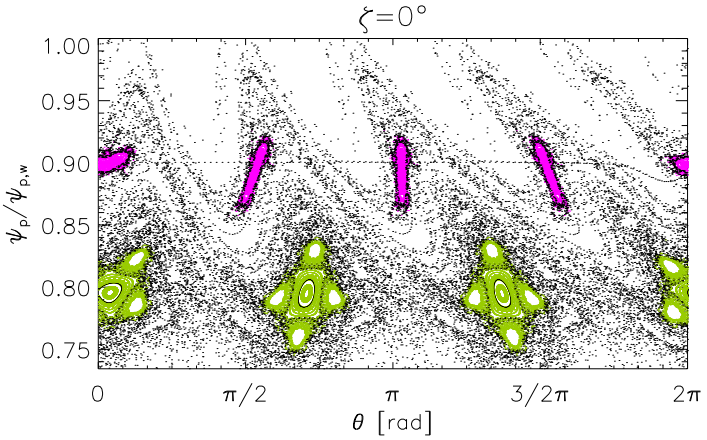

Figure 4.2: Poincaré plot at $\zeta = 0°$ of magnetic field lines. The x-axis is the poloidal angle while the y-axis is the poloidal flux coordinate normalized to the value at the wall. The last main island chain in green, the remnant island in violet, and in the outermost region the so-called laminar flux tubes embedded into ergodic finger like structures, can be observed.

by splitting the particle flux into a diffusive and a pinch term:

$$\Gamma = -D\nabla n + nv \; . \tag{4.3.1}$$

The steady-state solution to Eq. 4.3.1 with source at $x = 0$ and sink at $x = \pm\Delta/2$, and with D, v constant, is symmetric in x and given for $x > 0$ by

$$n = \frac{\Gamma}{v}\left[1 - e^{v/D(x-\Delta/2)}\right] \; . \tag{4.3.2}$$

In the limit of $v \to 0$ we have $n = (\Gamma/D)[(\Delta/2) - x]$. For this distribution the density gradient is simply given by the inverse of the domain size, it is not related to the actual equilibrium density gradient. A triangular profile as a function of $x = r - r_1$ is the natural steady-state distribution for diffusive motion given source at r_1 and sink at r_2 [125], where r is the radius in the poloidal section.

The helical flux surfaces $\psi_h^{(4,1)}$ are obtained from Eq. (2.2.60) setting $m = 4$ and $n = 1$:

$$\psi_h^{(4,1)} = 4\psi_p - \psi - (4g + I)\alpha_{4,1}\sin(4\theta - \zeta + \phi_{4,1} + \phi) \quad 0 < \phi < \pi \; . \tag{4.3.3}$$

The domain is radially centered at the $q = 4$ resonance, $\psi_{p,0} = 0.0140$ ($r_0 = r(\psi_{p,0}) \approx 36\ cm$), and bounded by the inner closed helical flux surface, $\psi_h^{(4,1)} = 0.0318375 = \psi_{h,1}$, where test particles are deposited, randomly distributed in ψ_p, θ and ζ, and by the outer closed helical flux $\psi_h^{(4,1)} =$

$0.0318244 = \psi_{h,2}$. The value of $\psi_{h,2}$ is chosen to fit as good as possible the borders of the 4/1 island since our interest is to evaluate the local radial transport in its OP and XP. It is worth noting that the Poincaré plot of the 4/1 island (purple points in Fig. 4.2) slightly deviates from the helical flux surfaces due to the non-linear interaction with the 3/1. In any case, for the purpose of this Chapter, the mismatch does not affect significantly the evaluation of D.

Now define $r_1 = |r(\psi_{h,1}) - r_0|$ and $r_2 = |r(\psi_{h,2}) - r_0|$ as the radial distance of points lying on the boundary surfaces from the helical axis (i.e. the OPs of $\psi_h^{(4,1)}$). The relevant length to calculate D is the width $\Delta = r_2 - r_1$, which has to be large compared with the banana width and gyro-radius. In the end, we let collapse $\psi_{h,1}$ on the helical axis, and therefore, $r_1 = 0$ and $r_2 = \Delta$. In Fig. 4.3, the closed helical flux surfaces are displayed together with $\psi_{h,2}$ and the resonance layer. In the simulation particles exiting the domain

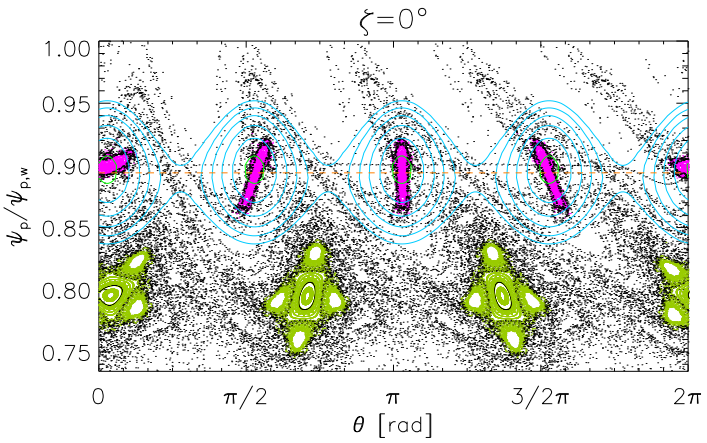

Figure 4.3: Poincaré plot at $\zeta = 0°$ of magnetic field lines. The x-axis is the poloidal angle while the y-axis is the poloidal flux coordinate normalized to the value at the wall. In light blue the closed helical flux surfaces $\psi_h^{(4,1)}(\phi = 0)$ are over plotted. In light green $\psi_{h,2}$ is highlighted, while the orange, dashed line represents the $q = 4$ resonance layer.

are reinserted at r_1 with random pitch, θ, ζ. The run time, τ, is chosen long enough to allow all particles to perform several cycles through the domain, leading to a steady-state distribution (we set 100 toroidal transits, $\tau \approx 8\ ms$). The domain radial width Δ is divided into smaller bins of size δ in order to determine the steady-state density profile.

To find the density n and the particle flux Γ we need to calculate the area of the domain. The helical flux surfaces can be approximated by an *Archimedes' serpentine* [71]. The Archimedes' serpentine is a cyclic helical

surface generated by a helical motion of a circle. The helix has the following parametric form for a set of "cylindrical" coordinates (X, Z, l) with l the arc length subtending the toroidal angle φ:

$$\begin{cases} X(\theta) = & R + a\cos\theta \ , \\ Z(\theta) = & a\sin\theta \ , \\ l(\theta) = & R\varphi \quad 0 < \theta < 2\pi \ , \end{cases} \tag{4.3.4}$$

where R is the major radius and a the distance between the helix axis and the magnetic axis. The length of the helix is

$$\mathcal{L} = \int_0^{2\pi} \mathrm{d}\theta \sqrt{x'(\theta)^2 + y'(\theta)^2 + z'(\theta)^2} = \int_0^{2\pi} \mathrm{d}\theta \sqrt{a^2 + R^2 q^2} \ , \tag{4.3.5}$$

where we used $\mathrm{d}\varphi/\mathrm{d}\theta = q$. The area of Archimedes' serpentine surface is, then,

$$\mathcal{A} = \int_0^{2\pi} \mathrm{d}\eta \ b\mathcal{L} = \int_0^{2\pi} \mathrm{d}\eta \ b \int_0^{2\pi} \mathrm{d}\theta \sqrt{a^2 + R^2 q^2} = 4\pi^2 b \sqrt{a^2 + R^2 q^2} \ , \tag{4.3.6}$$

where b is the radius of the circle normal to the helix. If we use the values reported in Sec. 4.4, namely

$$\begin{aligned} & q = 4 \ , \\ & R = 1.81 \ m \ , \\ & a = r_0 \approx 0.36 \ m \ , \\ & b_2 = \langle r_2 \rangle \approx 3.6 \cdot 10^{-3} \ m \ , \\ & b_1 = \langle r_1 \rangle \approx 8.0 \cdot 10^{-5} \ m \ , \end{aligned}$$

we obtain the following values for the Archimedes' serpentine areas with minor radius b_2 and b_1, respectively:

$$\begin{aligned} & \mathcal{A}_2 \approx 1 \ m^2 \ , \\ & \mathcal{A}_1 \approx 2.3 \cdot 10^{-2} \ m^2 \ . \end{aligned}$$

In order to get a visual representation of the surface, it is convenient to transform to a Cartesian system and parametrize the surface with (t, u), which are nothing else but the spherical angles:

$$\begin{cases} x(t,u) = & [R + a\sin(t/q) + b\cos(u)]\cos(t) \ , \\ y(t,u) = & [R + a\sin(t/q) + b\cos(u)]\sin(t) \ , \\ z(t,u) = & a\cos(t/q) + b\sin(u) \quad 0 < t < 8\pi \quad 0 < u < 2\pi \ . \end{cases} \tag{4.3.7}$$

Finally, Figs. 4.4 - 4.5 show a picture of the surface and its sections for an arbitrary set of normalized values of R, a, b, and $q = 4$, in Cartesian coordinates.

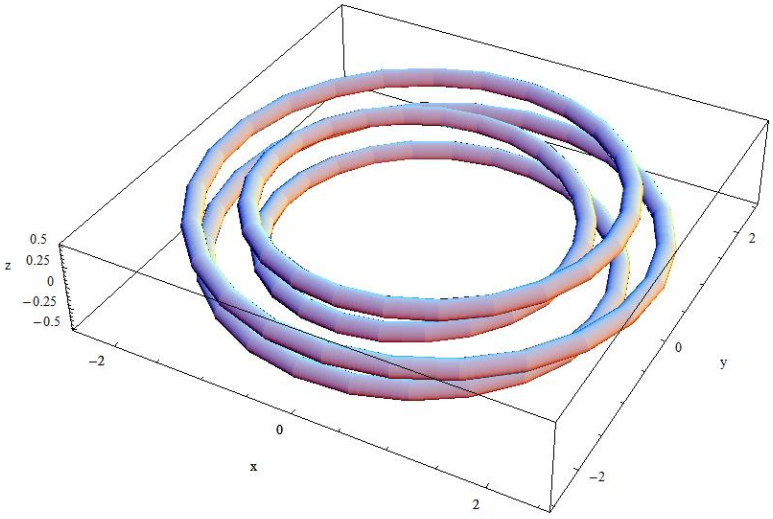

Figure 4.4: Archimedes' serpentine surface in Cartesian coordinates (x, y, z) with normalized values $R = 2$, $a = 1$, $b = 0.1$.

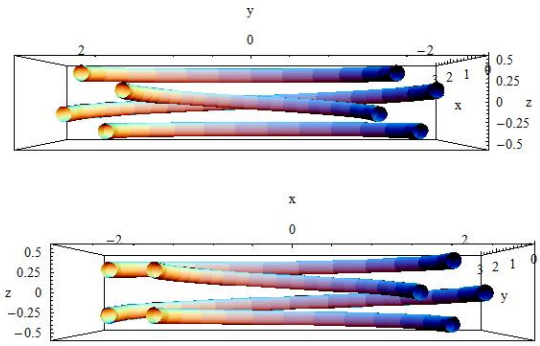

Figure 4.5: Archimedes' serpentine sections $x = 0$ (up) and $y = 0$ (down) in Cartesian coordinates (x, y, z) with normalized values $R = 2$, $a = 1$, $b = 0.1$.

We can now calculate n and Γ, given by

$$n(x_\delta) = \frac{\#\text{ particles in a bin}}{\delta\ \mathcal{A}_1\ \text{timesteps}}\ , \tag{4.3.8}$$

$$\Gamma = \frac{\#\text{ lost particles}}{\tau\ \mathcal{A}_2}\ , \tag{4.3.9}$$

where $\mathcal{A}_2$ and $\mathcal{A}_1$ are the Archimedes' serpentine areas with minor radius $\langle r_2 \rangle$ and $\langle r_1 \rangle$, respectively ($\langle ... \rangle$ stands for an average over all test particles

and timesteps). Finally D and v can be evaluated fitting the curve $n(x)$ defined by Eq. (4.3.2).

As an example we report the ion and electron density profiles found in the OP. The particle collision frequency is thermal, $\nu\tau_{tor} \approx 1.5$ (τ_{tor} is the collisionless on-axis toroidal transit time), while particle energy is $E \approx 102\ eV$ (value deduced from the EMC3-Eirene code, see Fig. 3.11(a) 3.11(b)).

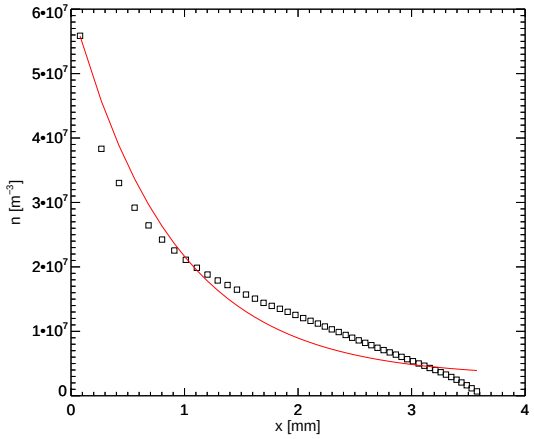

(a)

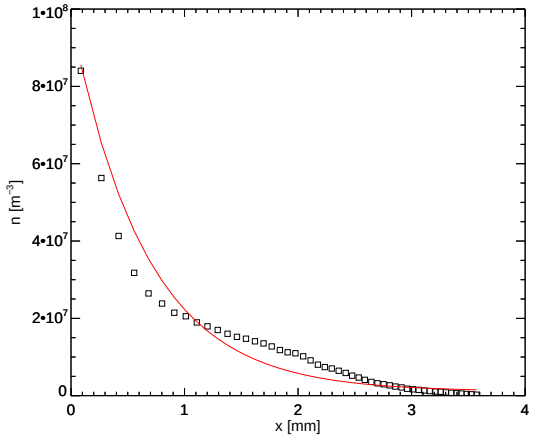

(b)

Figure 4.6: Density profile in the OP of $(m, n) = (4, 1)$ island for ions (a) and electrons (b). The black empty squares are the n values and the red line is the fitting curve.

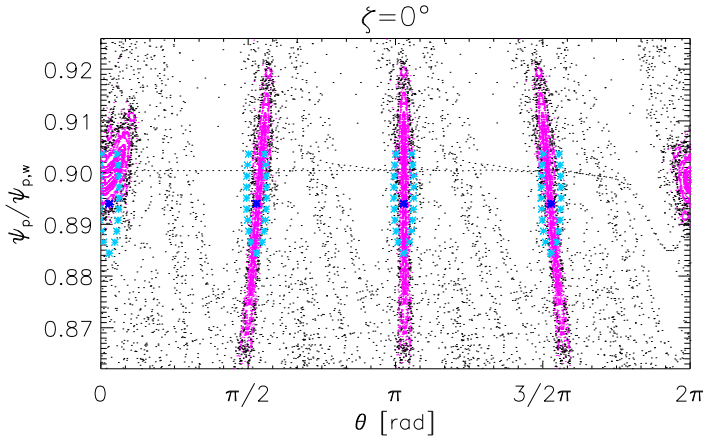

(a)

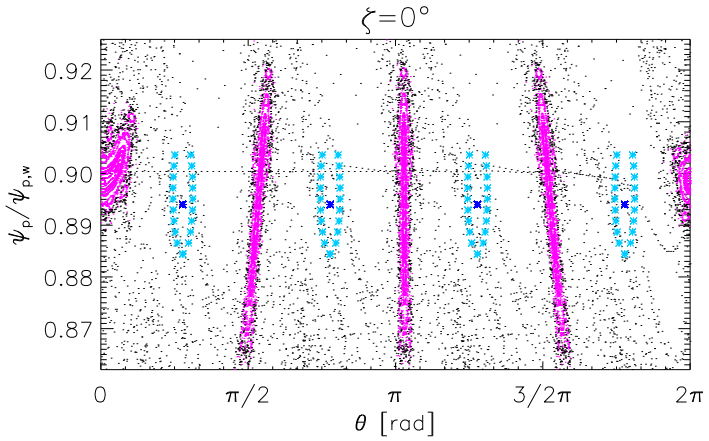

(b)

Figure 4.7: Poincaré plot at $\zeta = 0°$ of magnetic field lines. The x-axis is the poloidal angle while the y-axis is the poloidal flux coordinate normalized to the value at the wall. The points at r_1 (dark blue) and at r_2 for the calculation of the radial transport of particles in the OP, i.e. $\phi = 0$, (a) and XP, i.e. $\phi = \pi$, (b) are over plotted to the remnant islands (in violet).

The domain radial width is $\Delta \approx 7.00\ mm$ (ion Larmor radius $r_{L,i} \approx 0.86\ mm$, $\Delta/r_L \approx 8$), and the Archimedes' serpentine areas are $\mathcal{A}_2 \approx 1\ m^2$, $\mathcal{A}_1 \approx 0.023\ m^2$. In Fig. 4.6 the density profiles for ions and electrons are shown together with the fitting curve. The skewed density profiles indicate that nonlocal effects, induced by stochasticity, are clearly present, as already shown for global chaos in RFX [125, 126]. As a consequence, $v \neq 0$. We anyway consider only the value of D, with the caveat that in a nonlocal

system D depends on Δ [126]. It is also worth noting that in Fig. 4.6(b) electrons show a more pronounced skewness, which is consistent with the fact that they are more sensitive to magnetic chaos. The resulting diffusion coefficients are $D_i \approx 9 \cdot 10^{-2}\ m^2/s$ for ions (almost neoclassical $D_i^{neo} \approx 8 \cdot 10^{-2}\ m^2/s$, while the classical coefficient is $D_i^{cl} \approx 7 \cdot 10^{-3}\ m^2/s$) and $D_e \approx 6 \cdot 10^{-1}\ m^2/s$ for electrons ($D_e^{neo} \approx 3 \cdot 10^{-1}\ m^2/s$ and $D_e^{cl} \approx 2 \cdot 10^{-4}\ m^2/s$).

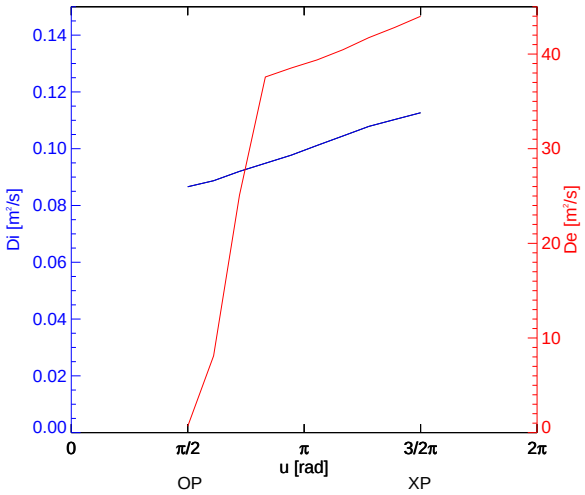

Figure 4.8: D_i and D_e values along the helical flux in between the OP and XP. On the x-axis the helical angle $u = m\theta - n\zeta + \phi$.

The domain, which up to now has been described for the OP only, can be shifted towards the XP by varying ϕ in Eq. (4.3.3), i.e. $\phi = 0$ for the OP and $\phi = \pi$ for the XP (see Fig. 4.7). By performing a series of steps in ϕ, we evaluate the diffusion coefficients along θ, between the OP and the XP. Actually, instead of θ, it is convenient to plot the diffusion coefficients as a function of the helical angle, $u_{m,n}$ with $m/n = 4/1$. The angle $u_{m,n}$ has been introduced in Sec. 1.2.3. The result is shown in Fig. 4.8. D_i is rather constant along the path ($\approx 0.1\ m^2/s$), and it is almost neoclassical, while D_e is larger, with typical values in a stochastic field [125, 126] ($0.6 \div 40\ m^2/s$). More important, D_e is strongly modulated along u (larger at the XP, lower at the OP), consistently with the parallel connection length maps shown in Sec. 3.3.2 and with the potential measurements that will be shown in Sec. 4.4. Finally, it is worth noting that, in a small domain right into the OP, $D_e \approx D_i$, which would bring, accordingly to Eq. (1.1.9), a vanishing radial electric field, $E^r \approx 0$. Actually, this result is supported by measurements of poloidal flow v_θ inside the 1/1 island in the LHD stellarator, which show a

plateau of $v_\theta \approx 0$ just right into the OP, which corresponds to $E^r \approx 0$ [66].

4.4 Ambipolar potential

In this Section we will present the measurement of plasma potential performed inside and outside an $m = 4$ island located at the edge of TEXTOR when the DED works in the 3/1 operational mode. Using the information that D_e is modulated along θ (see Fig. 4.8), we will develop a 3D model of ambipolar potential, which depends on θ. In fact, the difference between the ion and electron diffusion, shown in Sec. 4.3, must be immediately balanced by an ambipolar potential, which retains the symmetry of the fastest species, i.e. the electron. This information is embedded in ORBIT by including an analytic function, $\Phi(\psi_p, \theta, \zeta)$, in the Hamiltonian of the guiding-center (2.2.9). This is not a self-consistent approach, but it is easy to implement since electron and ion simulations can be run separately. Self-consistent approaches with ORBIT can be feasible but they require long runs (electron time step is $\sqrt{m_e/m_i}$ smaller than ions), and huge statistics to determine the potential from the electron/ion distributions.

4.4.1 The measurements of potential

A fast Mirnov probe located at the HFS of the TEXTOR device measures the potential in the region of the 4/1 island. The island is created and put into rotation in the poloidal direction, by inducing co-current rotating 3/1 fields through the DED at low current (1.2 kA). The probe is inserted at several radial positions of the plasma boundary, and at the same time the OP of the island is shifted poloidally.

Fig. 4.9(a) shows a coloured map of the measured plasma potential V_p as a function of the radial distance from the LCFS (x-axis), and of the poloidal steps of the island (y-axis). The map shows a structure resembling the magnetic topology of the 4/1 island. The area covered by the measurements corresponds to the region highlighted in the sketch of the island in Fig. 4.9(b). It is worth noting that ORBIT particle transport simulations, presented in Sec. 4.3, are consistent with the measurements: the potential well corresponds to the region with larger D_e (XP), while the potential increases and D_e decreases moving to the OP, both in poloidal and radial directions.

If we re-map the measurements in the (r,θ) plane, an impressive matching of the V_p shape with the magnetic topology can be noted. This is shown in Fig. 4.10, where the helical flux surfaces $\psi_h^{(4,1)}$ and the magnetic field Poincaré map are overplotted to V_p. In particular, the matching is very strong in the region outside the separatrix, while inside V_p does not follow exactly the flux surfaces.

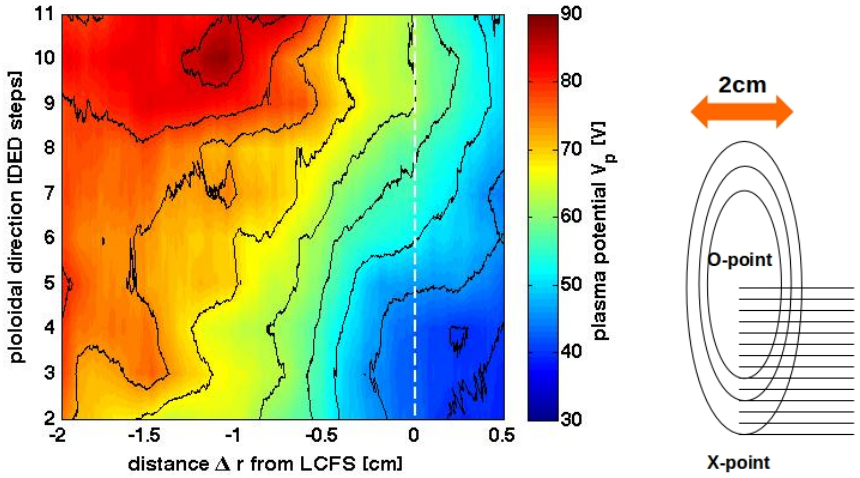

(a) (b)

Figure 4.9: (a) Map of the measured plasma potential: the potential value is indicated in a color bar, in the x-axis and y-axis are reported the radial distance from the LCFS and the poloidal steps of the rotating island, respectively; (b) the sampled region is highlighted with horizontal black lines in a sketch of the 4/1 island. The potential increases moving to the OP both in poloidal and radial directions. The potential well stays in correspondence with the XP.

4.4.2 The model for the potential

The results of test-particle simulations performed with ORBIT in Chapter 3, already showed a modulation of the considered quantities ($L_{\|}$, E^r, D) as a function of (r, θ), being footprints of the magnetic topology at the edge of TEXTOR. In Sec. 4.4.1, we have shown that the measurements of plasma potential well match the magnetic topology, too. As a consequence, we are leading up to think that the ambipolar potential Φ has to be modeled on the geometry of the islands.

The simpler choice is to impose Φ to have exactly the same geometry of $\psi_h^{(4,1)}$, and leaving the amplitude Φ_0 and phase $\tilde{\phi}$ as free parameters:

$$\Phi = \Phi_0 \, \psi_h^{(4,1)}(\tilde{\phi}) \tag{4.4.1}$$

The underlying assumption is that electrons rapidly flow along the helical surface ψ_h, and they shortcut any potential difference on the surface. Unfortunately, with this choice the leading radial term goes like $\Phi \propto \psi_p$, which corresponds to a small radial electric field, constant along r, which is clearly in contrast with measurements. This is not surprising since the radial profile of E^r is influenced by several factors, such as plasma wall interaction, the

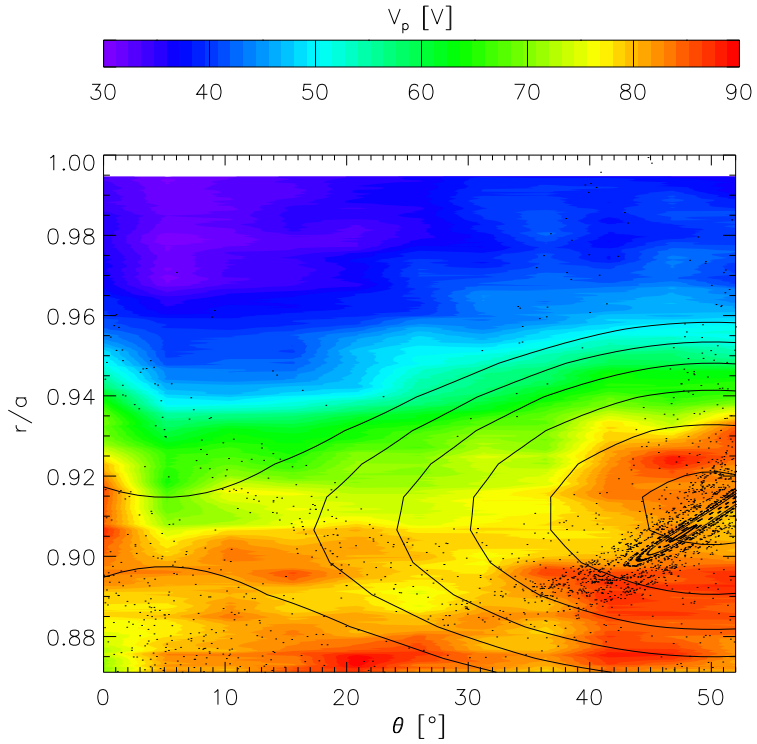

Figure 4.10: Map of the measured plasma potential V_p as a function of the poloidal angle θ and the normalized radius r. Its amplitude is indicated in the color bar. The helical flux surfaces $\psi_h^{(4,1)}$, Eq. (4.3.3), (black lines) and the magnetic field Poincaré plot (black points) are overplotted to the map.

velocity shear profile, electrostatic turbulence and blobs [4]. Thus, in order to find a good analytical formulation of Φ, we need to mix an experimental radial profile and simulation observations along θ, in the wake of RFX-mod (see Sec. 1.2.4). The simplest form for Φ can be written as

$$\Phi(\psi_p, \theta, \zeta) = \Phi_0 \left(f_1 + \frac{1}{2}(f_2 - f_1) \sin(-m\theta + n\zeta + \tilde{\phi}) \right) , \qquad (4.4.2)$$

where

$$f_i(\psi_p) = V_{p,i}^{min} + \frac{1}{2}(V_{p,i}^{max} - V_{p,i}^{min}) \left(1 - \tanh\left(\frac{\psi_p - \psi_{p,i}}{\Delta\psi_{p,i}} \right) \right) , \qquad (4.4.3)$$

with $i = (1, 2)$. f_1 and f_2 are the curves fitting the radial profile of V_p (normalized to $\langle V_p \rangle \approx 85\ V$ in the OP) at the poloidal positions of the XP and the OP, respectively (see Fig. 4.11). The values of the parameters $(V_{p,i}^{min}, V_{p,i}^{max}, \psi_{p,i}, \Delta\psi_{p,i})$ are listed in Tab. 4.1. The angular term is the

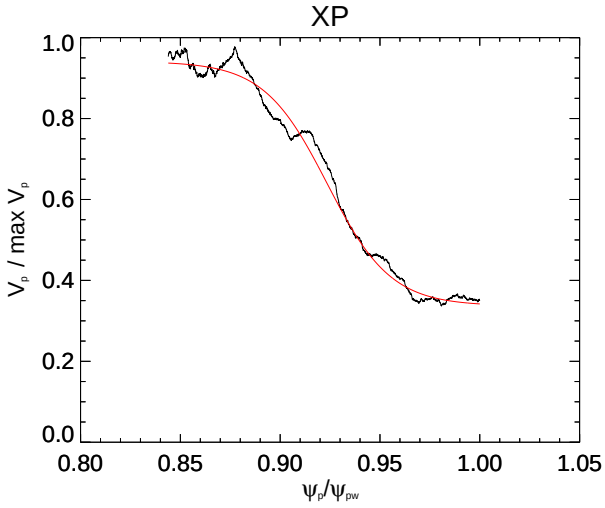

(a)

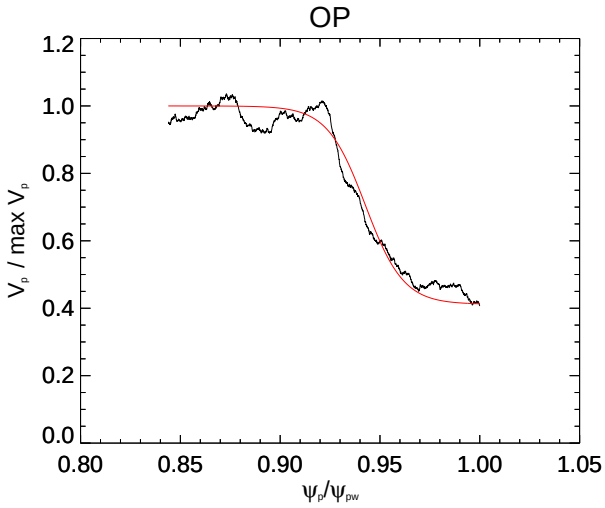

(b)

Figure 4.11: The radial profile of the measured plasma potential at the XP poloidal position (a) and at the OP poloidal position (b). The fit functions f_1 and f_2 (red curves in (a) and (b), respectively).

original sine of the flux function $\psi_h^{(4,1)}$, but with phase $\tilde{\phi}$. In the end, Φ depends on two free variables: Φ_0 and $\tilde{\phi}$. Similarly to what we have done

Table 4.1: Parameter values of the fitting curves f_1 and f_2, normalized to $\langle V_p \rangle \approx 85\ V$.

	XP ($i = 1$)	OP ($i = 2$)
$V_{p,i}^{min}$	0.35	0.41
$V_{p,i}^{max}$	0.94	1.00
$\psi_{p,i}$	0.0145	0.0148
$\Delta\psi_{p,i}$	0.0005	0.0003

for V_p, we map the amplitude of Φ in the (r, θ) plane (see Fig. 4.12) together with the flux surfaces $\psi_h^{(4,1)}$ and magnetic field Poincaré plot. We set $\Phi_0 = 90\ V$ (the maximum amplitude in the measurements) and $\tilde{\phi} = \phi$, i.e. the same phase of $\psi_h^{(4,1)}$. Φ matches the flux surfaces in the region outside the separatrix, while inside does not match them anymore. This behavior was similarly found in results from measurements at RFX-mod [140], and from simulations in Stellarators [52].

The radial electric field E^r is given by differentiating Φ:

$$E^r = \frac{\partial \Phi}{\partial r} = \frac{\partial \psi_p}{\partial r}\frac{\partial \Phi}{\partial \psi_p} = \frac{r}{q}\frac{\partial \Phi}{\partial \psi_p}\ . \tag{4.4.4}$$

The term $\partial\Phi/\partial\psi_p$ is given by

$$\frac{\partial \Phi}{\partial \psi_p} = \Phi_0 \left(f_1' + \frac{1}{2}(f_2' - f_1')\sin(-m\theta + n\zeta + \tilde{\phi}) \right)\ , \tag{4.4.5}$$

where

$$f_i'(\psi_p) = -\frac{1}{2\Delta\psi_{p,i}}(V_{p,i}^{max} - V_{p,i}^{min})\frac{1}{\left[\cosh\left(\frac{\psi_p - \psi_{p,i}}{\Delta\psi_{p,i}}\right)\right]^2}\ . \tag{4.4.6}$$

In Fig. 4.13, we also map the E^r amplitude together with the flux surfaces $\psi_h^{(4,1)}$ and magnetic field Poincaré plot, noting that E^r is modulated both in the radial and in the poloidal directions. In particular, a region of large positive E^r, along the separatrix, can be noticed. This is a confirmation of the well known presence of positive radial electric field at the edge of fusion devices [65, 107, 153]. But, if we focus on this region, we can note also a modulation in the poloidal angle, strictly linked to the magnetic topology, too: E^r has a minimum in between the XP and the OP, and an absolute maximum in correspondence of the XP. On the contrary, right into the OP, E^r almost vanishes, which is consistent with LHD results [66]. Therefore, the potential well is located near the XP, where the electrons are preferably lost,

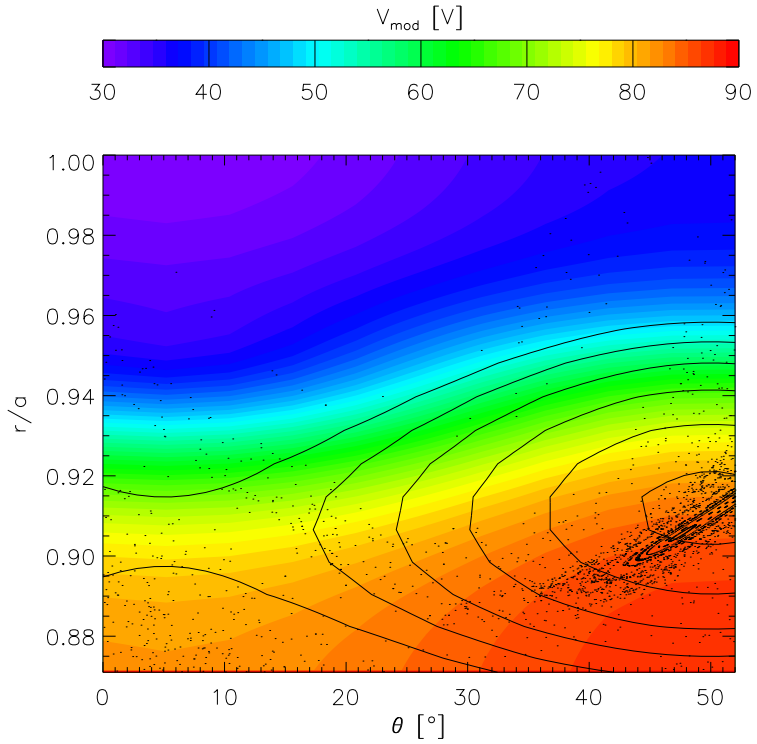

Figure 4.12: Map of the modeled ambipolar potential Φ as a function of the poloidal angle θ and the normalized radius r. Its amplitude is indicated in the color bar. The helical flux surfaces $\psi_h^{(4,1)}$, Eq. (4.3.3), (black lines) and the magnetic field Poincaré plot (black points) are overplotted to the map.

as shown in simulations with 12/4 and 3/1 configurations. This result is in accordance with the plasma potential measurements, discussed in Sec. 4.4.1.

In RFX-mod ORBIT predicts the potential well to stay in proximity of the OP of the main island ($m/n = 0/1$), and measurements show the potential well ($E^r > 0$) near the XP. Despite the apparent agreement with TEXTOR, in RFX the meaning in terms of electron diffusion is just the opposite: $E^r > 0$ is found where D_e is smaller (the XP of the 0/1 mode acts as an electron trap, see Fig. 1.10). The difference between RFX and TEXTOR could be ascribed to a collisional dependence (the case of RFX is highly collisional, contrary to TEXTOR); to a different level of chaos, in RFX compared to TEXTOR; or to a more pronounced plasma-wall interaction (measured particle fluxes to the wall in the RFP are 2 orders of magnitude larger than in tokamaks, being $\sim 10^{20}\ m^{-2}s^{-1}$ [101]).

In order to the test the ambipolarity of Φ, we perform a single electron run, with constant pitch angle $\lambda = 1$, and keeping $\Phi_0 = 90\ V$ and $\tilde{\phi} = \phi$. In

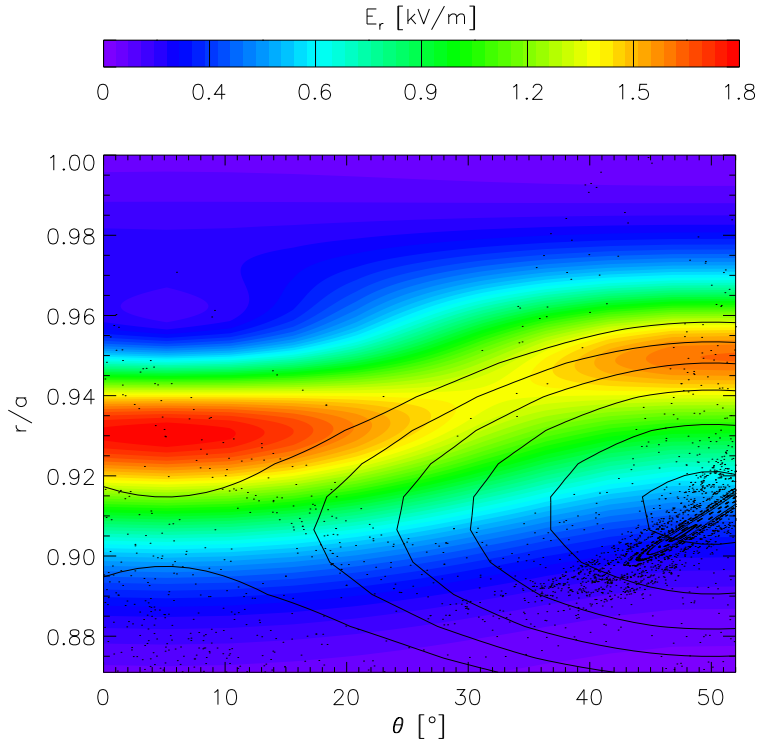

Figure 4.13: Map of the modeled radial electric E^r field as a function of the poloidal angle θ and the normalized radius r. Its amplitude is indicated in the color bar. The helical flux surfaces $\psi_h^{(4,1)}$, Eq. (4.3.3), (black lines) and the magnetic field Poincaré plot (black points) are overplotted to the map.

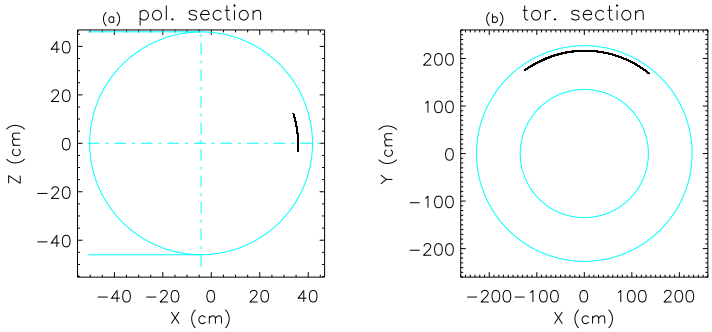

Figure 4.14: Poloidal (a) and toroidal (b) sections of a single electron trajectory. The electron is trapped by the ambipolar potential.

absence of an ambipolar potential the electron with $\lambda = 1$ should be free and complete both the toroidal and poloidal turns. Instead, as it can be seen in Fig. 4.14, if the potential is switched on, the electron is trapped inside the potential structure. A second test would be necessary: the calculation of the electron-root (see Sec. 1.1.2), by evaluating the electron and ion fluxes as a function of Φ_0 and $\tilde{\phi}$ (see Sec. 1.2.4). This is a work in progress.

4.5 Summary and remarks

In this Chapter we analyzed the local radial transport of ions and electrons by means of the evaluation of diffusion coefficients (D_i and D_e, respectively). The evaluation is carried on along a helical path from the OP through the XP of an $m/n = 4/1$ remnant island, created near the LCFS in the DED 3/1 configuration. The result shows that D_i is rather constant along the path, and it is almost neoclassical, while D_e is larger ($0.6 \div 40\ m^2/s$), and is strongly modulated (larger at the XP, lower at the OP), consistently with the $L_\parallel$ maps, shown in Chapter 3. In a local surface right into the OP, $D_e \approx D_i$ and the resulting $E^r \approx 0$.

In the second part of the Chapter, we developed a 3D model for the ambipolar potential Φ on the basis of the geometry of the $m/n = 4/1$ magnetic island and of the measured plasma potential radial profile. We verified the ambipolarity of Φ by showing that a single electron is trapped by the potential structure. A second test, aiming at verifying the balance of electron and ion fluxes, when the ambipolar potential is switched on, is an ongoing work. The radial electric E^r field is derived from Φ. E^r shows large positive value near the 4/1 separatrix, confirming well known results in the RMP tokamak community. Beside this, E^r appears modulated in the poloidal direction, showing a maximum in correspondence of the XP, where the electrons are preferably loss. Right into the OP, $E^r \approx 0$.

Finally, the results are compared with simulations and measurements in TEXTOR and RFX-mod. In TEXTOR, the modeled potential well matches the measurements, and corresponds to the XP of the $m/n = 4/1$ island, consistently with ORBIT transport simulations, that show larger D_e and smaller $L_\parallel$ in that region. In RFX-mod, ORBIT predicts the potential well to stay in proximity of the OP of the main island ($m/n = 0/1$), while measurements show the potential well near the XP: in fact, in RFX-mod $L_\parallel$ is smaller and D_e is larger near the OP of the 0/1 island. The difference between RFX-mod and TEXTOR could be ascribed to a collisional dependence (the case of RFX is highly collisional, contrary to TEXTOR); to a different level of chaos, in RFX compared to TEXTOR; or to a more pronounced plasma-wall interaction (PWI). The result on TEXTOR shows that, apart from strong collisional effects or PWI, ORBIT is capable of correctly describing the electrostatic response to a RMP island.

Chapter 5

Conclusions

In this Thesis the Student has benchmarked the Guiding-Center, Hamiltonian code ORBIT with the volume-preserving, field line tracing code NEMATO: the result is that the topology of islands and chaotic edge of a reversed-field pinch are correctly described by ORBIT. A more quantitative verification has been performed by considering two standard metrics of chaotic systems, such as the field line correlation length and the Lyapunov exponent. The correlation length provided by ORBIT and NEMATO are the same within numerical errors, while a more local metric, such as the Lyapunov exponent, shows a moderate deviation between the two codes. This difference can be ascribed to the numerical scheme (explicit Runge-Kutta in ORBIT, fully implicit in NEMATO). The work on this benchmark has been preparatory to the description of the stochastic edge of the TEXTOR tokamak with ORBIT, in comparison with what has been done in the RFX-mod reversed-field pinch.

The second main part of the Thesis has been the description of the plasma response of electrons and ions to the stochastic edge of TEXTOR, when $m/n = 12/4$ and $3/1$ islands are induced by the resonant magnetic perturbations (RMP) through the dynamic ergodic divertor (DED). This is a fundamental piece of physics, since it shows that, even in presence of static islands, differential radial diffusion of electrons and ions creates an ambipolar E^r field with the same symmetry as the parent island. This result on the one hand extends and reinforces previous work done on $0/1$ and $1/7$ islands in RFX-mod; on the other hand it shows that a positive E^r field arises with RMPs, that retains a poloidal dependence over the angle θ. In this respect, a 3D model of the ambipolar potential $\Phi(\psi_p, \theta, \zeta)$ can be developed with ORBIT, which reproduces in detail measured maps of plasma potential V_p, done in TEXTOR with a sweeping Mirnov probe in the (r, θ) plane. The potential model is able to trap electrons and therefore ensure ambipolarity for the measured potential amplitude. The phase is such that a maximum of E^r is found at the X-point of the $4/1$ island, in corrispondence of the

ergodic fingers, where it is well known that electrons are preferably lost ("pump-out" effect). This result shows that a role of E^r in the "pump-out" mechanism should be included, as well as in theories of ELM suppression.

Appendix A

DED current amplitude and phase

Eq. (3.2.7) in the complex representation is

$$\begin{aligned} I_j &= \sum_{n=-\infty}^{\infty} I_j^{(n)} \iota_n = \frac{I_d}{2i} \sum_{n=-\infty}^{\infty} \iota_n e^{i(n2\pi j/16+\chi_n)} \\ &= \frac{I_d}{2} \sum_{n=-\infty}^{\infty} \iota_n e^{i(n2\pi j/16+\tilde{\chi}_n)} \ , \end{aligned} \tag{A.0.1}$$

where

$$\tilde{\chi}_n = \chi_n - \frac{\pi}{2} \ . \tag{A.0.2}$$

Then, summing on $j = 1, 2, ..., 16$

$$\begin{aligned} \sum_{j=1}^{16} I_j &= \frac{I_d}{2} \sum_{n=-\infty}^{\infty} \iota_n \sum_{j=1}^{16} e^{i(n2\pi j/16+\tilde{\chi}_n)} \\ \sum_{j=1}^{16} I_j e^{-in'2\pi j/16} &= \frac{I_d}{2} \sum_{n=-\infty}^{\infty} \iota_n e^{i\tilde{\chi}_n} \sum_{j=1}^{16} e^{in2\pi j/16} e^{-in'2\pi j/16} = \\ &= \frac{I_d}{2} \sum_{n=-\infty}^{\infty} 16\delta_{nn'} \iota_n e^{i\tilde{\chi}_n} = 8 I_d \iota_{n'} e^{i\tilde{\chi}_{n'}} \ , \end{aligned} \tag{A.0.3}$$

where we used

$$\sum_{j=1}^{N} e^{i(n-n')2\pi j/N} = N\delta_{nn'} \ . \tag{A.0.4}$$

Thus, we obtain the following formula for coefficients and phases:

$$\iota_n e^{i\tilde{\chi}_n} = \frac{1}{8I_d} \sum_{j=1}^{16} I_j e^{-in2\pi j/16} \ . \tag{A.0.5}$$

If we consider the following current distribution

$$I_j = I_d \begin{cases} 1, & \text{for } 1 \leq j \leq 4 \ , \\ 0, & \text{for } 5 \leq j \leq 8 \text{ and } 13 \leq j \leq 16 \ , \\ -1, & \text{for } 9 \leq j \leq 12 \ . \end{cases} \tag{A.0.6}$$

Eq. (A.0.5) is, then,

$$\begin{aligned} \iota_n e^{i\tilde{\chi}_n} &= \frac{1}{8}(x + x^2 + x^3 + x^4 - x^9 - x^{10} - x^{11} - x^{12}) = \\ &= \frac{1}{8}(x + x^2 + x^3 + x^4)(1 - x^8) = \frac{1}{8}x(1 + x^2)(1 - x^8) = \\ &= \frac{1}{8}\frac{x(1 - x^4)(1 - x^8)}{1 - x} \ , \end{aligned} \tag{A.0.7}$$

where

$$\begin{aligned} & x = e^{-in2\pi/16} \ , \\ & 1 - x^8 = 1 - e^{-in\pi} = 1 - (-1)^n \ , \\ & 1 - x^4 = x^2(x^{-2} - x^2) = 2ie^{-in\pi/4}\sin(n\pi/4) \ , \\ & 1 - x = x^{1/2}(x^{-1/2} - x^{1/2}) = 2ie^{-in\pi/16}\sin(n\pi/16) \ . \end{aligned}$$

Thus

$$\begin{aligned} \iota_n e^{i\tilde{\chi}_n} &= \frac{1}{8}\frac{e^{-in2\pi/16}2ie^{-in\pi/4}\sin(n\pi/4)[1 - (-1)^n]}{2ie^{-in\pi/16}\sin(n\pi/16)} = \\ &= \frac{1}{8}[1 - (-1)^n]\frac{\sin(n\pi/4)}{\sin(n\pi/16)}e^{-in5\pi/16} \ . \end{aligned} \tag{A.0.8}$$

In particular, for $n = 1$, we find the coefficient and phase reported in (3.2.8):

$$\begin{aligned} \iota_1 &= \frac{\sin(n\pi/4)}{4\sin(n\pi/16)} \ , \\ \chi_1 &= \tilde{\chi}_1 + \frac{\pi}{2} = \frac{5\pi}{16} - \frac{\pi}{2} = \frac{3\pi}{16} \ . \end{aligned} \tag{A.0.9}$$

Appendix B

Continuous current density

Eq. (3.2.11) can be written as

$$J^{(n)}(r,\theta,\varphi) = A \sum_{j=-\infty}^{\infty} \sin\left(n\frac{2\pi j}{16} + \chi_n\right) \delta(\theta - \theta_\varphi + j\delta\theta) \,, \tag{B.0.1}$$

where $A = \delta(r - r_c)g(\theta,\varphi)(I_d)/(r_c)$ and we substituted

$$\theta_j = \theta_{01} - (j-1)\delta\theta - \theta_c/\pi \;\varphi = \theta_\varphi - j\delta\theta \,.$$

θ_{01} is the poloidal angle of the first coil at the toroidal angle $\varphi = 0$ and . Then, using the Dirac function representation

$$\delta(x) = \frac{1}{2\pi}\int_{-\infty}^{\infty} \mathrm{d}p \; e^{ixp} \tag{B.0.2}$$

and writing $\sin(x) = \mathrm{Im}\{\exp(ix)\}$, Eq. (B.0.1) becomes

$$\begin{aligned} J^{(n)}(r,\theta,\varphi) =& \frac{A}{2\pi}\mathrm{Im}\Bigg\{ e^{i\chi_n} \int_{-\infty}^{\infty} \mathrm{d}p \; e^{i(\theta-\theta_\varphi)p} \\ & \sum_{j=-\infty}^{\infty} \exp\left[i\left(\frac{2\pi n}{16} + p\delta\theta\right) j\right]\Bigg\} \,. \end{aligned} \tag{B.0.3}$$

and using the Poisson rule

$$\sum_{j=-\infty}^{\infty} e^{i2\pi jx} = \sum_{s=-\infty}^{\infty} \delta(s-x) \,,$$

we obtain

$$\begin{aligned} J^{(n)}(r,\theta,\varphi) =& \frac{A}{2\pi}\mathrm{Im}\Bigg\{ e^{i\chi_n} \int_{-\infty}^{\infty} \mathrm{d}p \; e^{i(\theta-\theta_\varphi)p} \\ & \sum_{s=-\infty}^{\infty} \delta\left(s - \frac{n}{16} - p\frac{\delta\theta}{2\pi}\right)\Bigg\} \,. \end{aligned} \tag{B.0.4}$$

Since $\delta(ax) = \delta(x)/|a|$ and

$$\int_{-\infty}^{\infty} \mathrm{d}x\ f(x)\delta(x-a) = f(a)\ ,$$

$J^{(n)}$ can be written as

$$\begin{aligned} J^{(n)}(r,\theta,\varphi) &= \frac{A}{\delta\theta}\mathrm{Im}\left\{ e^{i\chi_n} \sum_{s=-\infty}^{\infty} \exp\left[i2\pi\left(s-\frac{n}{16}\right)(\theta-\theta_\varphi)/\delta\theta\right]\right\} \\ &= \delta(r-r_c)g(\theta,\varphi)\frac{I_d}{r_c\delta\theta} \\ &\quad \sum_{s=-\infty}^{\infty} \sin\left(\frac{2\pi(s-n/16)}{\delta\theta}(\theta-\theta_\varphi)+\chi_n\right)\ . \end{aligned} \tag{B.0.5}$$

Hence, using $\theta_\varphi = \theta_{01} + \delta\theta - \theta_c/\pi\ \varphi$ and changing the sine to cosine, we get Eq. (3.2.13):

$$\begin{aligned} J^{(n)}(r,\theta,\varphi) =& \delta(r-r_c)g(\theta,\varphi)\frac{I_d}{r_c\delta\theta}\sum_{s=-\infty}^{\infty}\cos\Bigg(\frac{\pi}{2\delta\theta}\frac{(16s-n)}{4}\theta + \\ &+\frac{\theta_c}{2\delta\theta}\frac{(16s-n)}{4}\varphi+\chi_n-\frac{\pi}{2\delta\theta}\frac{(16s-n)}{4}\theta_0-\frac{\pi}{2}\Bigg)\ . \end{aligned} \tag{B.0.6}$$

Appendix C

Nonideal coil configuration

Consider the integral

$$f_{\bar{m}\bar{n}} = \frac{1}{(2\pi)^2}\int_0^{2\pi}\int_0^{2\pi} \mathrm{d}\theta\mathrm{d}\varphi\; g(\theta,\varphi)e^{-i\bar{m}\theta - i\bar{n}\varphi}\;, \tag{C.0.1}$$

using the definition of $g(\theta,\varphi)$ (3.2.12) the integral with respect to θ can be reduced:

$$\begin{aligned}
&\int_0^{2\pi} \mathrm{d}\theta\; g(\theta,\varphi)e^{-i\bar{m}\theta} = \int_{\pi-\theta_c(\varphi)}^{\pi+\theta_c(\varphi)} \mathrm{d}\theta\; e^{-i\bar{m}\theta} = \\
&= \frac{i}{\bar{m}}\left\{e^{-i\bar{m}(\pi+\theta_c(\varphi))} - e^{-i\bar{m}(\pi-\theta_c(\varphi))}\right\} = \\
&= \frac{ie^{-i\bar{m}\pi}}{\bar{m}}\left\{e^{-i\bar{m}\theta_c(\varphi)} - e^{i\bar{m}\theta_c(\varphi)}\right\}\;.
\end{aligned} \tag{C.0.2}$$

Then, Eq. (C.0.1) becomes

$$f_{\bar{m}\bar{n}} = \frac{1}{(2\pi)^2}\frac{ie^{-i\bar{m}\pi}}{\bar{m}}\int_0^{2\pi} \mathrm{d}\varphi\; e^{-i\bar{n}\varphi}\left\{e^{-i\bar{m}\theta_c(\varphi)} - e^{i\bar{m}\theta_c(\varphi)}\right\}\;. \tag{C.0.3}$$

Now, let us solve the integral:

$$\int_0^{2\pi} \mathrm{d}\varphi\; e^{-i\bar{n}\varphi}e^{\mp i\bar{m}\theta_c(\varphi)}\;. \tag{C.0.4}$$

Since $\theta_c(\varphi)$ is periodic in φ with period $\pi/2$, integral (C.0.4) can be written as

$$4\int_{\varphi_c-\pi/2}^{\varphi_c} \mathrm{d}\varphi\; e^{-i\bar{n}\varphi}e^{\pm i\bar{m}\theta_c(\varphi)}\;. \tag{C.0.5}$$

If we explicate $\theta_c(\varphi)$ using (3.2.12) and name $\alpha = 2\Delta\theta/\pi$, integral (C.0.5) can be developed as follow:

$$\begin{aligned}
&4\int_{\varphi_c-\pi/2}^{\varphi_c} \mathrm{d}\varphi\; e^{-i\bar{n}\varphi} e^{\pm i\bar{m}\left[\theta_{c0}-\alpha\left(\varphi-\varphi_c+\frac{\pi}{2}\right)\right]} = \\
&= 4e^{\pm i\bar{m}\left[\theta_{c0}-\alpha\left(-\varphi_c+\frac{\pi}{2}\right)\right]} \int_{\varphi_c-\pi/2}^{\varphi_c} \mathrm{d}\varphi\; e^{-i(\bar{n}\pm\alpha\bar{m})\varphi} = \\
&= 4e^{\pm i\bar{m}\left[\theta_{c0}-\alpha\left(-\varphi_c+\frac{\pi}{2}\right)\right]} \frac{1}{-i(\bar{n}\pm\alpha\bar{m})} \\
&\quad \left\{ e^{-i(\bar{n}\pm\alpha\bar{m})\varphi_c} - e^{-i(\bar{n}\pm\alpha\bar{m})(\varphi_c-\pi/2)} \right\} = \\
&= 8e^{\pm i\bar{m}\left[\theta_{c0}-\alpha\left(-\varphi_c+\frac{\pi}{2}\right)\right]} e^{-i(\bar{n}\pm\alpha\bar{m})\left(\varphi_c-\frac{\pi}{4}\right)} \\
&\quad \frac{1}{\bar{n}\pm\alpha\bar{m}} \frac{1}{2i} \left\{ e^{i(\bar{n}\pm\alpha\bar{m})\pi/4} - e^{-i(\bar{n}\pm\alpha\bar{m})\pi/4} \right\} = \\
&= 8e^{\pm i\bar{m}(\theta_{c0}-\Delta\theta/2)} e^{-i\bar{n}\left(\varphi_c-\frac{\pi}{4}\right)} \frac{\sin[(\bar{n}\pm\alpha\bar{m})\pi/4]}{\bar{n}\pm\alpha\bar{m}} \,.
\end{aligned} \tag{C.0.6}$$

Finally, introducing the notation $\theta_c = \theta_{c0} - \Delta\theta/2$, f_{mn} (C.0.3) becomes

$$f_{\bar{m}\bar{n}} = e^{-i\bar{m}\pi} e^{-i\bar{n}\varphi_c} \frac{2\sin(\alpha\bar{m}\pi/4)}{\pi^2\bar{m}} \frac{2[in\cos(\bar{m}\theta_c) + \bar{m}\alpha\sin(\bar{m}\theta_c)]}{\bar{n}^2 - (\alpha\bar{m})^2} \,. \tag{C.0.7}$$

According to Eq. (3.2.18) the expression for the Fourier coefficients of the current density $\tilde{J}_{mn}(r)$ is

$$\tilde{J}_{mn}(r) = \delta(r-r_c)\iota^{(n)} J_d f_{m-nm_0/4,\hat{n}-nn_0/4} \,. \tag{C.0.8}$$

The main contribution to the toroidal spectrum $\hat{n}$ comes from the terms $\hat{n} = n$ $(s = 0)$

$$f_{\bar{m}0} = e^{-i\bar{m}\pi} \frac{\sin(\alpha\bar{m}\pi/4)}{\alpha\bar{m}\pi/4} \frac{\sin(\bar{m}\theta_c)}{\bar{m}\pi} \,. \tag{C.0.9}$$

Substituting $f_{\bar{m}0}$ in Eq. (3.2.18) and replacing $\bar{m} = -m - nm_0/4$ we obtain

$$\begin{aligned}
\tilde{J}_{mn}(r) &= \delta(r-r_c) J_d e^{-i(-m-nm_0/4)\pi} \\
&\quad \frac{\sin[(-m-nm_0/4)\theta_c]}{(-m-nm_0/4)\pi} \\
&\quad \frac{\sin[\pi(-m-nm_0/4)\alpha/4]}{\pi(-m-nm_0/4)\alpha/4} = \\
&= \delta(r-r_c) J_d e^{inm_0/4)\pi} \\
&\quad (-1)^m \frac{\sin[(-m-nm_0/4)\theta_c]}{(-m-nm_0/4)\pi} = \\
&\quad \frac{\sin[\pi(-m-nm_0/4)\Delta/2]}{\pi(-m-nm_0/4)\Delta/2} = \\
&= \delta(r-r_c) J_d e^{i\pi nm_0/4} g_{mn} C_{mn} \,,
\end{aligned} \tag{C.0.10}$$

where

$$g_{mn} = \quad (-1)^m \frac{\sin[(-m - nm_0/4)\theta_c]}{(-m - nm_0/4)\pi} \tag{C.0.11}$$

and

$$C_{mn} = \frac{\sin[\pi(-m - nm_0/4)\Delta/2]}{\pi(-m - nm_0/4)\Delta/2} \ . \tag{C.0.12}$$

We include the factor $\exp(i\pi n m_0/4)$ in the phase χ_{mn} that becomes

$$\chi_{mn} = -\chi_0^{(n)} + \frac{\pi n m_0}{4} = -\chi_n + \frac{m_0 n}{4}(\pi - \theta_0) + \frac{\pi}{2} \ . \tag{C.0.13}$$

Appendix D

Scalar potential

Naming $z = nr_/R_c$ and $z_c = nr_c/R_c$, the first boundary condition of (3.2.26) is

$$a^i I'_m(z_c) - a^e K'_m(z_c) = 0 \ , \tag{D.0.1}$$

from which we obtain

$$a^e = a^i \frac{I'_m(z_c)}{K'_m(z_c)} \ . \tag{D.0.2}$$

The second boundary condition of (3.2.26) is

$$\begin{aligned} &- m(a^i I_m(z_c) - a^e K_m(z_c)) = \mu_0 J_{mn} r_c \cos\alpha_0 \ , \\ &- \frac{m a^i}{K'_m(z_c)} (I_m(z_c) K'_m(z_c) - I'_m(z_c) K_m(z_c)) = \mu_0 J_{mn} r_c \cos\alpha_0 \ , \end{aligned} \tag{D.0.3}$$

where we used (D.0.2). We recall, now, the modified Bessel functions have the following asymptotic terms at $r > r_c$:

$$\begin{aligned} I_m(z) &\approx \frac{1}{\Gamma(m+1)} \left(\frac{z}{2}\right)^m \ , \\ K_m(z) &\approx \frac{\Gamma(m)}{2} \left(\frac{z}{2}\right)^{-m} \ , \\ I'_m(z) &\approx \frac{m}{2\Gamma(m+1)} \left(\frac{z}{2}\right)^{m-1} \ , \\ K'_m(z) &\approx -\frac{m\Gamma(m)}{4} \left(\frac{z}{2}\right)^{-m-1} \ , \\ I_m(z) K'_m(z) - I'_m(z) K_m(z) &\approx -\frac{1}{z} \ , \\ I_m(z) K'_m(z_c) &\approx -\frac{1}{2z_c} \left(\frac{z}{z_c}\right)^m \ , \\ \Gamma(m+1) &= m\Gamma(m) \ . \end{aligned} \tag{D.0.4}$$

Hence, using (D.0.4) in Eq. (D.0.3) we get

$$a^i = -\mu_0 J_{mn} \cos\alpha_0 \frac{r_c}{m} z_0 K'_m(z_c) \ . \tag{D.0.5}$$

The scalar potential radial component $\Phi_{mn}(r)$ is

$$\begin{aligned}\Phi_{mn}(r) = a^i I_m(z) = -\mu_0 J_{mn} \cos\alpha_0 \frac{r_c}{m} z_c K'_m(z_c) I_m(z) = \\ = \mu_0 J_{mn} \cos\alpha_0 \frac{r_c}{2m} \left(\frac{z}{z_c}\right)^m = \\ = \mu_0 J_{mn} \cos\alpha_0 \frac{r_c}{2m} \left(\frac{r}{r_c}\right)^m \ .\end{aligned} \tag{D.0.6}$$

Bibliography

[1] S. S. Abdullaev, A. Wingen, and K. H. Spatschek. Mapping of drift surfaces in toroidal systems with chaotic magnetic fields. *Physics of Plasmas*, 13(4):042509, 2006.

[2] Sadrilla Abdullaev. *Magnetic Stochasticity in Magnetically Confined Fusion Plasmas*, volume 78 of *Springer Series on Atomic, Optical, and Plasma Physics*. Springer Cham Heidelberg New York Dordrecht London, 2013.

[3] M. Agostini, R. Cavazzana, P. Scarin, and G. Serianni. Operation of the gas-puff imaging diagnostic in the RFX-mod device. *Rev. Sci. Instrum.*, 77(10):10E513, 2006. Papers from the 16th Topical Conference on High Temperature Plasma Diagnostics.

[4] M Agostini, A Scaggion, P Scarin, G Spizzo, and N Vianello. Interplay between edge magnetic topology, pressure profile and blobs in the edge of rfx-mod. *Plasma Physics and Controlled Fusion*, 54(6):065003, 2012.

[5] M Agostini, P Scarin, R Cavazzana, F Sattin, G Serianni, M Spolaore, and N Vianello. Edge turbulence characterization in rfx-mod with optical diagnostics. *Plasma Physics and Controlled Fusion*, 51(10):105003, 2009.

[6] J. K. Anderson, J. Adney, A. Almagri, A. Blair, D. L. Brower, M. Cengher, B. E. Chapman, S. Choi, D. Craig, D. R. Demers, D. J. Den Hartog, B. Deng, W. X. Ding, F. Ebrahimi, D. Ennis, G. Fiksel, C. B. Forest, P. Franz, J. Goetz R. W. Harvey, D. Holly, B. Hudson, M. Kaufman, T. Lovell, L. Marrelli, P. Martin, K. McCollam, V. V. Mirnov, P. Nonn, R. O'Connell, S. Oliva, P. Piovesan, S. C. Prager, I. Predebon, J. S. Sarff, G. Spizzo, V. Svidzinski, M. Thomas, and M. D. Wyman. Dynamo-free plasma in the reversed-field pinch: Advances in understanding the reversed-field pinch improved confinement mode. *Phys. Plasmas*, 12:056118, 2005.

[7] E Aurell, G Boffetta, A Crisanti, G Paladin, and A Vulpiani. Predictability in the large: an extension of the concept of lyapunov exponent. *Journal of Physics A: Mathematical and General*, 30(1):1, 1997.

[8] Marco Barp, Roberto Cavazzana, Giuseppe Marchiori, Anton Soppelsa, and Loris Zanotto. Closed loop control of reversal parameter in rfx-mod. *Fusion Engineering and Design*, 86(6–8):1000–1004, 2011. Proceedings of the 26th Symposium of Fusion Technology (SOFT-26), Porto, Portugal 27 September–1 October 2010.

[9] Rosario Bartiromo. Plasma rotation and finite larmor radius losses in a reversed field pinch. *Physics of Plasmas*, 5(9):3342–3349, 1998.

[10] M. Bécoulet, G. Huysmans, X. Garbet, E. Nardon, D. Howell, A. Garofalo, M. Schaffer, T. Evans, K. Shaing, A. Cole, J.-K. Park, and P. Cahyna. Physics of penetration of resonant magnetic perturbations used for type i edge localized modes suppression in tokamaks. *Nuclear Fusion*, 49(8):085011, 2009.

[11] T. M. Biewer, C. B. Forest, J. K. Anderson, G. Fiksel, B. Hudson, S. C. Prager, J. S. Sarff, J. C. Wright, D. L. Brower, W. X. Ding, and S. D. Terry. Electron heat transport measured in a stochastic magnetic field. *Phys. Rev. Lett.*, 91:045004, Jul 2003.

[12] D. Biskamp. *Nonlinear Magnetohydrodynamics*, volume 263, pages 375–376. Cambridge University Press, The Pitt Building, Trumpington Street, Cambridge CB2 1RP, 1994.

[13] H.A.B. Bodin. The reversed field pinch. *Nuclear Fusion*, 30(9):1717, 1990.

[14] D Bonfiglio, M Veranda, S Cappello, L Chacón, and G Spizzo. Magnetic chaos healing in the helical reversed-field pinch: indications from the volume-preserving field line tracing code nemato. *Journal of Physics: Conference Series*, 260(1):012003, 2010.

[15] Allen H. Boozer. Plasma equilibrium with rational magnetic surfaces. *Physics of Fluids*, 24(11):1999–2003, 1981.

[16] Allen H. Boozer and Gioietta Kuo-Petravic. Monte carlo evaluation of transport coefficients. *Physics of Fluids*, 24(5):851–859, 1981.

[17] S. I. Braginskii. Transport Processes in a Plasma. In *Reviews of Plasma Physics*, volume 1, page 227. Consultants Bureau, New York, 1965.

[18] S. Cappello and D. Biskamp. Reconnection processes and scaling laws in reversed field pinch magnetohydrodynamics. *Nuclear Fusion*, 36(5):571, 1996.

[19] S. Cappello, D. Bonfiglio, and D. F. Escande. Magnetohydrodynamic dynamo in reversed field pinch plasmas: Electrostatic drift nature of the dynamo velocity field. *Physics of Plasmas*, 13(5):056102, 2006.

[20] S. Cappello, D. Bonfiglio, D. F. Escande, S. C. Guo, A. Alfier, and R. Lorenzini. The reversed field pinch toward magnetic order: a genuine self-organization. volume 1069, pages 27–39. AIP, 2008.

[21] L. Carraro, M.E. Puiatti, F. Sattin, P. Scarin, M. Spolaore, M. Valisa, B. Zaniol, and P. Zanca. Plasma-wall interactions and radial electric fields in the reversed field pinch RFX. *Journal of Nuclear Materials*, 313–316:976–979, 2003. Proc. 15th Int. Conf. on Plasma-Surface Interactions in Controlled Fusion Devices (PSI-15), Gifu, Japan, May 2002.

[22] Boris V. Chirikov. A universal instability of many-dimensional oscillator systems. *Physics Reports*, 52(5):263 – 379, 1979.

[23] S. Choi, D. Craig, F. Ebrahimi, and S. C. Prager. Cause of sudden magnetic reconnection in a laboratory plasma. *Phys. Rev. Lett.*, 96:145004, Apr 2006.

[24] G. Ciaccio, M. Veranda, D. Bonfiglio, S. Cappello, G. Spizzo, L. Chacon, and R. B. White. Numerical verification of orbit and nemato codes for magnetic topology diagnosis. *Physics of Plasmas*, 20(6):062505, 2013.

[25] J W Coenen, B Schweer, M Clever, S Freutel, O Schmitz, H Stoschus, U Samm, and B Unterberg. Charge exchange recombination spectroscopy on a diagnostic hydrogen beamer measuring impurity rotation and radial electric field at the tokamak textor. *Journal of Physics B: Atomic, Molecular and Optical Physics*, 43(14):144015, 2010.

[26] J.W. Coenen, O. Schmitz, B. Unterberg, M. Clever, M.A. Jakubowski, U. Samm, B. Schweer, H. Stoschus, M. Tokar, and the TEXTOR-Team. Rotation and radial electric field in the plasma edge with resonant magnetic perturbation at textor. *Nuclear Fusion*, 51(6):063030, 2011.

[27] A. Cravotta, G. Spizzo, D. Terranova, T. Bolzonella, P. Franz, L. Marrelli, P. Martin, S. Martini, and S. Ortolani. A statistical analysis of pulsed poloidal current drive in the reversed field experiment. *Physics of Plasmas*, 10(3):705–712, 2003.

[28] F. D'Angelo and R. Paccagnella. The stochastic diffusion process in reversed-field pinch. *Physics of Plasmas*, 3(6):2353–2364, 1996.

[29] G. De Masi, E. Martines, F. Auriemma, R. Cavazzana, B. Momo, C. Rea, S. Spagnolo, G. Spizzo, M. Spolaore, N. Vianello, and M. Zuin. The role of the magnetic topology in the Reversed Field Pinch edge physics. In V. Naulin, C. Angioni, M. Borghesi, S. Ratynskaia, S. Poedts, and T. Donné, editors, *Proc. 40th EPS Conference on Plasma Physics*, volume 37D, page O2.105, Helsinki, Finland, 1–5 July 2013. European Physical Society (Petit Lancy).

[30] G. De Masi, E. Martines, M. Spolaore, N. Vianello, R. Cavazzana, P. Innocente, B. Momo, S. Spagnolo, and M. Zuin. Electrostatic properties and active magnetic topology modification in the rfx-mod edge plasma. *Nuclear Fusion*, 53(8):083026, 2013.

[31] D. del Castillo-Negrete and L. Chacón. Local and nonlocal parallel heat transport in general magnetic fields. *Phys. Rev. Lett.*, 106:195004, 2011.

[32] Diego del Castillo-Negrete and P. J. Morrison. Chaotic transport by rossby waves in shear flow. *Physics of Fluids A: Fluid Dynamics*, 5(4):948–965, 1993.

[33] D. J. Den Hartog, J. T. Chapman, D. Craig, G. Fiksel, P. W. Fontana, S. C. Prager, and J. S. Sarff. Measurement of core velocity fluctuations and the dynamo in a reversed-field pinch. *Physics of Plasmas (1994-present)*, 6(5):1813–1821, 1999.

[34] R. N. Dexter, D. W. Kerst, T. W. Lovell, S. C. Prager, and J. C. Sprott. The Madison Symmetric Torus. *Fusion Technol.*, 19:131, 1991.

[35] T. Eich, D. Reiser, and K.H. Finken. Two dimensional modelling approach to transport properties of the textor-ded laminar zone. *Nuclear Fusion*, 40(10):1757, 2000.

[36] D. F. Escande, P. Martin, S. Ortolani, A. Buffa, P. Franz, L. Marrelli, E. Martines, G. Spizzo, S. Cappello, A. Murari, R. Pasqualotto, and P. Zanca. Quasi-single-helicity reversed-field-pinch plasmas. *Phys. Rev. Lett.*, 85:1662–1665, Aug 2000.

[37] D. F. Escande, R. Paccagnella, S. Cappello, F. D'Angelo, and C. Marchetto. Chaos Healing by Separatrix Disappearance and Quasisingle Helicity States of the Reversed Field Pinch. *Phys. Rev. Lett.*, 85 (15):3169, 2000.

[38] T. E. Evans, R. A. Moyer, P. R. Thomas, J. G. Watkins, T. H. Osborne, J. A. Boedo, E. J. Doyle, M. E. Fenstermacher, K. H. Finken, R. J. Groebner, M. Groth, J. H. Harris, R. J. La Haye, C. J. Lasnier, S. Masuzaki, N. Ohyabu, D. G. Pretty, T. L. Rhodes, H. Reimerdes, D. L. Rudakov, M. J. Schaffer, G. Wang, and L. Zeng. Suppression of large edge-localized modes in high-confinement diii-d plasmas with a stochastic magnetic boundary. *Phys. Rev. Lett.*, 92:235003, Jun 2004.

[39] T.E. Evans, M.E. Fenstermacher, R.A. Moyer, T.H. Osborne, J.G. Watkins, P. Gohil, I. Joseph, M.J. Schaffer, L.R. Baylor, M. Bécoulet, J.A. Boedo, K.H. Burrell, J.S. deGrassie, K.H. Finken, T. Jernigan, M.W. Jakubowski, C.J. Lasnier, M. Lehnen, A.W. Leonard, J. Lonnroth, E. Nardon, V. Parail, O. Schmitz, B. Unterberg, and W.P. West. Rmp elm suppression in diii-d plasmas with iter similar shapes and collisionalities. *Nuclear Fusion*, 48(2):024002, 2008.

[40] Todd E. Evans, Richard A. Moyer, Keith H. Burrell, Max E. Fenstermacher, Ilon Joseph, Anthony W. Leonard, Thomas H. Osborne, Gary D. Porter, Michael J. Schaffer, Philip B. Snyder, Paul R. Thomas, Jonathan G. Watkins, and William P. West. Edge stability and transport control with resonant magnetic perturbations in collisionless tokamak plasmas. *Nature Phys.*, 2:419–423, 2006.

[41] Y Feng, M Kobayashi, T Lunt, and D Reiter. Comparison between stellarator and tokamak divertor transport. *Plasma Physics and Controlled Fusion*, 53(2):024009, 2011.

[42] Y. Feng, M. Kobayashi, T. Morisaki, S. Masuzaki, J. Miyazawa, B.J. Peterson, S. Morita, M. Shoji, K. Ida, I. Yamada, K. Narihara, N. Ashikawa, H. Yamada, N. Ohyabu, A. Komori, O. Motojima, F. Sardei, D. Reiter, and the LHD Experimental Group. Fluid features of the stochastic layer transport in lhd. *Nuclear Fusion*, 48(2):024012, 2008.

[43] G. Fiksel, B. Hudson, D. J. Den Hartog, R. M. Magee, R. O'Connell, S. C. Prager, A. D. Beklemishev, V. I. Davydenko, A. A. Ivanov, and Yu. A. Tsidulko. Observation of weak impact of a stochastic magnetic field on fast-ion confinement. *Phys. Rev. Lett.*, 95:125001, Sep 2005.

[44] K H Finken, S S Abdullaev, W Biel, M F M de Bock, C Busch, E Farshi, M von Hellermann, G M D Hogeweij, M Jakubowski, R Jaspers, H R Koslowski, A Kraemer-Flecken, A Lazaros, M Lehnen, Y Liang, A Nicolai, O Schmitz, B Unterberg, E Westerhof, R Wolf, O Zimmermann, M de Baar, G Bertschinger, S Brezinsek, I G J Classen, A J H Donné, H G Esser, H Gerhauser, B Giesen, D Harting, J A Hoekzema, P W Huettemann, S Jachmich, K Jakubowska,

D Kalupin, F Kelly, Y Kikuchi, A Kirschner, R Koch, M Korten, A Kreter, J Krom, U Kruezi, A Litnovsky, X Loozen, N J Lopes Cardozo, A Lyssoivan, O Marchuk, Ph Mertens, A Messiaen, O Neubauer, V Philipps, A Pospieszczyk, D Reiser, D Reiter, A L Rogister, T Van Rompuy, A Savtchkov, U Samm, R P Schorn, F C Schueller, B Schweer, G Sergienko, K H G Telesca, M Tokar, G Van Oost, R Uhlemann, G Van Wassenhove, R Weynants, S Wiesen, and Y Xu. The dynamic ergodic divertor in the textor tokamak: plasma response to dynamic helical magnetic field perturbations. *Plasma Physics and Controlled Fusion*, 46(12B):B143, 2004.

[45] K. H. Finken et al. *The Structure of Magnetic Field in the TEXTOR-DED*, volume 45 of *Schriften des Forschungszentrums Jülich. Reihe Energietechnik / energy technology*. Jülich : Forschungszentrum, Zentralbibliothek, 2005.

[46] K.H. Finken, S.S. Abdullaev, A. Kaleck, and G.H. Wolf. Operating space of the dynamic ergodic divertor for textor-94. *Nuclear Fusion*, 39(5):637, 1999.

[47] John M. Finn and Luis Chacón. Volume preserving integrators for solenoidal fields on a grid. *Physics of Plasmas*, 12(5):054503, 2005.

[48] John M. Finn, Rick Nebel, and Charles Bathke. Single and multiple helicity ohmic states in reversed-field pinches. *Physics of Fluids B: Plasma Physics*, 4(5):1262–1279, 1992.

[49] M.-C. Firpo and D. Constantinescu. Study of the interplay between magnetic shear and resonances using hamiltonian models for the magnetic field lines. *Physics of Plasmas*, 18(3):032506, 2011.

[50] P. Franz, L. Marrelli, P. Piovesan, B. E. Chapman, P. Martin, I. Predebon, G. Spizzo, R. B. White, and C. Xiao. Observations of multiple magnetic islands in the core of a reversed field pinch. *Phys. Rev. Lett.*, 92:125001, Mar 2004.

[51] H. Frerichs, D. Reiter, O. Schmitz, T.E. Evans, and Y. Feng. Three-dimensional edge transport simulations for diii-d plasmas with resonant magnetic perturbations. *Nuclear Fusion*, 50(3):034004, 2010.

[52] J M García-Regaña, R Kleiber, C D Beidler, Y Turkin, H Maaßberg, and P Helander. On neoclassical impurity transport in stellarator geometry. *Plasma Physics and Controlled Fusion*, 55(7):074008, 2013.

[53] D. A. Gates and L. Delgado-Aparicio. Origin of tokamak density limit scalings. *Phys. Rev. Lett.*, 108:165004, Apr 2012.

[54] P. Ghendrih, M. Bécoulet, L. Costanzo, Y. Corre, C. Grisolia, A. Grosman, R. Guirlet, J.P. Gunn, T. Loarer, P. Monier-Garbet, P.R. Thomas, M. Zabiégo, J. Bucalossi, P. Devynck, G. Martin, C. De Michelis, F. Nguyen, B. Pégourié, R. Reichle, F. Saint-Laurent, J.-C. Vallet, and Tore Supra Team. Ergodic divertor experiments on the route to steady state operation of tore supra. *Nuclear Fusion*, 41(10):1401, 2001.

[55] F Gnesotto, P Sonato, W.R Baker, A Doria, F Elio, M Fauri, P Fiorentin, G Marchiori, and G Zollino. The plasma system of RFX. *Fusion Engineering and Design*, 25(4):335–372, 1995.

[56] M. Gobbin, D. Bonfiglio, D. F. Escande, A. Fassina, L. Marrelli, A. Alfier, E. Martines, B. Momo, and D. Terranova. Vanishing magnetic shear and electron transport barriers in the rfx-mod reversed field pinch. *Phys. Rev. Lett.*, 106:025001, Jan 2011.

[57] M. Gobbin, L. Marrelli, P. Martin, and R. B. White. Ion and electron local transport inside single helicity islands in the reversed field pinch. *Physics of Plasmas*, 14(7):072305, 2007.

[58] M Gobbin, L Marrelli, and R B White. Numerical studies of transport mechanisms in RFX-mod low magnetic chaos regimes. *Plasma Physics and Controlled Fusion*, 51(6):065010 (14pp), 2009.

[59] M. Gobbin, G. Spizzo, L. Marrelli, and R. B. White. Neoclassical transport in the helical reversed-field pinch. *Phys. Rev. Lett.*, 105:195006, Nov 2010.

[60] M. Gobbin, R.B. White, L. Marrelli, and P. Martin. Resonance between passing fast ions and mhd instabilities both in the tokamak and the rfp configurations. *Nuclear Fusion*, 48(7):075002, 2008.

[61] Herbert Goldstein. *Classical mechanics*, pages 392–393. Addison-Wesley, Reading, Massachussets, second edition, 1980.

[62] Herbert Goldstein. *Classical mechanics*, page 563. Addison-Wesley, Reading, Massachussets, second edition, 1980.

[63] Martin Greenwald. Density limits in toroidal plasmas. *Plasma Physics and Controlled Fusion*, 44(8):R27–R53, 2002.

[64] A. Grosman, J.-M. Ané, P. Barabaschi, K.H. Finken, A. Mahdavi, Ph. Ghendrih, G. Huysmans, M. Lipa, P.R. Thomas, and E. Tsitrone. H-mode barrier control with external magnetic perturbations. *Journal of Nuclear Materials*, 313-316(0):1314 – 1320, 2003. Plasma-Surface Interactions in Controlled Fusion Devices 15.

[65] W R Hess, C DeMichelis, M Mattioli, F Clairet, M Druetta, A Grosman, R Guirlet, T Hutter, J Lasalle, and P Monier-Garbet. Experimental study of ergodic edge plasmas with marfes in tore supra. *Plasma Physics and Controlled Fusion*, 37(9):951, 1995.

[66] K. Ida, N. Ohyabu, T. Morisaki, Y. Nagayama, S. Inagaki, K. Itoh, Y. Liang, K. Narihara, A. Yu. Kostrioukov, B. J. Peterson, K. Tanaka, T. Tokuzawa, K. Kawahata, H. Suzuki, and A. Komori. Observation of plasma flow at the magnetic island in the large helical device. *Phys. Rev. Lett.*, 88:015002, Dec 2001.

[67] K. Kamiya, K. Ida, M. Yoshinuma, C. Suzuki, Y. Suzuki, M. Yokoyama, and the LHD Experiment Group. Characterization of edge radial electric field structures in the large helical device and their viability for determining the location of the plasma boundary. *Nuclear Fusion*, 53(1):013003, 2013.

[68] Elizaveta Kaveeva and V. Rozhansky. Screening of resonant magnetic perturbations taking into account a self-consistent electric field. *Nuclear Fusion*, 52(5):054011, 2012.

[69] M. Kobayashi, Y. Feng, F. Sardei, D. Reiter, K.H. Finken, and D. Reiser. 3d numerical transport study of the edge ergodized plasma in textor-ded. *Nuclear Fusion*, 44(6):S64, 2004.

[70] U. Kruezi, H. Stoschus, B. Schweer, G. Sergienko, and U. Samm. Supersonic helium beam diagnostic for fluctuation measurements of electron temperature and density at the tokamak textor. *Review of Scientific Instruments*, 83(6):065107, 2012.

[71] Hana Lakomá. Course on constructive geometry. Technical report, Czech Technical University, Dept. of Mathematics, Thákurova 7, 166 29 Praha 6, January 2013.

[72] P.T. Lang, A. Loarte, G. Saibene, L.R. Baylor, M. Becoulet, M. Cavinato, S. Clement-Lorenzo, E. Daly, T.E. Evans, M.E. Fenstermacher, Y. Gribov, L.D. Horton, C. Lowry, Y. Martin, O. Neubauer, N. Oyama, M.J. Schaffer, D. Stork, W. Suttrop, P. Thomas, M. Tran, H.R. Wilson, A. Kavin, and O. Schmitz. Elm control strategies and tools: status and potential for iter. *Nuclear Fusion*, 53(4):043004, 2013.

[73] Yunfeng LIANG, Hans-Rudolf KOSLOWSKI, Stefan JACHMICH, Alberto ALFIER, Christopher G. GIMBLETT, Eric NARDON, Philippa K. BROWNING, Peter DEVOY, Thomas EICH, Carine GIROUD, Geoffrey MADDISON, Peter T. LANG, Mikhail P. GRYAZNEVICH, Derek HARTING, Martin HEYN, Samuli

SAARELMA, Youwen SUN, Ronald WENNINGER, Christopher WIEGMANN, Tao ZHANG, and JET-EFDA Contributors. Overview of elm control by low n magnetic perturbations on jet. *Plasma and Fusion Research*, 5:S2018–S2018, 2010.

[74] Bruce Lipschultz. Review of marfe phenomena in tokamaks. *Journal of Nuclear Materials*, 145–147(0):15–25, 1987. Proc. of the 7th International Conference on Plasma-Surface Interactions in Controlled Fusion Devices (PSI-7), Princeton, NJ, USA, 5–9 May 1986.

[75] A. Loarte, B. Lipschultz, A.S. Kukushkin, G.F. Matthews, P.C. Stangeby, N. Asakura, G.F. Counsell, G. Federici, A. Kallenbach, K. Krieger, A. Mahdavi, V. Philipps, D. Reiter, J. Roth, J. Strachan, D. Whyte, R. Doerner, T. Eich, W. Fundamenski, A. Herrmann, M. Fenstermacher, P. Ghendrih, M. Groth, A. Kirschner, S. Konoshima, B. LaBombard, P. Lang, A.W. Leonard, P. Monier-Garbet, R. Neu, H. Pacher, B. Pégourié, R. A. Pitts, S. Takamura, J. Terry, E. Tsitrone, and the ITPA Scrape-off Layer and Divertor Physics Topical Group. Chapter 4: Power and particle control. *Nuclear Fusion*, 47(6):S203, 2007.

[76] J. Lore, W. Guttenfelder, A. Briesemeister, D. T. Anderson, F. S. B. Anderson, C. B. Deng, K. M. Likin, D. A. Spong, J. N. Talmadge, and K. Zhai. Internal electron transport barrier due to neoclassical ambipolarity in the helically symmetric experimenta). *Physics of Plasmas (1994-present)*, 17(5):056101, 2010.

[77] R. Lorenzini, A. Alfier, F. Auriemma, A. Fassina, P. Franz, P. Innocente, D. López-Bruna, E. Martines, B. Momo, G. Pereverzev, P. Piovesan, G. Spizzo, M. Spolaore, and D. Terranova. On the energy transport in internal transport barriers of rfp plasmas. *Nuclear Fusion*, 52(6):062004, 2012.

[78] R. Lorenzini, E. Martines, P. Piovesan, D. Terranova, P. Zanca, M. Zuin, A. Alfier, D. Bonfiglio, F. Bonomo, A. Canton, S. Cappello, L. Carraro, R. Cavazzana, D. F. Escande, A. Fassina, P. Franz, M. Gobbin, P. Innocente, L. Marrelli, R. Pasqualotto, M. E. Puiatti, M. Spolaore, M. Valisa, N. Vianello, P. Martin, and RFX-mod team and collaborators. Self-organized helical equilibria as a new paradigm for ohmically heated fusion plasmas. *Nature Phys.*, 5:570–574, 2009.

[79] R. Lorenzini, D. Terranova, A. Alfier, P. Innocente, E. Martines, R. Pasqualotto, and P. Zanca. Single-helical-axis states in reversed-field-pinch plasmas. *Physical Review Letters*, 101(2):025005, 2008.

[80] L Marrelli, P Zanca, M Valisa, G Marchiori, A Alfier, F Bonomo, M Gobbin, P Piovesan, D Terranova, M Agostini, C Alessi, V Antoni, L Apolloni, F Auriemma, O Barana, P Bettini, T Bolzonella, D Bonfiglio, M Brombin, A Buffa, A Canton, S Cappello, L Carraro, R Cavazzana, M Cavinato, G Chitarin, S Dal Bello, A De Lorenzi, D F Escande, A Fassina, P Franz, G Gadani, E Gaio, E Gazza, L Giudicotti, F Gnesotto, L Grando, S C Guo, P Innocente, R Lorenzini, A Luchetta, G Malesani, G Manduchi, D Marcuzzi, P Martin, S Martini, E Martines, A Masiello, F Milani, M Moresco, A Murari, L Novello, S Ortolani, R Paccagnella, R Pasqualotto, S Peruzzo, R Piovan, A Pizzimenti, N Pomaro, I Predebon, M E Puiatti, G Rostagni, F Sattin, P Scarin, G Serianni, P Sonato, E Spada, A Soppelsa, G Spizzo, M Spolaore, C Taccon, C Taliercio, V Toigo, N Vianello, P Zaccaria, B Zaniol, L Zanotto, E Zilli, G Zollino, and M Zuin. Magnetic self organization, MHD active control and confinement in RFX-mod. *Plasma Physics and Controlled Fusion*, 49(12B):B359–B369, 2007.

[81] P. Martin, L. Marrelli, G. Spizzo, et al. Overview of quasi-single helicity experiments in reversed field pinches. *Nucl. Fusion*, 43:1855–1862, 2003.

[82] E Martines, R Lorenzini, B Momo, D Terranova, P Zanca, A Alfier, F Bonomo, A Canton, A Fassina, P Franz, and P Innocente. Equilibrium reconstruction for single helical axis reversed field pinch plasmas. *Plasma Physics and Controlled Fusion*, 53(3):035015, 2011.

[83] S. Martini and the RFX team. Active mhd control at high currents in rfx-mod. *Nuclear Fusion*, 47(8):783, 2007.

[84] J. A. Mier, R. Sánchez, L. García, D. E. Newman, and B. A. Carreras. On the nature of transport in near-critical dissipative-trapped-electron-mode turbulence: Effect of a subdominant diffusive channel. *Physics of Plasmas*, 15(11):112301, 2008.

[85] O. Neubauer, G. Czymek, B. Giesen, P. W. Hüttemann, M. Sauer, W. Schalt, and J. Schruff. Design features of the tokamak TEXTOR. *Fus. Sci. Technol.*, 47(2):76–86, 2005.

[86] William A. Newcomb. Hydromagnetic stability of a diffuse linear pinch. *Annals of Physics*, 10(2):232 – 267, 1960.

[87] F. Nguyen, P. Ghendrih, and A. Grosman. Interaction of stochastic boundary layer with plasma facing components. *Nuclear Fusion*, 37(6):743, 1997.

[88] S. Ortolani and D.D. Schnack. *Magnetohydrodynamics of Plasma Relaxation*. World Scientific, Singapore, 1993.

[89] S. Ortolani and D.D. Schnack. *Magnetohydrodynamics of Plasma Relaxation*, page 118. World Scientific, Singapore, 1993.

[90] S. Ortolani and D.D. Schnack. *Magnetohydrodynamics of Plasma Relaxation*, pages 146–147. World Scientific, Singapore, 1993.

[91] S. Ortolani and D.D. Schnack. *Magnetohydrodynamics of Plasma Relaxation*, pages 96–103. World Scientific, Singapore, 1993.

[92] Sergio Ortolani and the RFX team. Active MHD control experiments in RFX-mod. *Plasma Physics and Controlled Fusion*, 48(12B):B371, 2006.

[93] R. Paccagnella, S. Ortolani, P. Zanca, A. Alfier, T. Bolzonella, L. Marrelli, M. E. Puiatti, G. Serianni, D. Terranova, M. Valisa, M. Agostini, L. Apolloni, F. Auriemma, F. Bonomo, A. Canton, L. Carraro, R. Cavazzana, M. Cavinato, P. Franz, E. Gazza, L. Grando, P. Innocente, R. Lorenzini, A. Luchetta, G. Manduchi, G. Marchiori, S. Martini, R. Pasqualotto, P. Piovesan, N. Pomaro, P. Scarin, G. Spizzo, M. Spolaore, C. Taliercio, N. Vianello, B. Zaniol, L. Zanotto, and M. Zuin. Active-feedback control of the magnetic boundary for magnetohydrodynamic stabilization of a fusion plasma. *Physical Review Letters*, 97(7):075001, 2006.

[94] H. Park, C. C. Chang, B. H. Deng, C. W. Domier, A. J. H. Donné, K. Kawahata, C. Liang, X. P. Liang, H. J. Lu, N. C. Luhmann, A. Mase, H. Matsuura, E. Mazzucato, A. Miura, K. Mizuno, T. Munsat, Y. Nagayama, M. J. van de Pol, J. Wang, Z. G. Xia, and W-K. Zhang. Recent advancements in microwave imaging plasma diagnostics. *Review of Scientific Instruments*, 74(10):4239–4262, 2003.

[95] P. Piovesan, M. Zuin, A. Alfier, D. Bonfiglio, F. Bonomo, A. Canton, S. Cappello, L. Carraro, R. Cavazzana, D.F. Escande, A. Fassina, M. Gobbin, R. Lorenzini, L. Marrelli, P. Martin, E. Martines, R. Pasqualotto, M.E. Puiatti, M. Spolaore, M. Valisa, N. Vianello, P. Zanca, and the RFX-mod Team. Magnetic order and confinement improvement in high-current regimes of rfx-mod with mhd feedback control. *Nuclear Fusion*, 49(8):085036, 2009.

[96] I. Predebon, L. Marrelli, R. B. White, and P. Martin. Particle-transport analysis in reversed field pinch helical states. *Physical Review Letters*, 93(14):145001, 2004.

[97] M. E. Puiatti, P. Scarin, G. Spizzo, M. Valisa, M. Agostini, A. Alfier, A. Canton, L. Carraro, E. Gazza, R. Lorenzini, R. Paccagnella, I. Predebon, D. Terranova, D. Bonfiglio, S. Cappello, R. Cavazzana, S. Dal Bello, P. Innocente, L. Marrelli, R. Piovan, P. Piovesan, F. Sattin, and

P. Zanca. High density physics in reversed field pinches: comparison with tokamaks and stellarators. *Nuclear Fusion*, 49(4):045012 (9pp), 2009.

[98] M. E. Puiatti, P. Scarin, G. Spizzo, M. Valisa, R. Paccagnella, I. Predebon, M. Agostini, A. Alfier, A. Canton, S. Cappello, L. Carraro, E. Gazza, P. Innocente, R. Lorenzini, L. Marrelli, and D. Terranova. High density limit in reversed field pinches. *Physics of Plasmas*, 16(1):012505, 2009.

[99] M E Puiatti, G Spizzo, M Agostini, F Auriemma, D Bonfiglio, A Canton, S Cappello, L Carraro, R Cavazzana, G Ciaccio, G De Masi, A Fassina, P Franz, M Gobbin, S C Guo, P Innocente, R Lorenzini, L Marrelli, P Martin, L Piron, R Paccagnella, I Predebon, A Scaggion, P Scarin, D Terranova, M Valisa, N Vianello, B Zaniol, M Zuin, and the RFX-mod Team. Interaction between magnetic boundary and first wall recycling in the reversed field pinch. *Plasma Physics and Controlled Fusion*, 55(12):124013, 2013.

[100] M.E. Puiatti, S. Cappello, R. Lorenzini, S. Martini, S. Ortolani, R. Paccagnella, F. Sattin, D. Terranova, T. Bolzonella, A. Buffa, A. Canton, L. Carraro, D.F. Escande, L. Garzotti, P. Innocente, L. Marrelli, E. Martines, P. Scarin, G. Spizzo, M. Valisa, P. Zanca, V. Antoni, L. Apolloni, M. Bagatin, W. Baker, O. Barana, D. Bettella, P. Bettini, R. Cavazzana, M. Cavinato, G. Chitarin, A. Cravotta, F. D'Angelo, S. Dal Bello, A. De Lorenzi, D. Desideri, P. Fiorentin, P. Franz, L. Frassinetti, E. Gaio, L. Giudicotti, F. Gnesotto, L. Grando, S.C. Guo, A. Luchetta, G. Malesani, G. Manduchi, G. Marchiori, D. Marcuzzi, P. Martin, A. Masiello, F. Milani, M. Moresco, A. Murari, P. Nielsen, R. Pasqualotto, B. Pégourie, S. Peruzzo, R. Piovan, P. Piovesan, N. Pomaro, G. Preti, G. Regnoli, G. Rostagni, G. Serianni, P. Sonato, E. Spada, M. Spolaore, C. Taliercio, G. Telesca, V. Toigo, N. Vianello, P. Zaccaria, B. Zaniol, L. Zanotto, E. Zilli, G. Zollino, and M. Zuin. Analysis and modelling of the magnetic and plasma profiles during ppcd experiments in rfx. *Nuclear Fusion*, 43(10):1057, 2003.

[101] M.E. Puiatti, G. Spizzo, F. Auriemma, L. Carraro, R. Cavazzana, G. De Masi, M. Gobbin, P. Innocente, I. Predebon, P. Scarin, M. Agostini, A. Canton, S. Dal Bello, A. Fassina, P. Franz, L. Grando, D. Mansfield, L. Marrelli, P. Martin, G. Mazzitelli, S. Munaretto, L. Roquemore, A. Ruzzon, D. Terranova, M. Valisa, A. Vertkov, B. Zaniol, and the RFX-mod Team. Wall conditioning and density control in the reversed field pinch rfx-mod. *Nuclear Fusion*, 53(7):073001, 2013.

[102] M.E. Puiatti, L. Tramontin, V. Antoni, R. Bartiromo, L. Carraro, D. Desideri, E. Martines, F. Sattin, P. Scarin, G. Serianni, M. Spolaore, M. Valisa, and B. Zaniol. Plasma rotation and structure of the radial electric field in rfx. *Journal of Nuclear Materials*, 290–293:696–700, 2001. Proc. 14th Int. Conf. on Plasma-Surface Interactions in Controlled Fusion Devices (PSI-14), Rosenheim, Germany, May 2000.

[103] M.E. Puiatti, M. Valisa, M. Agostini, F. Auriemma, F. Bonomo, L. Carraro, A. Fassina, M. Gobbin, R. Lorenzini, B. Momo, A. Scaggion, B. Zaniol, A. Alfier, L. Apolloni, M. Baruzzo, T. Bolzonella, D. Bonfiglio, A. Canton, S. Cappello, R. Cavazzana, S. Dal Bello, G. De Masi, D.F. Escande, P. Franz, E. Gazza, S. Guo, P. Innocente, G. Marchiori, L. Marrelli, P. Martin, E. Martines, S. Martini, S. Menmuir, L. Novello, R. Paccagnella, P. Piovesan, L. Piron, I. Predebon, A. Ruzzon, F. Sattin, P. Scarin, A. Soppelsa, G. Spizzo, S. Spagnolo, M. Spolaore, D. Terranova, M. Veranda, N. Vianello, P. Zanca, L. Zanotto, and M. Zuin. Internal and external electron transport barriers in the rfx-mod reversed field pinch. *Nuclear Fusion*, 51(7):073038, 2011.

[104] A. B. Rechester and M. N. Rosenbluth. Electron heat transport in a tokamak with destroyed magnetic surfaces. *Phys. Rev. Lett.*, 40:38–41, Jan 1978.

[105] D. Reiser and D. Chandra. Plasma currents induced by resonant magnetic field perturbations in tokamaks. *Physics of Plasmas (1994-present)*, 16(4):042317, 2009.

[106] M.N. Rosenbluth, R.Z. Sagdeev, J.B. Taylor, and G.M. Zaslavski. Destruction of magnetic surfaces by magnetic field irregularities. *Nuclear Fusion*, 6(4):297, 1966.

[107] V. Rozhansky, E. Kaveeva, P. Molchanov, I. Veselova, S. Voskoboynikov, D. Coster, A. Kirk, S. Lisgo, and E. Nardon. Modification of the edge transport barrier by resonant magnetic perturbations. *Nuclear Fusion*, 50(3):034005, 2010.

[108] U. Samm, M. Brix, F. Durodié, M. Lehnen, A. Pospieszczyk, J. Rapp, G. Sergienko, B. Schweer, M.Z. Tokar, and B. Unterberg. Marfe feedback experiments on textor-94. *Journal of Nuclear Materials*, 266–269(0):666–672, 1999. Proc. 13th Int. Conf. on Plasma-Surface Interactions in Controlled Fusion Devices (PSI-13), San Diego (USA) 1998.

[109] R. Sanchez, D. E. Newman, J.-N. Leboeuf, B. A. Carreras, and V. K. Decyk. On the nature of radial transport across sheared zonal flows in electrostatic ion-temperature-gradient gyrokinetic tokamak plasma turbulence. *Physics of Plasmas*, 16(5):055905, 2009.

[110] J. S. Sarff, S. A. Hokin, H. Ji, S. C. Prager, and C. R. Sovinec. Fluctuation and transport reduction in a reversed field pinch by inductive poloidal current drive. *Phys. Rev. Lett.*, 72(23):3670–3673, Jun 1994.

[111] P. Scarin, M. Agostini, L. Carraro, A. Scaggion, G. Spizzo, M. Spolaore, and N. Vianello. Boundary plasma physics in rfx-mod: Radial electric field and transport topology. *Journal of Nuclear Materials*, 438, Supplement(0):S550–S553, 2013. Proc. 20th Int. Conf. on Plasma-Surface Interactions in Controlled Fusion Devices (PSI-20), Aachen (Germany) 20–25 May 2012.

[112] P. Scarin, N. Vianello, M. Agostini, G. Spizzo, M. Spolaore, M. Zuin, S. Cappello, L. Carraro, R. Cavazzana, G. De Masi, E. Martines, M. Moresco, S. Munaretto, M. E. Puiatti, M. Valisa, and the RFX-mod Team. Topology and transport in the edge region of rfx-mod helical regimes. *Nuclear Fusion*, 51(7):073002, 2011.

[113] O. Schmitz, J.W. Coenen, H. Frerichs, M. Kantor, M. Lehnen, B. Unterberg, S. Brezinsek, M. Clever, T. Evans, K.H. Finken, M. Jakubowski, A. Kraemer-Flecken, V. Phillips, D. Reiter, U. Samm, G.W. Spakman, and G. Telesca. Particle confinement control with resonant magnetic perturbations at textor. *Journal of Nuclear Materials*, 390–391:330–334, 2009. Proc. 18th Int. Conf. on Plasma-Surface Interactions in Controlled Fusion Devices (PSI-18), Toledo, Spain, 26–30 May 2008.

[114] O. Schmitz, T. E. Evans, M. E. Fenstermacher, E. A. Unterberg, M. E. Austin, B. D. Bray, N. H. Brooks, H. Frerichs, M. Groth, M. W. Jakubowski, C. J. Lasnier, M. Lehnen, A. W. Leonard, S. Mordijck, R. A. Moyer, T. H. Osborne, D. Reiter, U. Samm, M. J. Schaffer, B. Unterberg, and W. P. West. Resonant pedestal pressure reduction induced by a thermal transport enhancement due to stochastic magnetic boundary layers in high temperature plasmas. *Phys. Rev. Lett.*, 103(16):165005, Oct 2009.

[115] O. Schmitz, M.W. Jakubowski, H. Frerichs, D. Harting, M. Lehnen, B. Unterberg, S.S. Abduallaev, S. Brezinsek, I. Classen, T. Evans, Y. Feng, K.H. Finken, M. Kantor, D. Reiter, U. Samm, B. Schweer, G. Sergienko, G.W. Spakman, M. Tokar, E. Uzgel, R.C. Wolf, and the TEXTOR Team. Identification and analysis of transport domains in the stochastic boundary of textor-ded for different mode spectra. *Nuclear Fusion*, 48(2):024009, 2008.

[116] B. Schweer, M. Brix, and M. Lehnen. Measurement of edge parameters in textor-94 at the low and high field side with atomic beams. *Journal of Nuclear Materials*, 266-269(0):673 – 678, 1999.

[117] G. Sergienko, A. Pospieszczyk, M. Lehnen, M. Brix, J. Rapp, B. Schweer, and P.T. Greenland. Spectroscopic studies of stationary marfes in textor-94. *Journal of Nuclear Materials*, 290–293(0):720–724, 2001. Proc. 14th Int. Conf. on Plasma-Surface Interactions in Controlled Fusion Devices (PSI-14), Rosenheim, Germany, May 2000.

[118] G. Serianni, W. Baker, and S. Dal Bello. High-spatial resolution edge electrostatic probe system for RFX. *Rev. Sci. Instrum.*, 74(3):1558–1562, 2003. Papers from the 14th Topical Conference on High Temperature Plasma Diagnostics.

[119] P. B. Snyder, T. H. Osborne, K. H. Burrell, R. J. Groebner, A. W. Leonard, R. Nazikian, D. M. Orlov, O. Schmitz, M. R. Wade, and H. R. Wilson. The eped pedestal model and edge localized mode-suppressed regimes: Studies of quiescent h-mode and development of a model for edge localized mode suppression via resonant magnetic perturbationsa). *Physics of Plasmas (1994-present)*, 19(5):056115–056115–9, 2012.

[120] P. B. Snyder, H. R. Wilson, J. R. Ferron, L. L. Lao, A. W. Leonard, T. H. Osborne, A. D. Turnbull, D. Mossessian, M. Murakami, and X. Q. Xu. Edge localized modes and the pedestal: A model based on coupled peeling–ballooning modes. *Physics of Plasmas (1994-present)*, 9(5):2037–2043, 2002.

[121] P. Sonato, G. Chitarin, P. Zaccaria, F. Gnesotto, S. Ortolani, A. Buffa, M. Bagatin, W. R. Baker, S. Dal Bello, P. Fiorentin, L. Grando, G. Marchiori, D. Marcuzzi, A. Masiello, S. Peruzzo, N. Pomaro, and G. Serianni. Machine modification for active {MHD} control in {RFX}. *Fusion Engineering and Design*, 66–68(0):161–168, 2003. Proc. 22nd Symposium on Fusion Technology, Helsinki (Finland), 9th-13th September 2002.

[122] K. H. Spatschek. Basic principles of stochastic transport. volume 1013, pages 250–269. AIP, 2008.

[123] G. Spizzo, M. Agostini, P. Scarin, N. Vianello, R. B. White, S. Cappello, M. E. Puiatti, M. Valisa, and the RFX-mod Team. Edge topology and flows in the reversed-field pinch. *Nuclear Fusion*, 52(5):054015, 2012.

[124] G. Spizzo, S. Cappello, A. Cravotta, D. F. Escande, I. Predebon, L. Marrelli, P. Martin, and R. B. White. Transport barrier inside the reversal surface in the chaotic regime of the reversed-field pinch. *Physical Review Letters*, 96(2):025001, 2006.

[125] G. Spizzo, R. B. White, and S. Cappello. Chaos generated pinch effect in toroidal confinement devices. *Physics of Plasmas*, 14(10):102310, 2007.

[126] G Spizzo, R B White, S Cappello, and L Marrelli. Nonlocal transport in the reversed field pinch. *Plasma Physics and Controlled Fusion*, 51(12):124026, 2009.

[127] Gianluca Spizzo, Paolo Scarin, Matteo Agostini, Alberto Alfier, Fulvio Auriemma, Daniele Bonfiglio, Susanna Cappello, Alessandro Fassina, Paolo Franz, Lidia Piron, Paolo Piovesan, Maria Ester Puiatti, Marco Valisa, and Nicola Vianello. Investigation on the relation between edge radial electric field asymmetries in rfx-mod and density limit. *Plasma Physics and Controlled Fusion*, 52(9):095011, 2010.

[128] A Stella, M Guarnieri, F Bellina, P.P Campostrini, G Chitarin, F Trevisan, and P Zaccaria. The RFX magnet system. *Fusion Engineering and Design*, 25(4):373 – 399, 1995.

[129] H. Stoschus, O. Schmitz, H. Frerichs, D. Reiser, M.W. Jakubowski, B. Unterberg, M. Lehnen, D. Reiter, U. Samm, and the TEXTOR team. Impact of rotating resonant magnetic perturbation fields on plasma edge electron density and temperature. *Nuclear Fusion*, 52(8):083002, 2012.

[130] H.R. Strauss, L. Sugiyama, G.Y. Park, C.S. Chang, S. Ku, and I. Joseph. Extended mhd simulation of resonant magnetic perturbations. *Nuclear Fusion*, 49(5):055025, 2009.

[131] W Suttrop. The physics of large and small edge localized modes. *Plasma Physics and Controlled Fusion*, 42(5A):A1, 2000.

[132] W. Suttrop, T. Eich, J. C. Fuchs, S. Günter, A. Janzer, A. Herrmann, A. Kallenbach, P. T. Lang, T. Lunt, M. Maraschek, R. M. McDermott, A. Mlynek, T. Pütterich, M. Rott, T. Vierle, E. Wolfrum, Q. Yu, I. Zammuto, and H. Zohm. First observation of edge localized modes mitigation with resonant and nonresonant magnetic perturbations in asdex upgrade. *Phys. Rev. Lett.*, 106:225004, Jun 2011.

[133] X.Z. Tang and A.H. Boozer. Finite time lyapunov exponent and advection-diffusion equation. *Physica D: Nonlinear Phenomena*, 95(3 - 4):283 – 305, 1996.

[134] D. Terranova, A. Alfier, F. Bonomo, P. Franz, P. Innocente, and R. Pasqualotto. Enhanced confinement and quasi-single-helicity regimes induced by poloidal current drive. *Phys. Rev. Lett.*, 99:095001, Aug 2007.

[135] D. Terranova, L. Marrelli, J.D. Hanson, S.P. Hirshman, M. Cianciosa, and P. Franz. Helical equilibrium reconstruction with v3fit in the rfx-mod reversed field pinch. *Nuclear Fusion*, 53(11):113014, 2013.

[136] M. Z. Tokar, J. Rapp, D. Reiser, U. Samm, F. C. Schüller, G. Sergienko, and P. C. de Vries. Localized recycling as a trigger of MARFE. *Journal of Nuclear Materials*, 266–269:958–962, 1999. Proc. 13th Int. Conf. on Plasma-Surface Interactions in Controlled Fusion Devices (PSI-13), San Diego (USA) 1998.

[137] M. Valisa, L. Frassinetti, R. Paccagnella, M. E. Puiatti, F. Sattin, P. Scarin, G. Spizzo, M. Spolaore, N. Vianello, and the RFX team. Edge transport properties of RFX-mod approaching the Greenwald density limit. In *Fusion Energy Conference (Proc. 21st Int. Conf. Chengdu, People's Republic of China, 10–21 October 2006)*, pages CD–ROM file EX/P3–17. Vienna: IAEA, 2006.

[138] H. J. van der Meiden, S. K. Varshney, C. J. Barth, T. Oyevaar, R. Jaspers, A. J. H. Donné, M. Yu. Kantor, D. V. Kouprienko, E. Uzgel, W. Biel, A. Pospieszczyk, and TEXTOR Team. 10khz repetitive high-resolution tv thomson scattering on textor: Design and performance (invited). *Review of Scientific Instruments*, 77(10):10E512, 2006.

[139] N. Vianello, E. Martines, M. Agostini, A. Alfier, A. Canton, R. Cavazzana, G. De Masi, A. Fassina, R. Lorenzini, P. Scarin, G. Serianni, S. Spagnolo, G. Spizzo, M. Spolaore, M. Zuin, and the RFX-mod Team. Transport mechanisms in the outer region of RFX-mod. *Nuclear Fusion*, 49(4):045008 (8pp), 2009.

[140] N. Vianello, G. Spizzo, M. Agostini, P. Scarin, L. Carraro, R. Cavazzana, G. De Masi, E. Martines, B. Momo, C. Rea, S. Spagnolo, M. Spolaore, M. Zuin, and the RFX-Mod Team. 3d effects on the rfx-mod boundary. *Nuclear Fusion*, 53(7):073025, 2013.

[141] R. B. White and M. S. Chance. Hamiltonian guiding center drift orbit calculation for plasmas of arbitrary cross section. *Physics of Fluids*, 27(10):2455–2467, 1984.

[142] R B White, G Spizzo, and M Gobbin. Guiding center equations of high accuracy. *Plasma Physics and Controlled Fusion*, 55(11):115002, 2013.

[143] R.B. White. Modification of particle distributions by mhd instabilities i. *Communications in Nonlinear Science and Numerical Simulation*, 17(5):2200–2214, 2012. Special Issue: Mathematical Structure of Fluids and Plasmas – Dedicated to the 60th birthday of Phil Morrison.

[144] Roscoe B. White. *The theory of toroidally confined plasmas*, page 49. Imperial College Press, 57 Shelton Street, Covent Garden, London WC2H 9HE, second edition, April 2006.

[145] Roscoe B. White. *The theory of toroidally confined plasmas*, page 242. Imperial College Press, 57 Shelton Street, Covent Garden, London WC2H 9HE, second edition, April 2006.

[146] Roscoe B. White. *The theory of toroidally confined plasmas*, page 15. Imperial College Press, 57 Shelton Street, Covent Garden, London WC2H 9HE, second edition, April 2006.

[147] Roscoe B. White. *The theory of toroidally confined plasmas*, page 66. Imperial College Press, 57 Shelton Street, Covent Garden, London WC2H 9HE, second edition, April 2006.

[148] Roscoe B. White. *The theory of toroidally confined plasmas*, page 69. Imperial College Press, 57 Shelton Street, Covent Garden, London WC2H 9HE, second edition, April 2006.

[149] Roscoe B. White. *The theory of toroidally confined plasmas*, page 35. Imperial College Press, 57 Shelton Street, Covent Garden, London WC2H 9HE, second edition, April 2006.

[150] A. Wingen, T. E. Evans, C. J. Lasnier, and K. H. Spatschek. Numerical modeling of edge-localized-mode filaments on divertor plates based on thermoelectric currents. *Phys. Rev. Lett.*, 104(17):175001, Apr 2010.

[151] A. Wingen and K.H. Spatschek. Influence of different ded base mode configurations on the radial electric field at the plasma edge of textor. *Nuclear Fusion*, 50(3):034009, 2010.

[152] Y. Xu, M. Van Schoor, R.R. Weynants, S. Jachmich, M. Vergote, M.W. Jakubowski, P. Beyer, M. Mitri, B. Schweer, D. Reiser, B. Unterberg, K.H. Finken, M. Lehnen, R. Jaspers, and the TEXTOR Team. Edge turbulence during the static dynamic ergodic divertor experiments in textor. *Nuclear Fusion*, 47(12):1696, 2007.

[153] Y. Xu, R. R. Weynants, S. Jachmich, M. Van Schoor, M. Vergote, P. Peleman, M. W. Jakubowski, M. Mitri, D. Reiser, B. Unterberg, and K. H. Finken. Influence of the static dynamic ergodic divertor on edge turbulence properties in textor. *Phys. Rev. Lett.*, 97:165003, Oct 2006.

[154] P. Zaccaria, S. Dal Bello, and D. Marcuzzi. Tests and analyses for the mechanical and thermal qualification of the new rfx first wall tiles.

Fusion Engineering and Design, 66-68:289 – 293, 2003. in Proc. 22nd Symposium on Fusion Technology.

[155] Paolo ZANCA. Beyond the intelligent-shell concept: the clean-mode-control for tearing perturbations. *Plasma and Fusion Research*, 5:017–017, 2010.

[156] Paolo Zanca, Lionello Marrelli, Gabriele Manduchi, and Giuseppe Marchiori. Beyond the intelligent shell concept: the clean-mode-control. *Nuclear Fusion*, 47(11):1425, 2007.

[157] Paolo Zanca and David Terranova. Reconstruction of the magnetic perturbation in a toroidal reversed field pinch. *Plasma Physics and Controlled Fusion*, 46(7):1115, 2004.

[158] G. M. Zaslavsky. Chaos, fractional kinetics, and anomalous transport. *Physics Reports*, 371(6):461 – 580, 2002.

[159] H Zohm. Edge localized modes (elms). *Plasma Physics and Controlled Fusion*, 38(2):105, 1996.

[160] M Zuin, N Vianello, M Spolaore, V Antoni, T Bolzonella, R Cavazzana, E Martines, G Serianni, and D Terranova. Current sheets during spontaneous reconnection in a current-carrying fusion plasma. *Plasma Physics and Controlled Fusion*, 51(3):035012, 2009.